Precision Neuromodulation of Sensorimotor Systems

by

Charles Lu

A dissertation submitted in partial fulfillment
of the requirements for the degree of
Doctor of Philosophy
(Biomedical Engineering)
in the University of Michigan
2020

Doctoral Committee:

Associate Professor Parag G. Patil, Chair
Associate Professor Cynthia A. Chestek
Assistant Professor Daniel K. Leventhal
Professor Lonnie D. Shea

Charles W. Lu

lucw@umich.edu

ORCID iD: 0000-0003-0673-7452

Acknowledgements

My experience at the University of Michigan was shaped by, more than any other influence, my time in the Patil Lab. I would like to individually thank my colleagues in the lab and clinic, each of whom played critical roles in the projects presented in this dissertation and made my time in lab as enjoyable as it was: Karlo Malaga; Matt Willsey; Layla Houshmand; Ari Lax; Brian Schwartz; Joey Costello; Kelly Lupo; Wilma Mackenzie; Matthew Cheney; Melissa Matthews, Kelvin Chou; and of course, my advisor and mentor, Parag Patil, who has enthusiastically supported me in every facet of life. Special shoutout to my student mentees, who intrepidly took on impossible projects on my behalf and taught me to lead: Walker Thompson, Kumar Duraivel, Benji Bear, Allison Tichenor, Kim Huynh, Aidan Ahamparam, and Akshay Rao. Finally, I would like to specifically thank Sunjay Dodani who gave me my start in the Patil Lab and set me on the path that I am now on.

Outside of lab, the Translational Neural Engineering community has served as an incredible source of intellectual, professional, and social support. My friends in the Chestek Lab, in particular, have played an outsized role in helping me with my projects and have graciously brought me along on their escapades. Members of my dissertation committee—Cindy Chestek, Dan Leventhal, and Lonnie Shea—have likewise provided me with invaluable advice and guidance throughout my thesis work. Across the broader university environment, I enjoyed wonderful support from the Biomedical Engineering Department, the Medical Scientist Training Program, and my colleagues in those programs. The extracurricular organizations in which I participated—

miLEAD, the University Office of Technology Transfer, the Zell-Lurie Commercialization Fund, and ESPA (Engaging Scientists in Policy and Advocacy)—and the collaborators I met there have broadened my worldview tremendously and granted me the confidence to eagerly take on all that lies ahead.

Above all, I would like to thank my friends and family for their limitless encouragement. My dad, Yiwei, taught me to how to succeed; my mom, Suwen, how to make the most of what I've been given; and my brother, Brian, how to be a good friend to the incredible people around me. I could not have asked for better support while I pursued my passions. My graduate training would also not have been what it was without the remarkable friends I have had to support me along the way. Although the number of people who have helped me over the past five years are too many to list here, I would like to specifically thank a handful of special individuals: Xiaoran, Robin, and Ryan, for keeping me connected to the real world; Emily, for keeping me in check; Paloma, for doggedly bringing me on new adventures; Henry and Yingchao, for keeping me informed of what's going on with my other degree; and Sara, for pushing me to try new experiences I otherwise would not have considered. Finally, thank you to Physics House for providing me with the most interesting and loving community I have ever been a part of, and the ILB coalition for giving me something to look forward to each week.

Table of Contents

List of Tables

List of Figures

Abstract

Therapeutic neuromodulation has an established history for clinical indications, such as deep brain stimulation for movement disorders and spinal cord stimulation for pain, despite an incomplete understanding of its mechanism of action. Novel neuroprosthetics have the potential to enable wholly new therapies, including sensory restoration and treatment of affective disorders. In order to fully realize the potential of these interventions, precise parameterization of stimulation, informed by better understanding of underlying processes, is required. This dissertation explores the temporal and spatial determinants of outcomes for stimulation within the context of clinical and experimental sensorimotor neuromodulation.

The first study of the dissertation defines a new functional target for subthalamic deep brain stimulation for Parkinson disease. We use logistic LASSO to identify features of wideband neural recordings associated with therapeutic stimulation regions derived from patient-specific anisotropic tissue activation models. The study identifies several electrophysiological markers of optimal stimulation regions, which were used in a support vector machine classifier to predict therapeutic activation regions with 64% sensitivity and 82% specificity. By predicting entire regions of therapeutic activation, this algorithm provides a tool for efficient optimization of stimulation programming.

The second study investigates the use of empirical mode decomposition, a relatively novel signal analysis tool notable for its ability to extract time-variant and non-sinusoidal signal components, for neuroprosthetic control. We directly compare the performance of empirical mode decomposition against Fourier bandpass filtering, wavelet analysis, and principal spectral component analysis within the context of electrocorticography-based finger movement decoders. Using a Naïve Bayes classifier to detect thumb movement and decode finger flexion, our results indicate that it does not outperform conventional tools despite significantly higher computational cost.

The third study presents a novel form of lead localization utilizing impedance. The study presents a scalable and computationally efficient whole-brain impedance atlas derived from individual patient diffusion tensor images. The study then shows that *in vivo* impedance measurements generally match patterns observed in electrostatic simulations of impedance in patient-specific anisotropic brain conductance models. However, we find that monopolar impedances measured using a clinical macroelectrode provide spatial information at the resolution of 2-5 millimeters, requiring additional refinement to achieve precision necessary for clinical use.

The fourth study evaluates stimulation of a novel subthalamic target for modulation of pain. Rodent studies show that stimulation of zona incerta can provide analgesic effect, and clinical evidence suggests that stimulation of a nearby nucleus, nominally used to treat Parkinson disease, often also results in improvement of pain symptoms. We directly test the analgesic effect of zona incerta stimulation in humans and show that stimulation at 20 Hz, the physiological frequency of zona incerta, selectively reduces perceived heat pain. Stimulation at 60 and 130 Hz does not modulate sensation. Likewise, stimulation of zona incerta does not modulate sensation of non-painful heat or pressure pain threshold.

The final two studies briefly examine temporal dynamics of evoked sensory activity—within a single unit and across multiple channels. The first study demonstrates, in humans undergoing thalamic deep brain stimulation surgery for essential tremor, that microstimulation of a small region in sensory thalamus with a pulse pattern modeled after its own evoked activity can reproduce the original sensation. The second study shows that natural tactile stimulation evokes highly asynchronous activity in sensory cortex of a primate model.

Chapter 1

Introduction

Background

Therapeutic neuromodulation has a well-established clinical history. For over twenty years, deep brain stimulation (DBS) has been used to treat movement disorders to great effect. Likewise, cochlear implants have restored hearing to over 300,000 individuals with hearing loss since the 1980s (National Institute on Deafness and Other Communication Disorders, 2017). More recently, neuroprosthetic interfaces have demonstrated qualified success in providing sensory feedback for artificial limbs (Tan *et al.*, 2014; George *et al.*, 2019).

Although the specific mechanisms by which electrical stimulation modulates motor systems and conscious sensation have yet to be fully elucidated, research on novel modes of neuromodulation have consistently highlighted two key determinants of outcome. First is the critical importance of location. The nervous system, in all its complexity, operates through cell bodies and axons that occupy distinct physical space. Thus, the cognitive functions affected by stimulation are largely dictated by the specific neural pathways activated by delivered charge.

Although straightforward in theory, precise spatial targeting of neuromodulation is highly complex in practice. Neural organization occurs at the level of micrometers and often in entangled neuronal populations. Accurate localization of specific neural populations and pathways can involve physical, electrophysiological, functional, genetic, and histological methods. For example, *in vivo* validation of deep brain stimulator lead placement involves physical identification of structures with imaging technologies, electrophysiological identification of the target structure using microelectrode recording, and functional testing of stimulation with clinical motor testing (Frequin *et al.*, 2020). The multitude of localization technologies used to validate lead location serve to highlight the critical importance of accurate placement. Even a two-millimeter deviation can determine the clinical success or failure of the intervention (McClelland *et al.*, 2005).

Despite the importance of precisely targeted stimulation, contemporary methods remain limited to millimeter precision (Koeglsperger *et al.*, 2019). When exacerbated with the effects of brain shift (Hunsche *et al.*, 2009), these inaccuracies can often contribute enough targeting error to require multiple electrode placement attempts to achieve satisfactory clinical effect (McClelland *et al.*, 2005; Okun *et al.*, 2005). For some, but not all indications, functional testing may be used to compensate for deficiencies in stereotactic targeting. Newer indications for DBS, such as major depression (Mayberg *et al.*, 2005), substance use disorders (Chen *et al.*, 2019), and Alzheimer dementia (Lyketsos *et al.*, 2015), do not have the benefit of functional testing and must rely solely on the limited accuracy of stereotactic targeting.

Remarkably, even for well-validated modalities of DBS, such as treatment of Parkinson disease with subthalamic stimulation, the exact mechanisms of therapeutic effect and, therefore, the precise neuromodulatory pathway of action are still unclear (Cagnan *et al.*, 2019). While previous evidence supported the hypothesis that subthalamic DBS acts through retrograde activation of motor cortex via the hyperdirect pathway (Gradinaru *et al.*, 2009; Kumaravelu *et al.*, 2018), more recent studies have highlighted limitations in this interpretation (Yu *et al.*, 2020). It is possible, instead, that therapeutic DBS acts through multiple non-exclusive mechanisms of action, including direct modulation of both upstream and downstream pathways and changes in neurochemistry (Herrington *et al.*, 2016). These potential pathways do not have established tools for directly targeting and activation using conventional DBS. These limitations in our ability to precisely deliver neuromodulation to the optimal target, both spatially and functionally, establishes opportunities for innovation.

A second key determinant of neuromodulatory outcomes is timing. In this domain, mechanistic understanding is still rapidly evolving. At a fundamental level, individual neurons often transmit information using rate and pattern encoding—the number and timing of action potentials fired over a period of time. In many cases the firing rates of individual neurons can be associated with specific behaviors or stimuli (Weiss *et al.*, 2009). Likewise, firing rates of cells across a population are also known to exhibit precise temporal dynamics (Fortier-Poisson and Smith, 2016). The importance of appropriate timing is also reflected in the diversity of stimulation frequencies employed across different indications of therapeutic neuromodulation: 130 Hz for subthalamic DBS for Parkinson disease (Koeglsperger *et al.*, 2019), 10 kHz for spinal stimulators for pain (Russo and Van Buyten, 2015), and even higher frequencies for cochlear implants (Shannon *et al.*, 2011).

Although conventional stimulation utilizes tonic patterns of electrical pulses, physiological processes employ complex, irregular spiking activity, both within firing patterns of an individual unit (Weiss *et al.*, 2009) and across neuronal populations (Fortier-Poisson and Smith, 2016). Inspired by the temporal complexity of physiological neural activity, recent works have revealed that more sophisticated patterns of stimulation may be superior to tonic stimulation in achieving pain suppression (Kirketeig *et al.*, 2019), naturalistic sensation (Tan *et al.*, 2014; Swan *et al.*, 2018; George *et al.*, 2019), and suppression of Parkinson disease symptoms (Brocker *et al.*, 2017). Mechanisms by which these patterns achieve superior effect are still unclear, limiting the generalizability of these concepts.

Together, precise location and timing determine the behavioral outcomes of stimulation. This dissertation explores the intersection of these dynamics within the context of clinical and experimental neuromodulation. The following chapters propose tools for improved localization of deep brain stimulation targets, demonstrate novel modes of stimulation for sensory modulation, and investigate specific temporal dynamics of neural activity.

Outline

Broadly, this dissertation begins with clinically oriented studies focused on questions of location: How can we know where we are in the brain? Where is it most appropriate to stimulate? These questions are informed by both physical properties of the nervous system and physiological activity of local neural populations. Subsequent chapters explore dynamics of sensory modulation, with increasing emphasis on temporal stimulation parameters and their interactions with behavioral outcome.

Chapter 2 opens with a study that unites many of the above principles in the context of subthalamic DBS for Parkinson disease. The study identifies electrophysiological markers in the frequency domain of neural signals and uses them to predict the location of therapeutic regions of stimulation. Previous studies have described electrophysiological markers of clinically optimized lead sites (Ince *et al.*, 2010; Verhagen *et al.*, 2015; Tinkhauser *et al.*, 2017). However, DBS activates volumes of brain tissue (Butson *et al.*, 2007; Maks *et al.*, 2009), rather than discrete points. This study was the first to utilize such volumes to identify neural markers of clinically therapeutic activation regions. By marrying neural recordings, tissue activation models, and machine learning, the study identifies several electrophysiological markers of optimal stimulation targets, providing a tool for efficient optimization of DBS programming.

Chapter 3 describes an investigation of empirical mode decomposition, a relatively new alternative to the Fourier techniques utilized in Chapter 2. The decomposition is notable for its ability to extract time-variant and non-sinusoidal signal components which are neglected by conventional tools (Huang *et al.*, 1998). Evidence suggests that multiunit activity does contain important signals with these characteristics (Cole and Voytek, 2017), which may be useful for neurological disease state monitoring or neuroprosthetic control. To assess the utility of this tool, we directly compare the performance of empirical mode decomposition against Fourier analysis and other state-of-the-art signal decomposition techniques within the context of electrocorticography-based finger movement decoders.

Chapter 4 presents a study that focuses explicitly on location, presenting a novel form of deep brain localization utilizing purely physical properties of brain tissue. Previous studies have reported variations in brain tissue impedance along deep brain trajectories (Robinson, 1962). These properties have been indirectly associated with parameters of non-invasive imaging data (Tuch *et al.*, 2001) and play an important role in computational models of deep brain tissue activation (Houshmand *et al.*, In review). Chapter 4 proposes using these tools to determine lead location by finding concordance between measured impedances along a rigid trajectory and estimated values derived from pre-operative imaging. Notably, this approach is intuitive, cost-effective, and overcomes common limitations of deep brain targeting. The approach is agnostic to target physiology and opens the door to precise targeting of arbitrary deep brain structures.

Chapter 5 begins the dissertation's exploration of sensory system modulation by evaluating stimulation of a novel subthalamic target for suppression of pain. Previous rodent studies have provided strong evidence that stimulation of zona incerta can provide an analgesic effect (Lucas *et al.*, 2011). There have also been clinical reports that subthalamic DBS, which typically also activates zona incerta (Plaha *et al.*, 2006), often modulates patients' sensory thresholds and pain symptoms (Custozzo *et al.*, 2020). Chapter 5 directly tests the analgesic effect of zona incerta DBS in humans, providing human translation of rodent observations and a neurophysiological explanation of the analgesic effects observed from subthalamic DBS. The study also investigates the selectivity and frequency-dependency of this intervention.

Chapter 6 presents preliminary data from an investigation of a novel approach to stimulation patterning for tactile sensory modulation. While there have been previous attempts to elicit naturalistic sensations via physiologically-inspired patterns of electrical stimulation (Swan *et al.*, 2018; George *et al.*, 2019), results have been inconsistent. This study takes the idea of biomimetic stimulation patterns to its extreme and models stimulation timing after the evoked activity of the specific unit being stimulated. Early results indicate that these tailored patterns can induce naturalistic sensations much more reliably than conventional tonic patterns, other power-matched patterns, or patterns reported elsewhere (Weiss *et al.*, 2009; Tan *et al.*, 2014; Swan *et al.*, 2018), which tend to produce parasthetic sensations. Although preliminary, the results highlight the critical importance of precise temporal parameters in neural signaling.

Chapter 7 presents the final study of this dissertation, which examines multi-unit timing dynamics of sensory-evoked activity. Literature suggests that the relative timings of action potentials from separate sensory neurons convey meaningful information about tactile input (Fortier-Poisson and Smith, 2016). This presents a plausible explanation for why electrical stimulation, which simultaneously activates large neural populations, often results in artificial parasthetic sensations. Chapter 7 presents evidence that this may indeed by the case, by demonstrating that natural tactile stimuli evoke highly unsynchronized activity in sensory cortex.

Finally, Chapter 8 places the above works within the context of existing knowledge and future possibilities. Specific attention is given to the potential clinical impact of newly developed technologies and future experiments to further explore the ideas discussed here.

Chapter 2

Electrophysiological Prediction of Therapeutic Tissue Activation Volumes

Co-authored with: Karlo A. Malaga, Kelvin L. Chou, Cynthia A. Chestek, Parag G. Patil

Abstract

Background: Subthalamic deep brain stimulation alleviates motor symptoms of Parkinson disease by activating precise volumes of neural tissue. While electrophysiological and anatomical correlates of clinically effective electrode sites have been described, therapeutic stimulation likely acts through multiple distinct neural populations, necessitating the need to characterize the full span of tissue activation. Microelectrode recordings have yet to be mapped to therapeutic tissue activation volumes and surveyed for predictive markers.

Objective: Combine high-density, broadband microelectrode recordings with detailed computational models of tissue activation to describe and to predict regions of therapeutic tissue activation.

Methods: Electrophysiological features were extracted from microelectrode recordings along 23 subthalamic deep brain stimulation implants in 16 Parkinson disease patients. These features were mapped in space against tissue activation volumes of therapeutic stimulation, modeled using clinically-determined stimulation programming parameters and fully individualized, atlas-independent anisotropic tissue properties derived from 3T diffusion tensor magnetic resonance images. Logistic LASSO was applied to a training set of 17 implants out of the 23 implants to identify predictors of therapeutic stimulation sites in the microelectrode recording. A support vector machine using these predictors was used to predict therapeutic activation. Performance was validated with a test set of six implants.

Results: Analysis revealed wide variations in the distribution of therapeutic tissue activation across the microelectrode recording-defined subthalamic nucleus. Logistic LASSO applied to the training set identified six oscillatory predictors of therapeutic tissue activation: theta, alpha, beta, high gamma, high frequency oscillations (HFO, 200-400 Hz), and high frequency band (HFB, 500-2000 Hz), in addition to interaction terms: theta x HFB, alpha x beta, beta x HFB, and high gamma x HFO. A support vector classifier using these features predicted therapeutic sites of activation with 64% sensitivity and 82% specificity in the test set, outperforming a beta-only classifier. A probabilistic predictor achieved 0.87 area under the receiver-operator curve with test data.

Conclusions: Together, these results demonstrate the importance of personalized targeting and validate a set of microelectrode recording signatures to predict therapeutic activation volumes. These features may be used to improve the efficiency of deep brain stimulation programming and highlight specific neural oscillations of physiological importance.

Keywords: Parkinson disease; deep brain stimulation; subthalamic nucleus; microelectrode recording; tissue activation volumes

Abbreviations: deep brain stimulation (DBS); subthalamic nucleus (STN); volume of tissue activation (VTA); high-frequency oscillations (HFO); high-frequency band (HFB); support vector machine (SVM)

Introduction

Deep brain stimulation of the subthalamic nucleus (STN DBS) is a well-established surgical treatment for Parkinson disease. Efficacious therapy requires both accurate surgical placement of DBS leads and careful programming of stimulation parameters. Together, these procedures ensure modulation of the correct neural pathways to achieve maximal therapeutic effect. However, conventional DBS programming to achieve optimal tissue activation is a time-consuming empirical process (Hunka *et al.*, 2005; Volkmann *et al.*, 2006).

There exist both anatomical and electrophysiological approaches to prospectively identify therapeutic activation regions. Clinical observations (Zonenshayn *et al.*, 2004; Wodarg *et al.*, 2012; Garcia-Garcia *et al.*, 2016) and computational models (Maks *et al.*, 2009; Butson *et al.*, 2011; Akram *et al.*, 2017) both point to dorsal STN as an effective stimulation target. This region is traversed by the hyperdirect pathway (Haynes and Haber, 2013), which has been strongly implicated in the therapeutic mechanisms of DBS (Gradinaru *et al.*, 2009; Kumaravelu *et al.*, 2018). Tissue activation models, in particular, have made notable contributions to this area of study. Although *in vivo* measurement of tissue activation is typically impractical, tissue activation models offer a sophisticated estimate of the anatomical region activated by therapeutic stimulation (McIntyre *et al.*, 2004; Kuncel *et al.*, 2008) and have strengthened hypotheses identifying dorsal STN and the hyperdirect pathway as optimal sites of stimulation (Maks *et al.*, 2009; Akram *et al.*, 2017). Regions of elevated beta power observed on microelectrode recording have also been associated with effective DBS (Ince *et al.*, 2010; Yoshida *et al.*, 2010; Zaidel *et al.*, 2010; Guo *et al.*, 2013; Stein and Bar-Gad, 2013; Bour *et al.*, 2015; Horn *et al.*, 2017; Tinkhauser *et al.*, 2018) and are often coincident with dorsal STN (Zaidel *et al.*, 2010; Moshel *et al.*, 2013; Verhagen *et al.*, 2015).

However, a growing body of evidence suggests that this is not the complete story. While the “average” active contact is often located near the dorsal STN border, maximally effective stimulation sites are known to vary significantly across patients (Caire *et al.*, 2013; Telkes *et al.*, 2018). This highlights a need to more precisely characterize the three-dimensional span of tissue activated by therapeutic stimulation, which has historically been analyzed as a solitary point (Ince *et al.*, 2010; Yoshida *et al.*, 2010; Guo *et al.*, 2013; Horn *et al.*, 2017). Likewise, a number of subthalamic oscillations outside the beta band—notably alpha, gamma, and high frequency oscillations—are known to play key roles in Parkinsonian neurophysiology (Foffani *et al.*, 2003; Lopez-Azcarate *et al.*, 2010; Oswal *et al.*, 2013a, b; Telkes *et al.*, 2016; Shreve *et al.*, 2017; van Wijk *et al.*, 2017; Telkes *et al.*, 2018) and potentially interact in clinically meaningful ways, such as phase-amplitude coupling (Lopez-Azcarate *et al.*, 2010; van Wijk *et al.*, 2016; Shreve *et al.*, 2017; Telkes *et al.*, 2018). These observations suggest a need to more holistically interpret the anatomical and electrophysiological loci of STN DBS intervention to better understand optimal physiological sites of action.

Here, we analyze fully individualized anisotropic models of therapeutic tissue activation alongside high-density, broadband electrophysiology. We bring together these complementary modes of study into a unified analysis of therapeutic stimulation, by mapping microelectrode recordings to clinically-derived tissue activation models. By incorporating individual heterogeneous anisotropy into our models, we achieve precise patient-specific estimates of tissue activation (Howell and McIntyre, 2016, 2017). We describe a data-driven approach to identify associations between regions of therapeutic tissue activation and broadband electrophysiological features, including cross-frequency interactions. We then show that selected signal features can be used to accurately predict spans of therapeutic activation in a test set of data.

Materials and methods

Patients

Subjects included 16 patients (11 men and 5 women) with advanced idiopathic Parkinson disease who underwent STN DBS surgery at the University of Michigan. Patient selection criteria for STN DBS at the institution have been described previously (Patil *et al.*, 2012). All patients were implanted bilaterally with Medtronic DBS leads, model 3389. Leads were placed with guidance by 3T magnetic resonance imaging (MRI), stereotactic navigation, and microelectrode recording. Subjects were STN DBS patients with stable programming parameters and subjectively satisfactory clinical outcomes 6 months after surgery. Subjects had a mean (standard deviation) age of 63 (6.1) years and mean disease duration of 10 (4.6) years. Stimulation amplitudes ranged from 1.7 to 4.8 (mean 2.8 V), with pulse width of 60 µs and frequencies of 125-185 Hz. Three implanted leads utilized two adjacent active contacts; all others utilized one active contact. Average DBS OFF and DBS ON MDS-UPDRS part III scores off medication were 45 (19) and 31 (17), with 25% improvement due to STN DBS stimulation. The study was approved by the University of Michigan Institutional Review Board, and all participants provided individual informed consent.

DBS Lead Placement

Patients underwent frame-based awake DBS surgery with microelectrode recording. Planned targets were initially assigned from indirect targeting (12 mm lateral, 3 mm posterior, and 4 mm inferior to the mid-commissural point), with adjustment from direct magnetic resonance visualization of the ventral border of STN, on 3T MRI (field of view = 200 mm x 200 mm, 0.69 x 0.69 x 1.25 mm voxels) (Philips Achieva 3T; Philips, Amsterdam, Netherlands). Recordings were performed from 15 mm above to 5 mm below the planned target on a single trajectory. Microelectrode signals were recorded at the tip of a bipolar microelectrode (MicroTargeting Electrode; FHC, Bowdin, ME), amplified (D360 Isolated Patient Amplifier System; Digitimer, Hertfordshire, England), and recorded to a computer using custom software (LabVIEW 2015; National Instruments, Austin, TX). An electrophysiologist identified the dorsal and ventral borders of the STN during surgery. DBS leads were then inserted with the tip near the ventral border of the electrophysiologically identified STN. Intraoperative confirmation of the microelectrode trajectory and DBS lead placement were performed using fluoroscopy. Additional details of the surgical procedure are described in previous publications (Patil *et al.*, 2012; Houshmand *et al.*, 2014).

Location of DBS Electrode Contacts

A high-resolution computed tomographic (CT) scan (GE HD750; General Electric, Boston, MA) was performed 2 to 4 weeks after surgery to visualize the location of DBS leads and individual electrode contacts. CT images were resampled via linear interpolation to match the resolution of the MRI images and oriented in Talairach space via coregistration to Talairach-oriented MR images using a mutual-information algorithm in commercial software (Analyze, AnalyzeDirect, Overland Park, KS). Additional detail can be found in (Houshmand *et al.*, 2014). Contacts were then directly visualized in 3D image reconstructions and coordinates were exported to MATLAB (MathWorks, Natick, MA) software for further analysis.

Tissue Activation Modeling

Preoperative diffusion tensor imaging (DTI) data for each patient were acquired using a single-shot echo planar imaging sequence with a dS-SENSE parallel-imaging scheme (reduction factor = 2, field of view = 224 mm x 224 mm, 1 x 1 x 2 mm voxels). Diffusion weighting was encoded along 16 independent orientations with a b-value of 800 s/mm^2. DTI images were resampled via cubic spline interpolation to match the resolution of the MRI images and oriented in Talairach space via coregistration to the Talairach-oriented MRI images in Analyze (Analyze

12.0; Mayo Clinic, Rochester, MN). The Analyze software DTI application was used to calculate the eigenvectors and eigenvalues of the DTI images. Diffusion tensors were then calculated from the eigenvectors and eigenvalues in MATLAB (MATLAB R2018b; MathWorks, Natick, MA) and converted to conductivity tensors using the linear relationship between conductivity and diffusion tensor eigenvalues ($\sigma/d \approx 0.844$ S·s/mm^3) as described by Tuch et al. (Tuch *et al.*, 2001).

3D finite element models of therapeutic DBS were constructed for each patient in COMSOL (Multiphysics 5.2; COMSOL, Burlington, MA), incorporating each patient's entire MRI scan, the DBS lead, and clinically-determined stimulation parameters. Brain tissue was modeled as a block with DTI-derived anisotropic conductivity tensors linearly interpolated onto the adaptive mesh. The lead was modeled as an isotropically conductive Medtronic DBS lead, model 3389, (contact: 1.4×10^{7} S/m; insulation: 1×10^{-13} S/m) (Yousif *et al.*, 2008; Kent and Grill, 2014) positioned to match the coordinates of each patient's implanted DBS contacts, as measured from post-operative CT.

Boundary conditions were defined for the DBS electrode and bulk tissue. Specifically, an electric potential was applied to the surface of the active contact(s) according to programmed stimulation parameters of each patient, floating potentials were applied to the surfaces of the remaining contacts, and ground was applied to the surface of the brain tissue. Each patient's finite element model was meshed once individually, with finer meshing applied near the lead. Simulations were then run to solve for the electric potential in each model. The models were electrostatic, assuming frequency-independent gray matter impedance (Logothetis *et al.*, 2007).

Tissue activation volumes (VTAs) were generated for each patient in COMSOL by calculating the spatial derivative of the electric potential (McNeal, 1976; Rattay, 1986) with activation thresholding at the level corresponding to each patient's clinical stimulation amplitude (Astrom *et al.*, 2015).

Microelectrode Recording

Wideband (0.1 Hz -15 kHz) spiking activity and field potentials were recorded along the DBS probe trajectory at 0.5 mm intervals, spanning from 15 mm above to 5 mm below the surgical target (the STN ventral border on imaging), using the microelectrode recording tip. A typical trajectory traverses thalamus, field of Forel, zona incerta, subthalamic nucleus, and substantia nigra. Seven seconds of uninterrupted electrophysiology was recorded at each site, with the first second of recording removed from analysis to eliminate movement artifact. Each trajectory had electrophysiology recorded at 30 to 48 sites. Microelectrode recordings less than 5 mm from the starting depth, which may have been affected by the cannula, were excluded from analysis. Recorded signal at each site was also visually examined for extraneous noise and excluded from analysis if found to be noisy. Data from 9 trajectories out of 32 implants were unavailable or excluded due to presence of significant noise. In total, microelectrode data from 641 sites were included in this analysis. Direct visualization of the microelectrode and the permanently implanted DBS lead using intraoperative fluoroscopy confirmed that both leads follow the same trajectory in the anteroposterior and dorsoventral directions. Post-operative migration of the DBS lead was assumed to be minimal. Using this relationship, electrophysiology was spatially mapped to each VTA model along the trajectory defined by the DBS lead visualized on post-operative CT.

At each depth, we calculated spike rate and the log of normalized power within the delta (0.1-4 Hz), theta (4-8 Hz), alpha (8-13 Hz), beta (13-30 Hz), low gamma (30-59 Hz), high gamma (61-200 Hz), high frequency oscillation (HFO; 200-400), and high frequency (HFB; 500-2000 Hz) bands (Thompson *et al.*, 2014). In addition to main effects, first order interaction terms, calculated as the product of each pair of covariates, e.g., log(beta power) x log(low gamma power), were also considered during analysis. Spike rate was calculated by high pass filtering the microelectrode recording at 300 Hz and counting the number of threshold crossings at 4.5 times the signal's root mean square. For analysis of oscillations, spectra of each microelectrode recording were estimated using the fast Fourier transform. To remove 60 cycle noise, spectra values within 2.5 Hz of each 60 Hz harmonic was replaced with the median power within 5 Hz of the harmonic.

Classifier Design and Validation

Predictive electrophysiological parameters for forecasting of VTA spans were identified using logistic least absolute shrinkage and selection operator (logistic LASSO). LASSO is a well-established regression method that removes uninformative covariates from linear models, thereby selecting for features that provide predictive value (Tibshirani, 1996). This was carried out using MATLAB's built-in lassoglm() function. The function requires a regularization parameter, λ, which determines the penalization of non-zero slopes. A parameter sweep of λ was used to determine the optimal value of λ to minimize divergence observed in 300-fold cross validation. The final λ value used for parameter selection was one standard deviation greater than the optimal value to prevent overfitting, following the one standard error rule for model selection (Kirkland *et al.*, 2015). Parameterization of LASSO and covariate selection were performed using a training set of the data comprised of sites along 17 lead trajectories in 13 patients (out of a total of 23 implants in 16 patients), consisting of 486 sites.

The final classifier was a support vector machine (SVM) (Cortes and Vapnik, 1995), used due to its robustness to extreme values which are often observed in electrophysiological data. The classifier incorporated the covariates identified by logistic LASSO, along with the first order terms implicated by selected interaction terms. The SVM was trained on the training data set using the

MATLAB built-in fitcsvm() function, with a one standard deviation box constraint (to prevent overfitting to outliers) and assumption of uniform prior probabilities. (Since there are many more sites sampled outside of therapeutic VTAs than inside, an SVM trained on empirical prior probabilities will be biased toward classifying points as non-VTA.) Notably, the classifier analyzed each site *independently*, predicting whether it was inside or outside of the clinically-determined VTA, using electrophysiological features recorded at that site alone (Figure 1A). The microelectrode recording from each site was analyzed independently of all other sites, without any spatial, trajectory, or subject information included in the analysis. Binary classifications from the SVM at each site were then spatially smoothed with a Gaussian window (σ=1 mm) to produce a probabilistic prediction spanning the DBS lead trajectory (Figure 1B). Performance of the smoothed prediction was characterized by a receiver-operator characteristic curve.

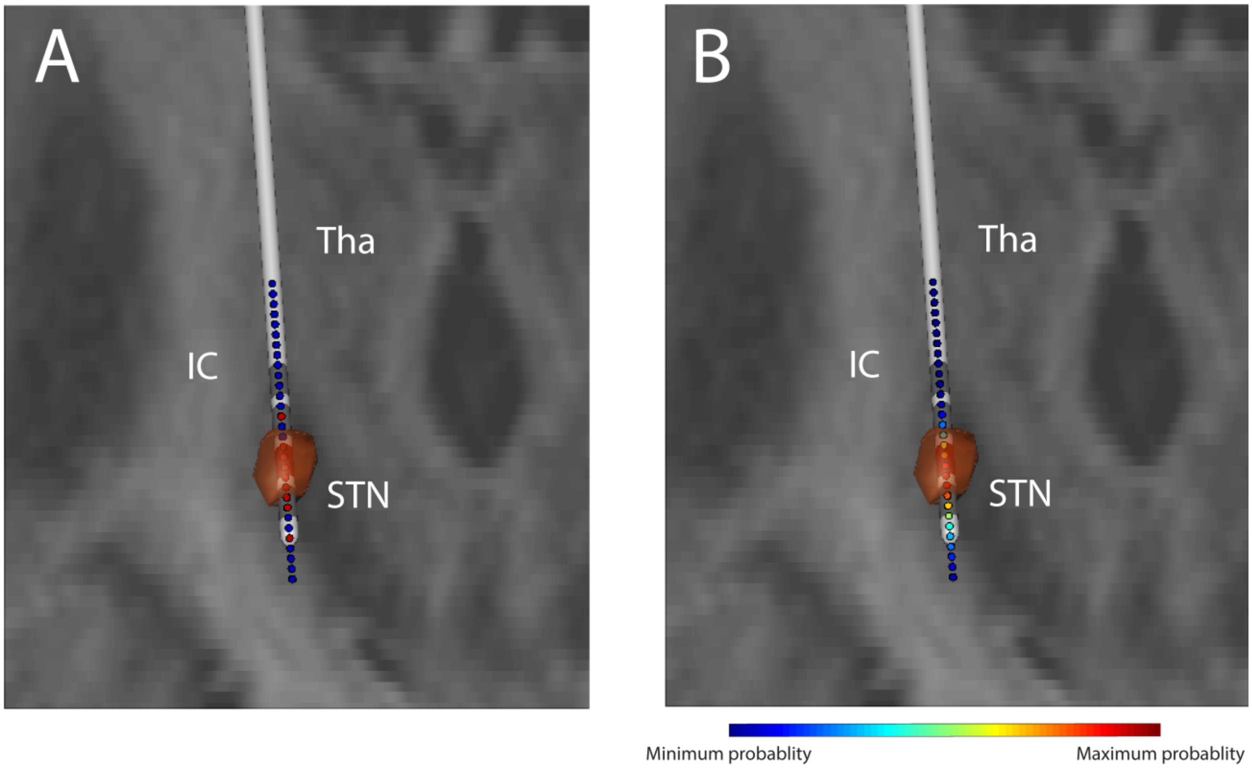

Figure 2-1 Patient example of algorithm predictions projected upon the corresponding COMSOL model of clinically effective tissue activation and patient MRI. (A) SVM binary predictions of clinically activated sites. Sites predicted to be within the therapeutic VTA (shown in orange) are indicated with red circles; sites predicted to be outside

indicated with blue. Active contact is shown in red. (B) The predictions shown in A are smoothed over space to produce a probabilistic prediction, accounting for the spatially contiguous nature of VTAs. Colors indicate probability of a site being within the therapeutic VTA, with hotter colors indicating higher probability.

Performance of the SVM classifiers were determined using a holdout set of data comprised of electrophysiology from 155 sites (from six lead trajectories in three randomly selected patients not included in the training set). As such, classifier design and validation were achieved using wholly separate sets of data. This was done to ensure that classifier performance is not a result of overfitting to the training data.

The optimized SVM classifier was compared to both a beta-only classifier and a simple STN border-based approach to targeting and programing. The STN border approach assumes 2.8 V (cohort average) monopolar stimulation at the electrophysiologically-defined dorsal border of STN. This passive approach to programming activates 2.0 mm of tissue in each direction along the span of the DBS lead (observed in two implants with 2.8 V monopolar stimulation).

Statistical Analysis

All statistical tests were performed using MATLAB software. Statistical validation of classifier performance was determined using Fisher's exact test. Classifiers were compared using the McNemar test. Performance metrics are assessed using test data.

Results

Lead Placement and Tissue Activation Locations

DBS lead placement was found to vary across patients, with the average active contact located 1.9 mm ventral to the electrophysiological STN dorsal border. Tissue activation volumes modeled from clinically-determined stimulation parameters of different implants spanned regions above, within, and/or below the STN. 18% of observed VTA spans along the DBS lead were dorsal to STN, 37% within the dorsal half of STN, 36% within the ventral half of STN, and 9% ventral to STN.

Predictive Electrophysiological Features

A parameter sweep was used to determine the most appropriate regularization constant for logistic LASSO regression of VTA spans against microelectrode recordings. The sweep, performed using 300-fold cross-validation on the training set of 486 sites, yielded an optimal regularization constant of $\lambda=0.00633$, with a standard deviation of 0.0308. Details of the parameter sweep are shown in Supplementary Figure 1. Re-running LASSO with a regularization constant equal to the optimal value plus the standard deviation ($\lambda=0.0591$) identified five predictive neural features: HFB, theta x HFB, alpha x beta, beta x HFB, and high gamma x HFO. The main effects implicated by the interaction terms—theta, alpha, beta, high gamma, and HFO—were included as predictors for subsequent classifier analysis.

Support Vector Machine Predictions

Table 2-1 Classifier performance. Classifier performance using the full model determined by LASSO and using a beta-only model. PPV = positive predictive value; NPV = negative predictive value; LOOCV = leave-one-out cross-validation

	Full model			Beta only		STN-border
	Train	Test	LOOCV	Train	Test	Test
Accuracy	0.76	0.77	0.73	0.51	0.52	0.70
Sensitivity	0.60	0.64	0.56	0.53	0.57	0.50
Specificity	0.85	0.82	0.83	0.50	0.50	0.77
PPV	0.67	0.57	0.63	0.35	0.30	0.45
NPV	0.81	0.86	0.91	0.67	0.76	0.81

A support vector machine classifier was used to predict therapeutic tissue activation sites using ten electrophysiological features: theta, alpha, beta, high gamma, HFO, HFB, theta x HFB, alpha x beta, beta x HFB, and high gamma x HFO. The binary classifier achieved 77% accuracy, with 64% sensitivity and 82% specificity on the test set of 155 independently analyzed sites (Table 1). Performance was significantly above chance with an odds ratio of 8.4 (Fisher's exact test: $p<10^{-6}$; 95% confidence interval: 3.8-18.5). Leave-one-out cross-validation (COOCV) (partitioned by implant) of the support vector machine achieved similar overall performance. Binary predictions and VTA models for each trajectory analyzed in this study can be seen in Supplementary Figure 2. This model outperformed both a beta-only classifier (McNemar's test: $p<10^{-6}$) and the STN border-based approach to targeting and programming (McNemar's test: p=0.1175) (Table 1). Performance of the model was also evaluated against classifiers using individual frequency bands and a classifier using all available covariates (Supplementary Table 1). The model using LASSO-selected covariates achieved greater predictive value than all other classifiers. The HFB and spike rate-only classifiers were the highest-performing alternative models, both with accuracies of 74%.

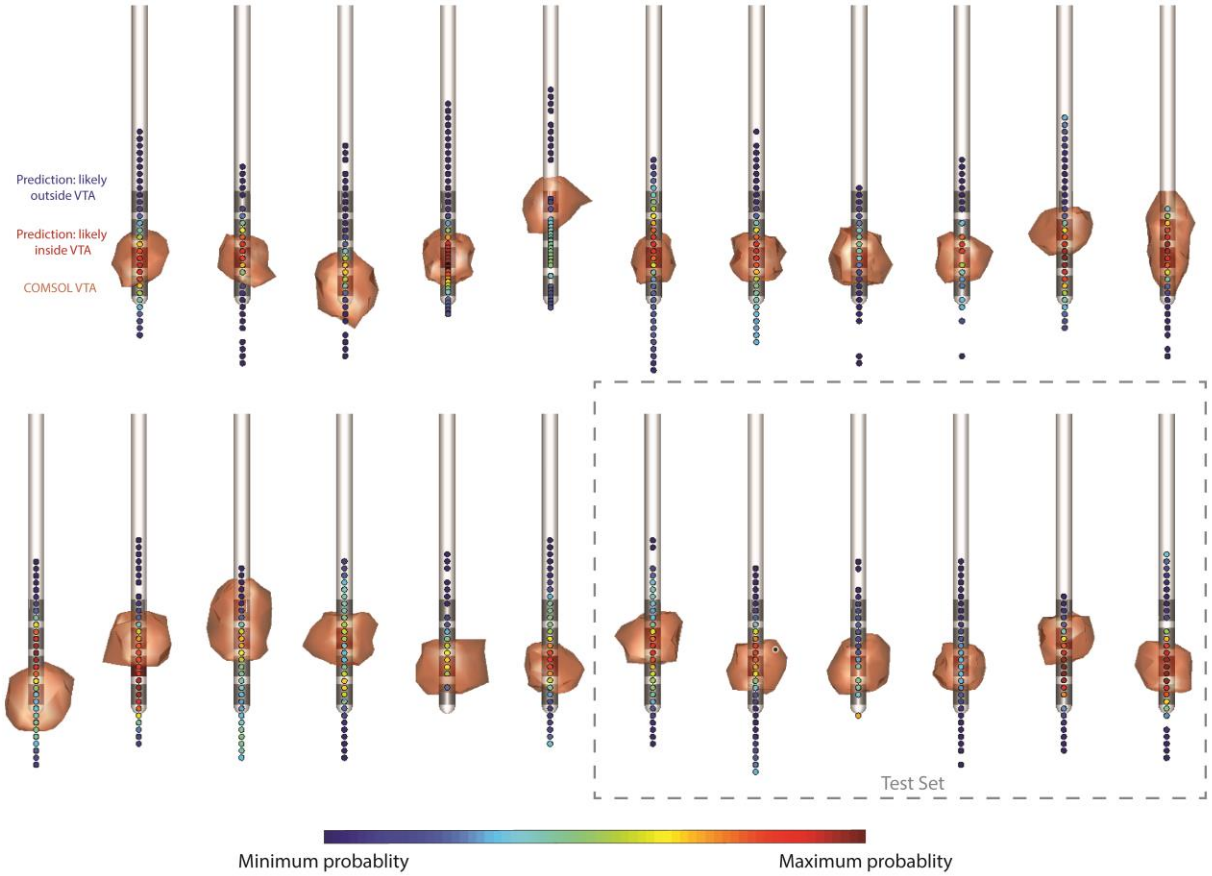

Figure 2-2 Therapeutic VTA locations along DBS lead trajectories and smoothed classifier predictions, for all implants. Colors indicate probability of a site being within the therapeutic VTA, with hotter colors indicating higher probability. Active contact is shown in red. Two leads utilized two active contacts (both anodic and synchronized). Test data comprised of six implants is enclosed by the gray dotted line. The implant shown in Figure I is shown as the top left implant in this figure.

While therapeutic activation sites may exist as isolated regions throughout the STN region, VTAs generated by conventional leads must be contiguous in space. To yield a more clinically useful prediction of VTA span reflecting this possibility, binary classifications of individually analyzed points were smoothed with a Gaussian window (σ=1 mm) to be graded over space (Figure 2). The smoothed predictions yielded probabilistic scores with an AUC of 0.87 for the test data (Figure 3). Examination of individual implants in Figure 2 reveals that classifier performance can vary by implant, with some predictions fully concordant with modeled VTAs, while others exhibit only slight overlap.

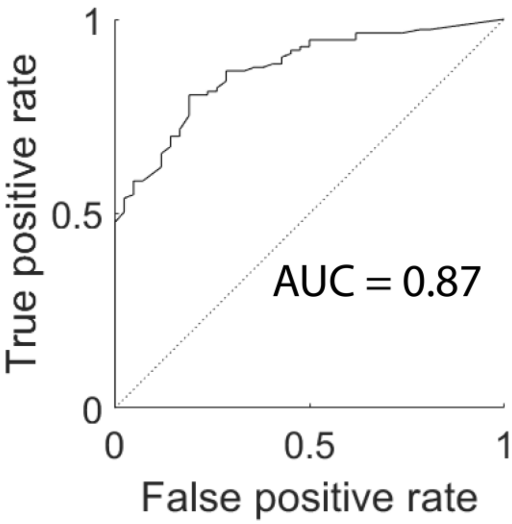

Figure 2-3 Receiver operating characteristic curve of smoothed classifier. Calculated from test data. AUC = area under curve.

Interpretation of Covariate Effects

In the SVM classifier, higher values of beta, HFB (500-2000 Hz), and theta x HFB were positive predictors of therapeutic VTAs, while higher values of theta, alpha, high gamma, HFO, alpha x beta, beta x HFB, and high gamma x HFO were negative predictors. In general, single covariates were insufficient to accurately forecast effective sites of tissue activation along the DBS trajectory.

Of particular interest was the predictive effect of beta. Plotting beta power against HFB (Figure 4A) shows that elevated beta is a positive predictor of therapeutic activation sites, but only in the presence of high HFB. Sites with high beta are not activated by therapeutic stimulation when observed with low HFB. HFB-theta interactions show a different effect: low theta power is a positive predictor of therapeutic activation when coincident with high HFB power (Figure 4B). As HFB is an indicator of STN multiunit activity (Novak *et al.*, 2011), these interactions suggest that high beta and low theta power are positive predictors of therapeutic activation only within the STN. Overlapping regions of VTA and non-VTA sites show that these covariates must still be interpreted alongside other bands of interest to generate reliable predictions. Alpha-beta and high gamma-HFO interactions were also identified as predictors of therapeutic activation. While the nature of interactions between these oscillations and their relation to VTAs is unclear from visual analysis, the high covariance observed between these pairs of covariates is notable (Figure 4C-D).

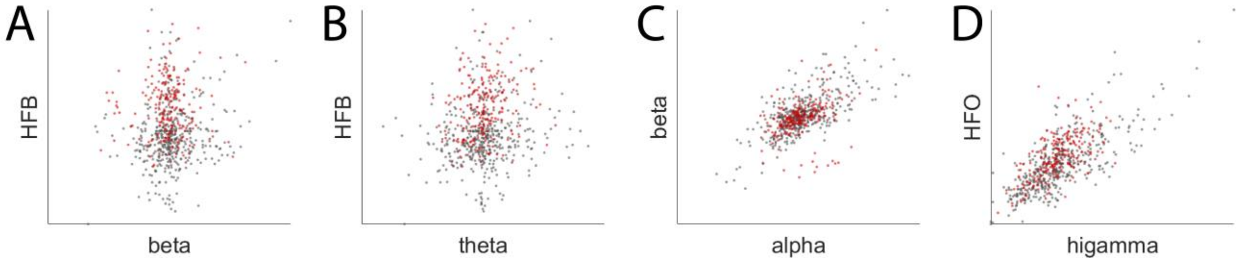

Figure 2-4 Power within main effects of interaction terms plotted against one another show inter-frequency dependence of predictors. Red points indicate sites within modeled VTAs, gray points indicate sites outside. Axes are scaled along arbitrary units. A shows interactions between main effects of the beta x HFB term, B for theta x HFB, C for alpha x beta, and D for high gamma x HFO.

Discussion

This study yields three notable findings. First, we used atlas-independent, fully individualized patient VTA models to show that clinically effective tissue activation volumes can span a variety of locations, with large proportions of clinically optimized tissue activation observed both above and within the electrophysiologically-defined STN. Second, we mapped high-density, broadband microelectrode recordings to individualized VTAs, and applied a data-driven method to objectively select and validate seven anatomically agnostic electrophysiological predictors of therapeutic tissue activation in the subthalamic region. Third, we demonstrated and validated a predictive clinical tool to aid DBS lead placement and programming that significantly outperforms a beta-only classifier. When tested on a set of three randomly selected new patients, the algorithm achieved an AUC of 0.87, demonstrating high accuracy and generalizability across patients. In doing so, this study unifies anatomical, electrophysiological, and computational analyses to describe and to validate electrophysiological signatures of regions activated by therapeutic STN DBS.

Logistic LASSO suggested ten electrophysiological predictors of therapeutic VTAs that were subsequently validated by an SVM classifier: theta, alpha, beta, high gamma, HFO, HFB, theta x HFB, alpha x beta, beta x HFB, and high gamma x HFO. While covariates of the relatively simple model used here do not directly reflect physiological mechanisms of treatment or disease pathology, the high predictive value of the SVM does warrant additional attention toward the selected oscillations. Predictive frequency bands identified in this study both support the literature on existing oscillations of interest and suggest new directions of investigation. Power in beta, HFO, alpha, and gamma bands are well-established correlates of Parkinsonian symptoms: beta and HFO are associated primarily with bradykinesia and rigidity, while gamma and alpha oscillations are more often associated with other motor manifestations and affective components of Parkinson disease (Foffani *et al.*, 2003; Ozkurt *et al.*, 2011; Oswal *et al.*, 2013b). Likewise, subthalamic theta activity has been causally linked to Parkinsonian tremor (Tass *et al.*, 2010). Together, these separate frequency bands may independently contribute information about different dimensions of Parkinsonism, each of which can be acted upon by therapeutic DBS. In contrast, HFB power represents STN multiunit activity and therefore provides primarily anatomical information (Novak *et al.*, 2011). Evaluation of an HFB-only classifier reveals high predictive value in this anatomical information, as expected from the well-established practice of targeting STN. Other frequency bands likely contribute information to more precisely identify therapeutic activation sites within and adjacent to STN. Notably, spike rate was not selected as a predictive feature of therapeutic VTAs, despite the unique spiking activity of STN. Its exclusion from the LASSO model is likely due to spiking rate's high covariance with HFO and HFB (Schlag and Balvin, 1963; Stark and Abeles, 2007), which reduces the amount of predictive information it contributes to the model. Elevated spike rate is also often observed in thalamus, which is rarely activated by STN DBS, further reducing its contribution to the predictive model. Note, however, that the microelectrode features used in this study are extracted from only six seconds of recording at each site, which may neglect phenomena that occur at longer time scales and limit the quality of spectral estimation used for other features.

Interaction terms selected by LASSO must be carefully interpreted. The HFB interaction terms identified here provide anatomical context for interpretation of beta and theta power, by restricting their predictive value to sites within STN. Interpretation of the alpha-beta interaction is less obvious. Stein and Bar-Gad (Stein and Bar-Gad, 2013) suggest that perhaps a single physiologically important oscillation is captured by both alpha and beta bands, in concordance with the high covariance of alpha and beta observed in our data, which the model corrects for using the interaction term. There also exists some evidence that the two bands together are directly linked to presentation of parkinsonian tremor (Hirschmann *et al.*, 2019). Similar phenomena may also explain inclusion of the high gamma-HFO interaction in the LASSO model. Perhaps surprisingly, beta-gamma and beta-HFO interactions were excluded. This is likely due to the complex nature of described interactions between beta and high frequency oscillations (Lopez-Azcarate *et al.*, 2010; van Wijk *et al.*, 2016), which would not be captured by the simplistic metric used here.

Looking ahead, the prominence of multi-frequency interactions identified and validated here strongly points to avenues of future study. Telkes et al. (Telkes *et al.*, 2016) recently demonstrated that information in beta must be fused with high frequency bands to accurately predict optimal implantation tracks. While the interactions analyzed in this study and by Telkes indicate only that power across frequency bands should be jointly assessed in the predictive model, there also exist more complex measures of interaction that may provide valuable additional information. Sophisticated multi-frequency phenomena, such as phase-amplitude coupling (van

Wijk *et al.*, 2016; Shreve *et al.*, 2017) and beta burst length (Tinkhauser *et al.*, 2017), have demonstrated physiological relevance. While the regression-based approach described here is unsuitable for analysis of these predictors, the cross-frequency features identified here and in other studies highlight the importance of investigating different components of broadband electrophysiology in concert.

Anatomically, we used atlas-independent, fully individualized VTA models to show that therapeutic effect can be achieved with tissue activation across a variety of sites both within and outside the STN borders. Most therapeutic VTAs activated regions within and above STN, which can be largely achieved with 2.8 V stimulation at dorsal STN. This is in line with prior work pointing to dorsolateral STN as an optimal site of stimulation (Zonenshayn *et al.*, 2004; Wodarg *et al.*, 2012). STN border-based programming was outperformed by microelectrode predictions, although the difference was not statistically significant. However, nuances in performance of the STN border approach necessitate important caveats to this finding. The low positive predictive value (0.45) of STN border-based programming suggests that it activates a large portion of tissue that need not be stimulated for therapeutic effect. Furthermore, the specificity of the approach is likely overestimated. Although key sites of therapeutic activation may be distinct, conventional VTAs must be spatially contiguous, activating neighboring regions. Thus, STN border-based programming and the therapeutic VTAs used for reference exhibit the same systematic error, artifactually inflating the measured specificity. When interpreted together with the anatomical diversity of therapeutic activation regions observed across subjects, as reported by earlier studies (Caire *et al.*, 2013; Hamel *et al.*, 2017), these findings support opportunities for additional refinement of DBS targeting and personalized stimulation.

Although this study treats therapeutic tissue activation as a binary variable, presentations of Parkinson disease and its response to STN DBS are known to be multidimensional and varied across patients. A robust body of work suggests that different symptoms may be optimally treated by activation of different subthalamic regions and neural pathways with unique electrophysiological markers (Moran *et al.*, 2008; Oswal *et al.*, 2013b; Bour *et al.*, 2015; Kuhn and Volkmann, 2017). In this view, it is critical to consider the full span of activated tissue when identifying neural markers of DBS targets, as therapy is likely achieved through activation of multiple sites with distinct electrophysiological signatures. Recent work by Telkes et al. (Telkes *et al.*, 2018) showed that different motor subtypes of Parkinson disease present with unique multiband signatures in spatially distinct STN regions. Close examination of results in Figure 2 reveal large variations in classifier performance between individual implants, suggesting that this phenomenon is likely present in the current study as well. These observations demonstrate the significant potential for further progress in this area. Future work will directly examine these relationships and their utility in treatment optimization.

It is important to note that the analysis here must be understood within the context of some fundamental limitations of the methodology. The spatially contiguous nature of VTAs guarantees that the clinically determined sites of therapeutic activation are biased to include non-therapeutic regions adjacent to clinically important sites of activation. This intrinsic error in our designation of therapeutic activation regions likely introduces significant noise into the algorithm, both in design and validation. Also, the spatial relationship between recorded oscillations and the corresponding synchronous neural population is both imprecise and incompletely understood (Lempka and McIntyre, 2013; Maling *et al.*, 2018), limiting the precision of microelectrode predictions. Spatially smoothing the predictions in this study provided an informative but imperfect remedy for these sources of imprecision.

More generally, it should be noted that tissue activation modeling is complex and makes several specific assumptions. This study utilizes fully individualized anisotropic conductivities and simple activation thresholds to calculate precise patient-specific VTAs. Alternative approaches, such as those employing explicit axon models (Gunalan *et al.*, 2017) and driving force calculations (Peterson *et al.*, 2011), may yield different therapeutic activation volumes (Gunalan *et al.*, 2018). At the same time, literature suggests that incorporation of tissue heterogeneity and anisotropy generates reliable activation models (Howell and McIntyre, 2016, 2017). Small errors in image co-registration and lead movement after implantation may also introduce errors into our analysis.

Nonetheless, by predicting both the approximate location and span of generalized therapeutic tissue activation volumes, the approach presented here can be used to quickly estimate effective sites and amplitudes of stimulation. Perhaps more importantly, this method significantly restricts the parameter space that must be explored to optimize DBS stimulation parameters. With the introduction of directional DBS leads promising greater therapeutic windows (Contarino *et al.*, 2014; Pollo *et al.*, 2014; Dembek *et al.*, 2017), new tools such as the one presented here are needed to constrain the greatly expanded parameter space of directional leads to efficiently interrogate potential program settings. Eventually, such targeting methods may be used in concert with parameter optimization algorithms (McIntyre *et al.*, 2006; Teplitzky *et al.*, 2016; Xiao *et al.*, 2016; Pena *et al.*, 2017; Anderson *et al.*, 2018), potentially achieving even greater STN DBS programming efficiency.

Acknowledgements

We are grateful for the assistance of Kelly Lupo in image processing and care of patients included in this study.

Funding

This research was supported by the A. Alfred Taubman Medical Institute, the Coulter Foundation, the STIM (Surgical Therapies Improving Movement) Program, and a Ford Foundation Predoctoral Fellowship.

Supplement

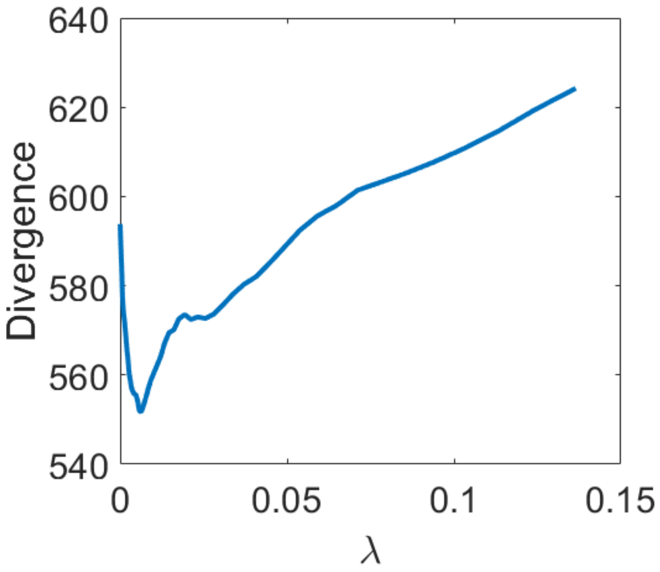

Figure 2-5 (Supplementary Figure 1) LASSO regularization parameter sweep. Parameter sweep of λ using 300-fold cross-validation over the training data set. Minimum divergence was found at $\lambda = 0.00633$, with a standard deviation of 0.0308.

Figure 2-6 (Supplementary Figure 2) Therapeutic VTA locations along DBS lead trajectories and binary classifier predictions, for all implants. Sites predicted to be within the therapeutic VTA (shown in orange) are indicated with red circles; sites outside indicated with blue. Active contact is shown in red. Two leads utilized two active contacts (both anodic and synchronized). Test data comprised of six implants is enclosed by the gray dotted line. The implant shown in Figure I is shown as the top left implant in this figure.

Table 2-2 (Supplementary Table 1) Classifier performance by covariate set. Performance of classifiers using LASSO-selected covariates, all covariates, and individual frequency bands. Reported values are from validation on the test data. PPV = positive predictive value; NPV = negative predictive value.

Included covariates	Accuracy	Sensitivity	Specificity	PPV	NPV
LASSO-selected	0.77	0.64	0.82	0.57	0.86
All	0.70	0.62	0.64	0.46	0.84
Delta	0.41	0.50	0.37	0.23	0.67
Theta	0.48	0.64	0.42	0.29	0.76
Alpha	0.39	0.98	0.17	0.30	0.95
Beta	0.52	0.57	0.50	0.30	0.76
Low gamma	0.43	0.62	0.35	0.26	0.71
High gamma	0.49	0.3	0.53	0.23	0.70
High frequency oscillations	0.58	0.60	0.58	0.34	0.79
High frequency band	0.74	0.64	0.78	0.52	0.78
Spike rate	0.74	0.43	0.86	0.53	0.80

Chapter 3

Evaluation of Empirical Mode Decomposition in Finger Decoding

Co-authored with: Suseendrakumar Duraivel, Akshay T. Rao, J. Nicole Bentley, William C. Stacey, Cynthia A. Chestek, and Parag G. Patil

Abstract

Objective. Conventional neural signal analysis methods assume that features of interest are linear, time-invariant signals confined to well-delineated spectral bands. However, new evidence suggests that neural signals exhibit important non-stationary characteristics with ill-defined spectral distributions. These features pose a need for signal processing algorithms that can characterize temporal and spectral features of non-linear time series. This study compares the effectiveness of four signal processing algorithms in extracting neural information and decoding cortical signals: Fourier bandpass filtering (FFT), principal spectral component analysis (PSCA), wavelet analysis (WA), and empirical mode decomposition (EMD).

Approach. Electrocorticographic signals were recorded from the motor and sensory cortex of two epileptic patients performing finger movements. Each signal processing algorithm was used to extract beta (10-30 Hz) and gamma (66-114 Hz) band power to detect finger movement and decode finger flexions, respectively. Naïve Bayes classifiers using each signal were validated using leave-one-out cross-validation.

Main results. All four algorithms achieved above 90% accuracy in finger movement detection using beta power. When decoding individual finger flexion using gamma, the PSCA classifier achieved 83 ± 4% accuracy while FFT, WA, and EMD analysis achieved accuracies of 75 ± 6%, 68 ± 5%, and 56 ± 5% respectively.

Significance. These results reveal some of the advantages and limitations of each approach to signal decomposition, which can inform the development of effective neural decoding pipelines. Further analysis could compare performance in extracting more specific non-sinusoidal features, such as transients and phase-amplitude coupling.

Author’s Note

The project described in this chapter was originally conceived by Suseendrakumar Duraivel, who also wrote all code and performed all analysis related to this project. The dissertation author (Charles Lu)’s contribution to the chapter consisted of high-level direction and coordination of the project, code review, interpretation of results, manuscript design, and manuscript revisions.

Introduction

Conventional Fourier bandpass filtering (FFT) uses deterministic frequency bands to extract signal information and assumes that neural signals can be represented as time-invariant sinusoids. However, recent studies suggest that neural oscillations possess broadband, power-law characteristics dispersed across the frequency domain and exhibit physiologically important non-stationary features (Miller *et al.*, 2009c; Cole and Voytek, 2017), including non-sinusoidal waveforms in cortical beta (Manning *et al.*, 2009; Cole *et al.*, 2017).

Signal-processing tools that can capture both the spectral and temporal dynamics of neural signals may improve analysis of neural waveforms. For example, principal spectral component analysis (PSCA) uses singular value decomposition to capture spectral components that exhibit maximum variance during epochs of interest (Jolliffe and Cadima, 2016).

On the other hand, wavelet analysis (WA) and empirical mode decomposition (EMD) capture temporal variations in neural signals evoked by physiological activity. WA uses short-time wavelike oscillations to extract the temporal response (Mallat, 1989), whereas EMD iteratively decomposes temporal patterns in the neural signal (Huang *et al.*, 1998). These three algorithms have the potential to capture spectral variations and non-stationary features of neural signals.

This study directly compares the performance of these four signal decomposition techniques within the context of finger decoding. We applied FFT, PSCA, WA, and EMD to decode human ECoG signals during movement. Beta and gamma powers extracted from each algorithm were used to train separate Naïve-Bayes classifiers to detect thumb movement and decode finger flexion, respectively. The performance of each classifier was then compared to gain insights on the quality of signal extraction. Our results indicate some of the advantages and limitations of each approach, offering new perspectives on the development of neural decoding pipelines and warranting future studies that compare extraction of specific non-sinusoidal features, such as transient activity and phase-amplitude coupling.

Methods

All human procedures were carried out in accordance with protocols approved by the Institutional Review Board at the University of Michigan.

Human ECoG signals

Electrocorticographic signals were recorded from two epileptic patients at 30 kHz using a Neuroport signal processor (Blackrock Microsystems). The subjects had been implanted with clinical subdural ECoG grids (Figure 1) for epilepsy treatment as previously described in (Irwin *et al.*, 2016). Subjects were cued to flex fingers independently during eight-second movement trials. Finger positions were recorded using a DataGlove 5 Ultra (5DT) with flex sensors on each finger. Each finger was flexed eight to twelve times. For this analysis, we considered only the thumb, index, and little fingers. The data were subsampled to 10 kHz and common average referenced across each ECoG grid. Movement was defined as the 1-second period following movement onset, as measured by the DataGlove. Rest was defined as a period >1-second during which no movement was recorded. Three data sets were analyzed: one set of 27 trials from Patient 1 (P1a), a second set of 33 trials from Patient 1 performed on a separate day (P1b), and 29 trials from Patient 2 (P2).

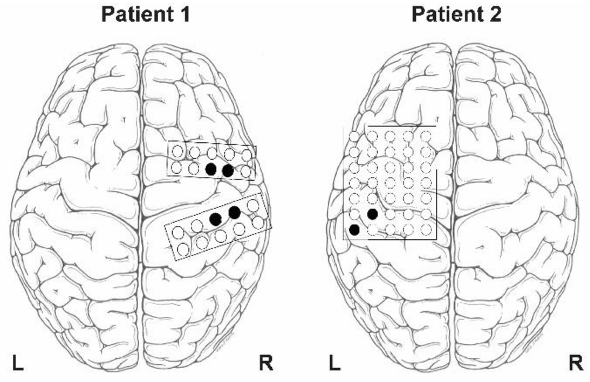

Figure 3-1 Electrode positions for the two subjects. Signals recorded from the black electrodes were used for analysis.

Fourier bandpass filtering (FFT)

Spectral analysis through Fourier filtering (FFT) assumes that fluctuations in activity can be characterized by sinusoids. Processing nonsinusoidal data with FFT may reveal non-existent harmonics, making it difficult to characterize cross-frequency coupling in neural signals (Kramer *et al.*, 2008). Regardless, the simplicity of FTT makes it an ideal choice to many neural signal decoding tasks.

Fourier bandpass filtering of beta and gamma was implemented using 8th order elliptic IIR bandpass filters. Beta band cutoffs were 10 Hz and 30 Hz; cutoffs for gamma were 66 Hz and 114 Hz (Schroeder *et al.*, 2017).

Principal spectral component analysis (PSCA)

Principal component analysis is an adaptive processing algorithm that reduces the dimensionality of a dataset into predefined variables, known as principal components. PSCA is the application of this algorthm to a signal's power spectral density (Jolliffe and Cadima, 2016).

Since this is a data-driven method, it can prove useful for decomposing the spectral data of complex neural signals. Previous work has used PSCA to accurately detect finger movement from cortical signals (Miller *et al.*, 2009a).

Power spectra with 1024 frequency points up to Nyquist frequency were computed using MATLAB's periodogram function and normalized across trials. Principal component analysis was then applied to the normalized power spectra to obtain principal components and component scores. The beta and gamma powers were represented using the second and first principal components, respectively.

Wavelet analysis (WA)

Wavelet transforms provide temporally localized frequency analysis that can overcome the frequency-time resolution trade-offs exhibited by the short-time Fourier transform (Cohen, 2014). We used the analytical Morlet wavelet to construct a scalogram between 5 Hz and 200 Hz with 1.95 Hz resolution. We extracted beta and gamma power by summing the squares of absolute coefficients in each frequency band.

Empirical mode decomposition (EMD)

EMD is a data processing tool introduced to process non-linear and non-stationary time series. The algorithm, developed by Huang et al., reduces a composite signal into a set of oscillatory time-series called intrinsic mode functions (IMFs) by iteratively subtracting the mean of the signal's temporal envelope (Huang *et al.*, 1998). Previous work has demonstrated the utility of EMD in processing neural signals for a variety of prediction tasks, including estimation of anesthetic depth, classification of epileptic seizures, and classification of finger flexion (Hazrati, 2012; Huang *et al.*, 2013; Cho *et al.*, 2017).

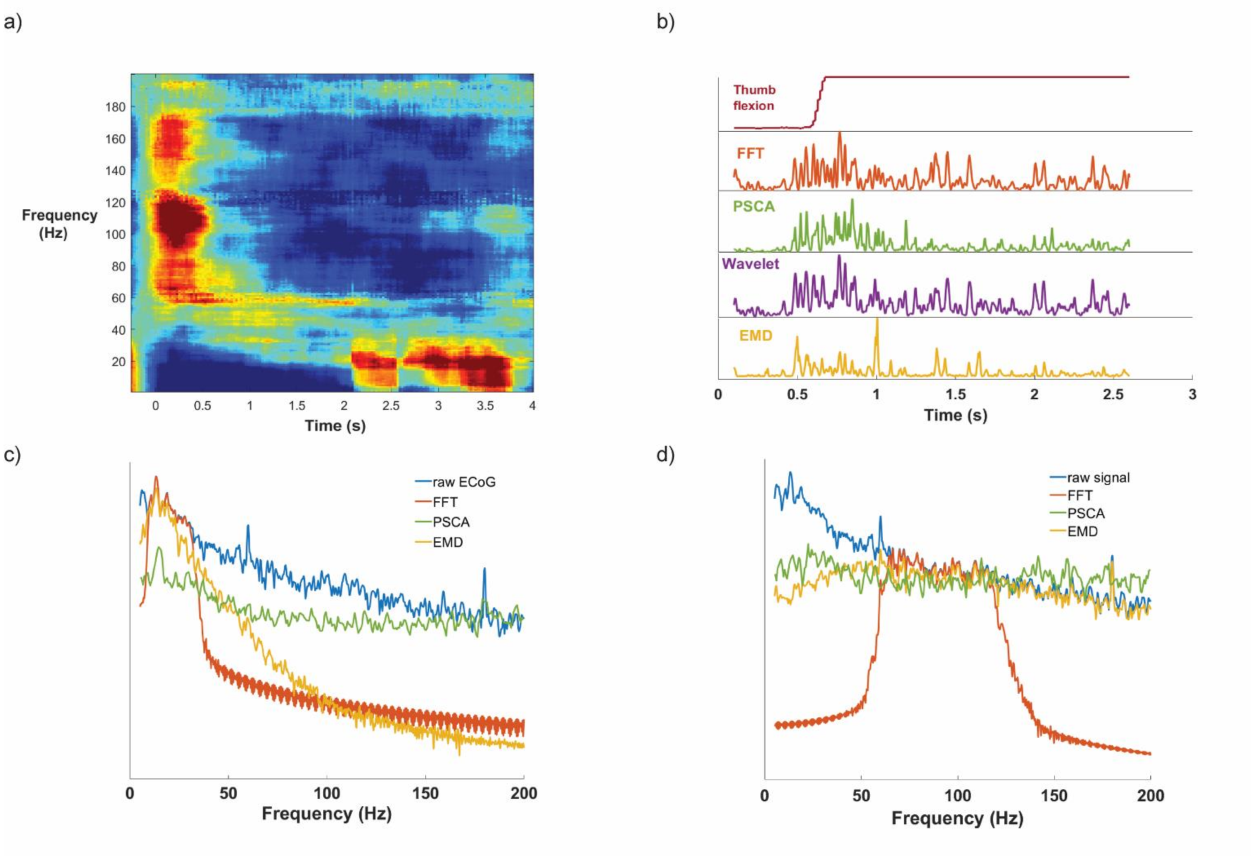

Figure 3-2 Neural signal analysis scheme. a) Multi-taper spectral analysis: finger flexion begins at t = 0, leading to a significant elevation ($p < 0.05$, 1-sided permutation test, false discovery rate corrected) in the gamma band (66-144 Hz) and a suppression in the beta band (10-30Hz) b) Gamma power burst following thumb flexion from a representative electrode, as decoded by each of the four algorithms. c) Spectral characteristics of beta. d) Spectral characteristics of gamma. FFT produces sharp cut-off bands in both cases, whereas the other three algorithms produce more varied spectra.

EMD was implemented using publicly available MATLAB code from Huang (Research Center for Adaptive Data Analysis, 2015), with envelopes calculated using standard not-a-knot spline interpolation. We specified the algorithm to decompose neural signals to 9 IMFs, as subsequent IMFs did not contain any signal. EMD is an empirical approach, so beta and gamma bands were assigned based on the power spectral densities of each IMF. Based on spectral characteristics, we chose the 5th IMF to represent beta band and the 3rd IMF for gamma band.

Finger flexion analysis

Processed ECoG data from each of the four algorithms was used to train two sets of Naïve-Bayes classifiers. Extracted log power of beta was used to detect thumb movement, and extracted gamma was used to predict finger flexions of the thumb, index, and little finger. Naïve-Bayes was chosen for its general simplicity, as well as its robustness to small training sets, which may lead to overfitting in more complex models (Duda *et al.*, 2012). Performance was measured using leave-one-out cross-validation.

Results

Multi-taper spectral analysis (Percival and Walden, 1993) shows gamma band synchrony and beta band depression during finger movement in a subset of electrodes (Figure 2(a)). Gamma band elevation was significant ($p < 0.05$, 1-sided permutation test, false discovery rate corrected). Relevant electrodes were selected for analysis based on the methods described in (Chestek *et al.*, 2013). Robust modulation of gamma power was observed on these electrodes during finger movement for all four algorithms (Figure 2(b)). Each of the four algorithms extracted different representations of beta and gamma bands (Figure 2(c) & 2(d)), with FFT producing the sharpest cut-offs.

For all four signal processing methods, classification using beta band power achieved above-chance detection of thumb movement across all datasets ($p < 10^{-3}$, binomial cumulative distribution test (Combrisson and Jerbi, 2015)) (Figure 3). The McNemar test found no significant difference in performance between any of the four algorithms.

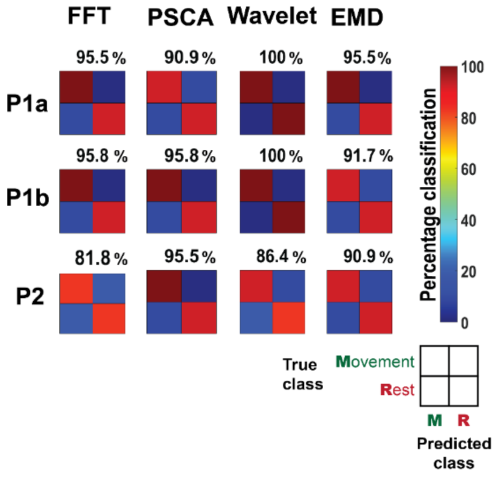

Figure 3-3 Finger movement detection using beta. Percentages above confusion matrices indicate classification accuracies. All algorithms could predict thumb movement onsets above random chance ($p < 10$-3).

In decoding finger flexions using gamma band power, the classifier achieved above chance prediction accuracies for all four algorithms ($p < 0.01$) (Figure 4). PSCA achieved an overall accuracy of 83% with a standard deviation of 4%, whereas FFT (75 ± 6%), WA (68 ± 5%), and EMD (56 ± 5%) achieved lower decoding accuracies. For all the three cases, the classification accuracies of PSCA and FFT were significantly greater than that of EMD ($p < 0.05$, McNemar test).

Discussion

An analysis of the accuracy data reveals noticeable differences between the performance of FFT, PSCA, WA, and EMD in processing human ECoG for a Naïve-Bayes classifier. When using extracted beta to detect thumb movement, all algorithms achieved similarly high performance. When using extracted gamma to decode finger flexions, all algorithms classified flexions with an above average chance, although performance across algorithms varied.

PSCA-extracted gamma produced the most consistently accurate classification results of the four algorithms. These results support the claim that neurophysiological signals are distributed over a broadband spectral distribution, rather than within clearly defined frequency bands. The adaptive nature of PSCA allows for active tuning of the processing pipeline, which could ensure reliable extraction of a wide variety of non-sinusoidal components. Other studies have demonstrated similar success with PSCA-extracted gamma in speech decoding (Kellis *et al.*, 2010; Miller *et al.*, 2011) and identification of visual stimuli (Miller *et al.*, 2009b; Miller *et al.*, 2010).

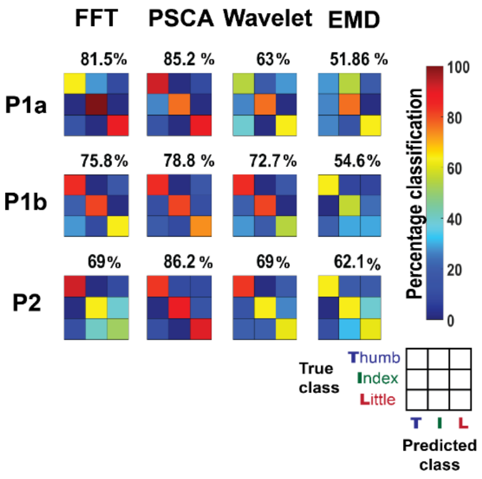

Figure 3-4 Finger flexion decoding using gamma. Percentage values above confusion matrices indicate classification accuracies. All algorithms could predict flexion above random chance ($p < 0.01$). Accuracies of PSCA and FFT are greater than EMD, in all the three cases ($p < 0.05$).

Although we did not observe significant differences in decoding performance between WA and FFT gamma, WA can be used to identify transients, a property that was not investigated in this study. This capability may be useful for analysis of time-variant phenomena and has been used to capture spikes (Lopes-dos-Santos *et al.*, 2014) and evoked potentials (Lopes-dos-Santos *et al.*, 2017) from neural oscillations.

EMD-extracted gamma exhibited the lowest performance of the four algorithms. The observed accuracy is comparable to previous work using EMD for finger flexion classification (Hazrati, 2012). The comparatively low performance of EMD-extracted gamma may be due to the EMD algorithm’s tendency to behave as a series of dyadic filter banks when decomposing signals with flat power spectral densities (Flandrin *et al.*, 2004). The broadness of the gamma band may cause the algorithm to behave as a bandpass filter with indeterminate cut-off frequencies, which may compromise neural information. In this analysis, we did not observe any mixing of spectral content in the resultant IMFs, precluding the need for noise assisted versions of EMD (Yeh *et al.*, 2010). However, more sophisticated forms of EMD such as multivariate empirical mode decomposition may be more suitable for decomposing high frequency gamma oscillations. This method has had success in predicting seizure onset from EEG (Cho *et al.*, 2017).

Since EMD appears to provide accurate estimates of beta, it may be useful for examining temporal patterns such as phase of low-frequency oscillations such as alpha and beta. Calculations of phase-amplitude coupling and phase-locking value, for example, benefit significantly from EMD-derived signals over traditional bandpass filtering (Pittman-Polletta *et al.*, 2014). Recent studies have even suggested that some observed phase-amplitude coupling values may arise spuriously from non-sinusoidal features in the phase-carrier oscillation, a phenomena that may be suitable for extraction by EMD (De Hemptinne *et al.*, 2013; Cole *et al.*, 2017; Cole and Voytek, 2018).

Our comparison test-case was based on the performance of a Naïve-Bayes classifier. The simplicity of this model compared to other widely used classifiers (SVMs, K-nearest neighbors, neural networks, etc.) makes it a good first choice for prototyping decoding pipelines. The particular characteristics of the chosen classifier may influence the resulting algorithm performance. Naïve-Bayes relies on an assumption of independent predictors, so processing algorthms that reveal greater interactions betweens features may have hindered performance (Bressan *et al.*, 2003). In future work that involves much larger neural datasets, a comparison of decoding algorithms with a more complex classifier would be prudent.

Conclusion

In summary, we compared the effectiveness of PSCA, WA, and EMD against standard FFT analysis of neural signals by training Naïve-Bayes classifiers to detect finger movements and decode finger flexions from human cortical signals. We found that all four algorithms were equally accurate in predicting finger movements using beta. In decoding finger flexions using gamma, PSCA produced the highest performance. Although WA and EMD-extracted gamma resulted in lower decoding performance, the two algorithms appear to operate well on lower frequencies and can extract temporal information not provided by PSCA and traditional bandpass filtering. These results can inform the development of decoding pipelines in future studies that require extraction of a specific quality from human ECoG data.

Chapter 4

Impedance-Guided Lead Localization

Co-authored with: Aidan D Ahamparam, Allison R Tichenor, Parag G Patil

Abstract

Background: Previous studies have reported variations in brain tissue impedance along deep brain trajectories. These properties have been associated with parameters of non-invasive imaging data. Using this relationship to localize deep brain leads may increase accuracy of lead placement for deep brain stimulation therapies that lack functional methods of validation.

Objective: Evaluate the feasibility of localizing deep brain leads using *in vivo* measured impedance and computational models of deep brain impedance.

Methods: Patient-specific diffusion-tensor-derived conductivity models were used simulate deep brain impedance measurements and create computationally efficient whole-brain models of tissue impedance. Wideband impedance measurements were measured along deep brain trajectories in living human subjects using the macro contact of a microelectrode lead and compared to simulated impedances. Trajectories were localized by comparing measured impedances to estimated values along potential trajectories in the vicinity of the surgical plan.

Results: Computationally efficient transforms of diffusion tensor-derived fractional anisotropy and maximum eigenvalue accurately approximated electrostatic simulations of impedance with a correlation of 0.93. Simulations of deep brain impedance indicated that locally measured impedance captures tissue properties from as far as 5 mm away from the measurement site. Patterns observed in simulated impedances were generally concordant with trends measured

in vivo. Impedance-guided localization of both hypothetical and implanted leads resulted in millimeter-scale errors.

Conclusions: These results demonstrate the feasibility of impedance-guided localization of deep brain leads. Although conceptually sound, measurement of impedance using macro contacts does not provide sufficient spatial resolution to perform precise localization.

Introduction

Deep brain stimulation (DBS) is an established treatment modality for a number of neurological disorders—most notably Parkinson disease, essential tremor, dystonia, and Tourette's syndrome—through electrical activation of precise anatomical targets. Across DBS indications, accuracy of electrode placement is a critical determinant of clinical success and failure (McClelland *et al.*, 2005; Okun *et al.*, 2005). However, stereotactic targeting technologies are limited in precision. Conventional approaches to lead placement incorporating imaging and stereotactic platforms achieve precisions of 1 to 2 mm (Schrader *et al.*, 2002; Holloway *et al.*, 2005; Bjartmarz and Rehncrona, 2007; Balachandran *et al.*, 2009; D'Haese *et al.*, 2010; Burchiel *et al.*, 2013; Lefranc *et al.*, 2014; von Langsdorff *et al.*, 2015; Koeglsperger *et al.*, 2019). An additional 2 to 4 mm of error can be contributed by brain shift (Winkler *et al.*, 2005; Khan *et al.*, 2008; Hunsche *et al.*, 2009).

For some applications of DBS, uncertainty in stereotactic accuracy can be compensated for by functional testing, such as intra-operative stimulation and recorded electrophysiology. This additional information can result in revisions of the initial implant in over half of cases (Frequin *et al.*, 2020). However, there exist several DBS indications for which intraoperative testing is currently infeasible. Notably, recent research has identified the subgenual cingulate (CG25) as a promising stimulation target for treatment-resistant depression (Mayberg *et al.*, 2005), and the anterior limb of internal capsule for treatment of substance use disorders (Chen *et al.*, 2019), among others (Lyketsos *et al.*, 2015; Herrman *et al.*, 2019; Huys *et al.*, 2019). Further development of these treatment modalities requires tools to more accurately verify intraoperative lead location.

Localization of lead location using cerebral tissue impedance was first proposed by Robinson, with the observation that changes in measured impedance corresponded to histological borders of brain structures (Robinson, 1962). Robinson and others then demonstrated that these variations in tissue impedance could be used to identify lead entry into specific structures *in situ* (Fry *et al.*, 1962; Robinson and Tompkins, 1964; Laitinen *et al.*, 1966; Johansson *et al.*, 2009). The clinical potential of this approach has been demonstrated by use of *in vivo* impedance to localize brain tumors (Bullard and Makachinas, 1987; Rajshekhar, 1992; Andrews *et al.*, 2009).

Here, we combine the principles pioneered by Robinson *et al.* with modern imaging technologies and computational models to find direct relationships between measured tissue impedances and detailed, patient-specific brain imaging data. We demonstrate that deep brain impedances correspond with location in diffusion tensor-derived conductivity models of the brain, show frequency-independent variations in *in vivo* measurements of tissue impedance, and apply these findings to a deep brain localization tool.

Methods

Subjects

Impedance and imaging data were measured from two patients with advanced Parkinson disease undergoing subthalamic deep brain stimulation surgery at the University of Michigan. Details of patient selection at the institution have been described in a previous publication (Patil *et al.*, 2012). All participants provided informed consent. The study was approved by the University of Michigan Institutional Review Board.

Surgical procedure

Subjects underwent awake, frame-based deep brain stimulation surgery, during which microelectrode recording and impedance measurements were performed. Planned targets were initially assigned from indirect targeting (12 mm lateral, 3 mm posterior, and 4 mm inferior to the mid-commissural point), with adjustment from direct magnetic resonance (MRI) visualization of the ventral border of subthalamic nucleus. Microelectrode recording to determine location of the subthalamic nucleus was performed using a NeuroProbe and Neuro Omega system (Alpha Omega, Alpharetta, GA). Locations of implanted electrodes were directly visualized via computed tomography two weeks after surgery.

Simulated impedance measurements

Pre-operative diffusion tensor imaging (DTI) data for each patient were acquired using a single-shot echo planar imaging sequence with a dS-SENSE parallel-imaging scheme (reduction factor = 2, field of view = 224 mm x 224 mm, 1 x 1 x 2 mm voxels). Diffusion weighting was encoded along 16 independent orientations with a b-value of 800 s/mm^2. Diffusion tensors were resampled via cubic spline interpolation to match the resolution of pre-operative imaging and oriented in Talairach space via coregistration to the Talairach-oriented images in Analyze (Analyze 12.0; Mayo Clinic, Rochester, MN). The Analyze software DTI application was used to calculate the eigenvectors and eigenvalues of the DTI images. Diffusion tensors were then calculated from the eigenvectors and eigenvalues in MATLAB (MATLAB R2019b; MathWorks, Natick, MA) and converted to conductivity tensors using the linear relationship between conductivity and diffusion tensor eigenvalues ($\sigma/d \approx 0.844$ S·s/mm^3) as described by Tuch et al. (Tuch *et al.*, 2001).

3D electrostatic finite element models incorporating individual brain anatomy, macroelectrode position and orientation, and anisotropic tissue conductivity were modeled in COMSOL (Multiphysics 5.5; COMSOL, Burlington MA). Bulk brain tissue was modeled as a sphere (8 cm radius) surrounded by concentric shells to model cerebrospinal fluid, skull, and scalp. Brain tissue was assigned diffusion tensor imaging-based anisotropic electrical conductivities linearly interpolated onto the mesh. The remaining domains—cerebrospinal fluid, skull, and scalp—were assigned isotropic resistivities of 56 ohm-cm, 16000 ohm-cm, and 230 ohm-cm, respectively (Sadleir and Argibay, 2007; Wendel *et al.*, 2010). The cerebrospinal fluid shell, skull shell, and scalp shell had inner and outer radii of 8 cm and 8.8 cm, 8.8 cm and 9.3 cm, and 9.3 cm and 10 cm, respectively. Ground was defined as a 1x1x0.1 cm block at the bottom of the scalp shell. The macro electrode at which impedance was measured was modeled after the macro contact of the NeuroProbe (1 mm length, 0.56 mm diameter). The cylindrical lead had an outer diameter of 0.46 mm, an inner diameter of 0.200 µm, and a length of 1 mm. The macro contact was translated and rotated to match locations where impedance was measured *in vivo*.

A boundary condition of 1-amp current was applied to the surface of the macro contact. Simulations solved for the resulting voltage at the macro contact, which was then converted to measured impedance by application of Ohm's law.

Approximation of impedance from diffusion tensors

Diffusion tensor values were used to approximate COMSOL-simulated impedances to provide a scalable method to estimate whole-brain impedances. Fractional anisotropy (FA) was used to estimate impedance ($\hat{z}_{FA}$) using a cubic relationship,

$$\hat{z}_{FA}(FA) = aFA^3 + bFA^2 + cFA + d$$

Where a, b, c, and d are fitted parameters. Maximum eigenvalue (λ) of tensors were fit to impedance ($\hat{z}_\lambda$) using an exponential decay function:

$$\hat{z}_\lambda(\lambda) = ae^{-b\lambda} + c$$

Where a, b, and c are fitted parameters. Expected values from the two functions where then averaged and smoothed with a 3D Guassian filter (σ = 2 voxels ≈ 1 mm) to predict COMSOL-simulated impedances.

In vivo impedance measurement

Impedance measurements were performed along trajectories parallel to the microelectrode recording, but offset by 2 mm. The use of a separate trajectory was necessary due to the formation of edema by each electrode pass, which would affect both impedance measurements and microelectrode recording. Monopolar impedance measurements were made using a commercially available battery-powered LCR meter (880 LCR Meter; B&K Precision, Yorba Linda, CA). The positive contact of the LCR meter was connected to the macro contact of the microelectrode, and return connected to a stimulating EMG surface lead attached to the subject's right clavicle. This configuration established a distal and relatively large current sink, producing impedance measurements localized to the site of the macro contact (Newman, 1966). Other electronic recording devices, including the Neuro Omega recording contacts, were detached from the patient for the duration of impedance measurement. Custom software (LabVIEW 2019; National Instruments, Austin, TX) was used to control the LCR meter to measure complex impedance measurements at 100 Hz, 1 kHz, 10 kHz, and 100 kHz. Measurements were made from 15 mm above to 5 mm below the planned target, in 0.5 mm steps.

Impedance-guided trajectory localization

In order to identify the most likely location of the lead based on impedance, measured impedance values along the DBS trajectory were compared to estimated impedances along plausible trajectories within the vicinity of the planned approach using Python (Python 3.6; Python Software Foundation). An initial search analyzed the 3x3x3 mm volume around the planned target with a uniform 9x9x9 grid and an equal number of randomly selected points. Plausible ring and arc values within 3 degrees of the planned values were also searched in a similar manner, resulting in a total of 119,000 potential trajectories. Best-fit trajectories were ranked using Pearson's correlation coefficient. This process was then iterated with the three best-fit trajectories at each stage, with a 30% reduction in search dimensions until the search window reached 0.1 mm.

Results

Spatial variance of simulated impedances

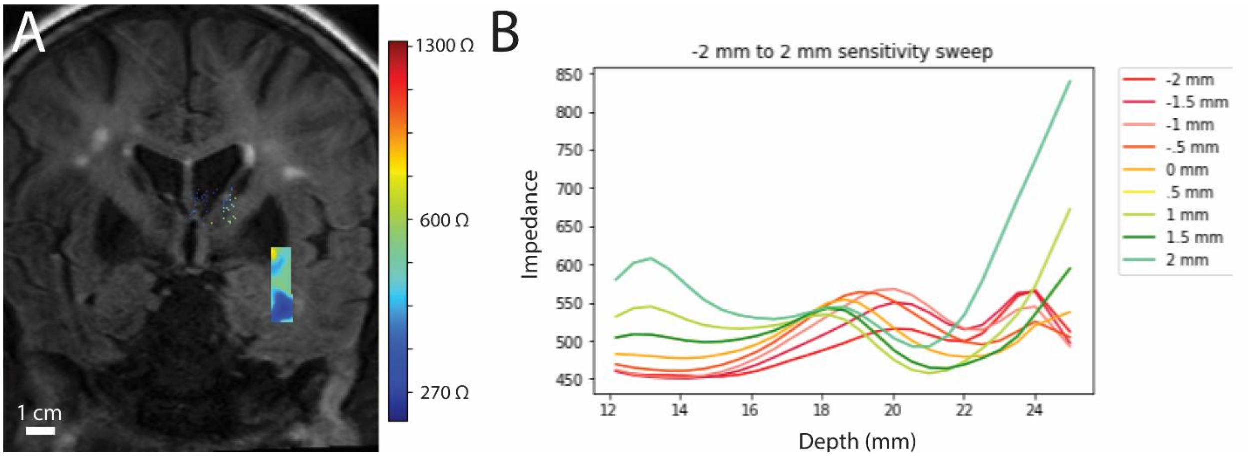

Figure 4-1 COMSOL-simulated impedances of deep brain tissue. A) COMSOL-simulated impedances (color; red: high impedance, blue: low impedance) overlaid on 3T MRI (grayscale). Note regionally depressed impedance measurements around areas of cerebrospinal fluid (left lateral ventricle and temporal horn of lateral ventricle). B) COMSOL-simulated impedance of parallel trajectories spaced 0.5 mm apart.

Simulation of locally measured impedances in the region of basal ganglia indicate significant variety in local impedance (Figure 1A). Observations of locally depressed impedances both within and around regions of cerebrospinal fluid suggest that nearby tissues can affect measured impedance from up to 5 mm away. An analysis of local impedances along parallel trajectories 0.5 mm apart (Figure 1B) indicate that impedance topographies could appear highly similar across parallel trajectories up to 2 mm apart. These simulation results suggest that while measured impedance is related to regional tissue properties, information is limited to millimeter-scale resolution.

DTI estimates of finite element model impedance

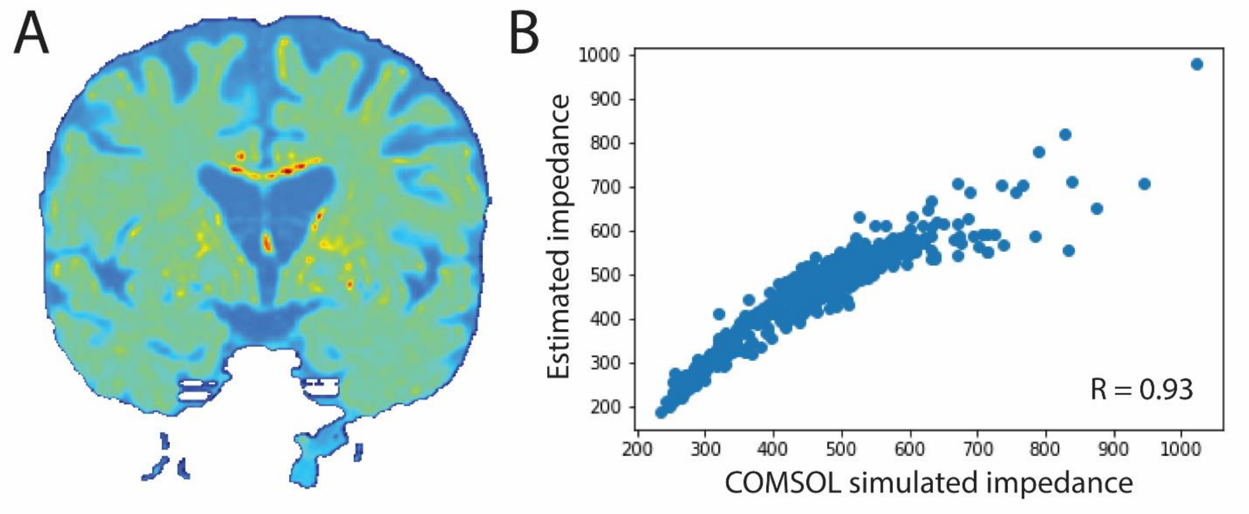

Figure 4-2 Computationally efficient estimation of whole-brain impedance. A) Whole-brain estimation of local impedance calculated from fractional anisotropy and maximum eigenvalues of conductivity tensors. Values range between 100 and 1000 Ohms. B) Conductivity tensor-based estimates of local impedance plotted against COMSOL-simulated impedances at the same sites.

In order to predict impedances at a whole-brain scale, a more efficient method of estimating impedance from imaging data was developed. COMSOL simulations of sites near the basal ganglia were used to define a relationship between COMSOL-simulated impedances and two conductivity tensor properties: fractional anisotropy and maximum eigenvalue. Fractional anisotropy and maximum eigenvalue were used to approximate COMSOL impedances via cubic and exponential decay transforms, respectively, providing an accurate and computationally efficient estimate of impedances across the entire brain (Figure 2A). Impedance predictions by fractional anisotropy and maximum eigenvalue matched COMSOL-simulated impedances with a correlation of 0.93 (Figure 2B).

Impedance-guided localization of deep brain trajectories

Table 4-1 Trajectory error for hypothetical targets.

Implant	Trajectory	
	Impedance-matched	Starting trajectory
Subthalamic nucleus	2.05	0.92
Ventral intermediate thalamus	3.12	3.61
Globus pallidus internus	4.12	4.44
Anterior limb of internal capsule	2.50	2.77
Errors shown in millimeters.		

Impedances along four DBS trajectories were simulated in COMSOL: subthalamic nucleus, ventral intermediate thalamus, globus pallidus internus, and anterior limb of the internal capsule. The simulated impedances along each trajectory were then compared to estimated impedances along DBS trajectories in the vicinity of the known trajectory. The algorithm was provided with a starting trajectory with random error of up to 3 mm (in the X, Y, and Z directions) and 3 degrees (in ring and arc). In three out of four test cases, the trajectory with the most similar impedance topography approached the correct trajectory (Table 1). However, errors of multiple millimeters were consistently observed.

Spatial and spectral variance of in vivo impedance measurements

In vivo measurements of impedance found values within the range described by previous literature (McIntyre *et al.*, 2006). While absolute impedances differed across frequencies (Figure 3A), topographies were similar across frequency once baseline was removed (Figure 3B), with correlation coefficients across different frequencies ranging from 0.85 to 0.98. Normalized impedance topographies revealed clear changes across depth. Spectral characteristics of impedance measured at each depth were also highly similar (Figure 3C,D), confirming that brain tissue exhibits largely non-capacitive impedance from 1 Hz to 100 kHz, as previously shown (Nicholson, 1965; Robinson *et al.*, 1965). Differences in absolute impedance across frequencies were likely due to equipment, equipment-tissue interfaces, and tissues distal to the electrode.

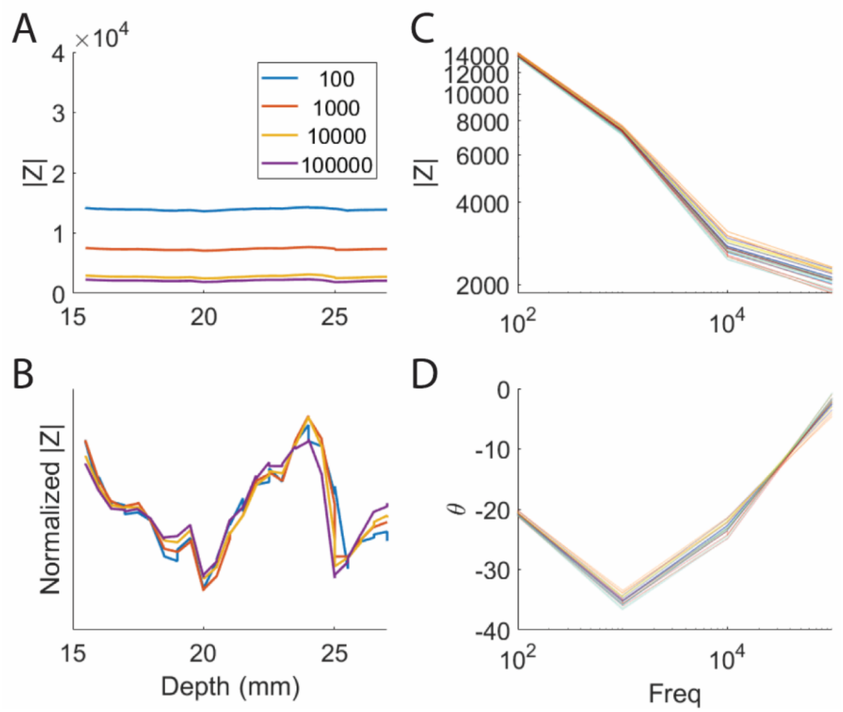

Figure 4-3 Impedance profiles along the trajectory of an exemplary DBS implant. A) Absolute impedance across each depth along an implant, measured at 100 Hz, 1 kHz, 10 kHz, and 100 kHz. B) Absolute impedances normalized to a shared scale. C) Absolute impedance across frequency. Each line represents a measurement taken from a different depth. Blue lines correspond to shallow sites, while red lines correspond to deeper sites. D) Phase measurements with respect to the input signal across frequency.

When impedance topographies were compared to electrophysiology recorded along parallel trajectories (Figure 4), the occurrence of impedance changes broadly coincided with changes in multiunit activity, approximated by 1000-2000 Hz power in the recorded neural signal. Changes in impedance were less sharp than changes in electrophysiology. Some discordance between trends was expected due to the 2 mm separation between tracks used for impedance and electrophysiology measurement.

Comparison of measured impedances to COMSOL-simulated values along the same trajectory also revealed general concordance (R = 0.84). Simulated impedance magnitudes exhibited spans of 80 and 438 Ω in the two models for which data was available, while measured impedances spanned 1.1 and 1.7 kΩ, respectively.

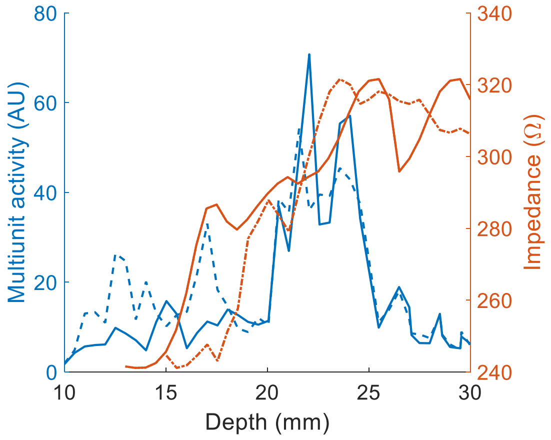

Figure 4-4 Multiunit activity, measured *in vivo* impedance, and COMSOL-simulated impedance plotted against depth. Dotted and solid blue lines indicate multiunit activity along the central and posterior (2 mm from central) trajectories of an implant, with elevated activity at 20-25 mm indicating subthalamic nucleus. Red lines indicate measured impedance at 1000 Hz (dotted; values scaled to fit axis) and COMSOL simulated impedance (solid) along the medial track, 2 mm from central.

In vivo impedance-guided localization

Two intraoperatively measured impedance topographies were compared to estimated impedances along trajectories within the neighborhood of the surgical plan. In each case, a trajectory with a highly correlated impedance topography was found (R = 0.99 and 0.89). However, the impedance-matched trajectory target differed from the CT-visualized trajectory by more than the difference between the planned trajectory and CT-visualized trajectory (Figure 5, Table 1).

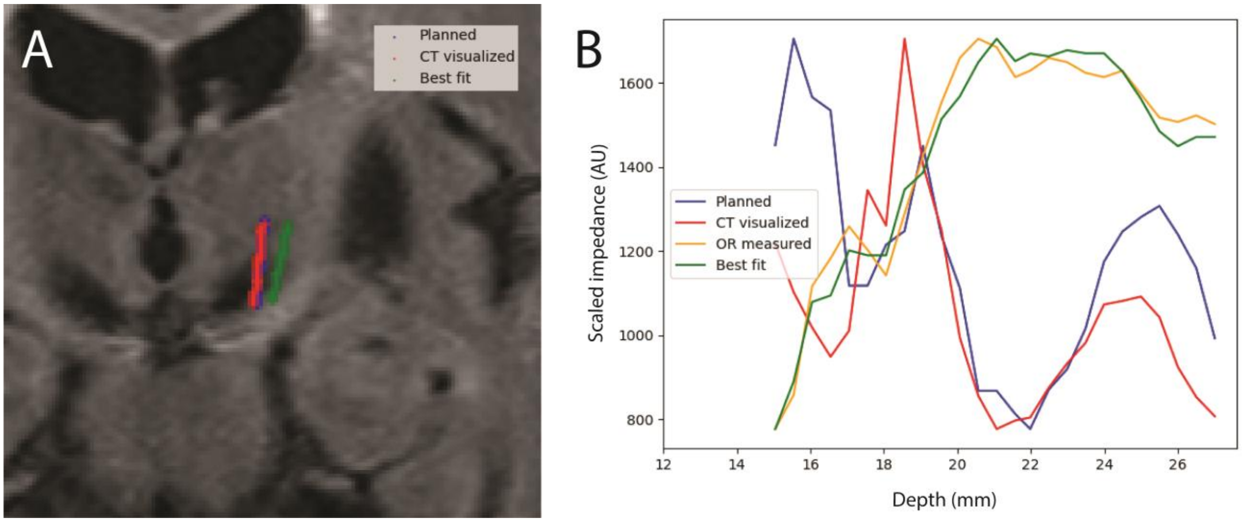

Figure 4-5 Representative best-fit trajectory alongside planned and CT-visualized trajectories. A) The planned (blue), CT-visualized (red), and impedance best-fit (green) trajectories overlaid on the patient 3T MRI. B) The estimated impedance topographies of the planned, CT-visualized, and impedance best-fit trajectories, plotted alongside the OR-measured impedance values (yellow).

Table 4-2 Differences between trajectories and CT-visualized lead locations.

Implant	Trajectory	
	Impedance-matched	Planned
1	4.67	0.95
2	6.56	4.71

Differences shown in millimeters.

Discussion

While variability in brain tissue impedance has been previously observed (Robinson, 1962), this study is the first to combine impedance measurements with sophisticated computational models and contemporary imaging technologies. By combining *in vivo* measurements with patient-specific computational models of tissue impedance, this study assesses the feasibility of using local impedance to localize deep brain leads. We validated a computationally efficient, scalable model of whole-brain impedance and showed that impedance measurements provide information about local tissue properties at a spatial resolution of millimeters. We also demonstrate that *in vivo* measurements of impedance vary across deep brain trajectories and are largely concordant with trends observed in imaging-based models. Impedance-guided localization of deep brain leads, however, yielded errors of multiple millimeters.

The results here indicate that local impedance, as measured in this study, does not provide sufficient spatial resolution to precisely determine lead location. This is likely due to the relatively large size of the macro contact, which results in a large volume of measured tissue (Newman, 1966). Additional spatial error may also have been contributed by tissue shift occurring during electrode movement. Curiously, the spans of values observed in measured and simulated impedances differed by roughly an order of magnitude. While the scale of this discrepancy is not unusual (McIntyre *et al.*, 2006), it does suggest potential for more accurate modeling of deep brain impedances from imaging data.

Importantly, the concordance of measured and computational results does indicate the conceptual feasibility of impedance-guided localization, given improvements in spatial resolution of impedance measurements. The observation of significant changes in impedances measured *in vivo* and creation of a scalable whole-brain model of local impedance demonstrate that this approach can provide meaningful spatial information. Attainment of necessary improvements is straightforward, with use of either smaller contacts or implementation of multi-contact configurations for impedance measurements. Measurements at additional sites along parallel trajectories would also improve accuracy by providing additional fitting constraints.

The need for additional such tools is highlighted by the rapidly expanding list of indications for DBS. Notable emerging DBS treatments include major depression targeting the cingulate gyrus (Mayberg *et al.*, 2005), substance use disorders targeting nucleus accumbens or the anterior limb of the internal capsule (Chen *et al.*, 2019), and Alzheimer dementia targeting the fornix (Lyketsos *et al.*, 2015). While classical indications of DBS, such as Parkinson disease and essential tremor, can benefit from functional validation of lead placement, most emerging indications are not amenable to robust intra-operative testing. With suboptimal placement of DBS electrodes accounting for roughly half of lead revisions (McClelland *et al.*, 2005) and failed surgeries (Okun *et al.*, 2005), tools such as impedance-guided localization are necessary to maximize the clinical potential of these interventions.

This potential innovation would exist within a diverse ecosystem of targeting technologies. The foundation of conventional deep brain surgical targeting relies on stereotactic neurosurgery informed by pre-operative MRI. However, stereotactic targeting when used alone is limited by intrinsic inaccuracies of 1 to 2 mm (Koeglsperger *et al.*, 2019) and effects of brain shift (Hunsche *et al.*, 2009). Microelectrode recordings offer a highly precise complement to stereotactic approaches, although the technique requires skilled operation and is applicable only to a select subset of anatomical targets that exhibit distinguishable electrophysiology. Notably, intra-operative magnetic resonance imaging may overcome many of these limitations, but the high cost of specialized instrumentation and expertise preclude its use in many settings (Kubben *et al.*, 2011). Impedance-guided localization, if realized, would offer an intuitive and low-cost supplement to existing technologies.

Chapter 5

Analgesic Stimulation of Zona Incerta

Co-authored with: Daniel E Harper, Asra Askari, Matthew S Willsey, Philip P Vu, Andrew D Schrepf, Steven E Harte, Parag G Patil

Abstract

Background: Stimulation of zona incerta in rodent models has been shown to modulate perception of pain. Sensory changes observed in Parkinsonian patients with subthalamic deep brain stimulation suggest that this effect is translatable to humans.

Objective: Utilize the serendipitous placement of subthalamic deep brain stimulation leads to directly investigate the effects of zona incerta stimulation on human pain perception.

Methods: Twelve Parkinson disease patients with subthalamic deep brain stimulation implants were asked to rate perceived pain from non-painful and painful heat stimuli and undergo mechanical pressure pain threshold testing. Pain measurements were conducted while subjects received contralateral zona incerta deep brain stimulation at 20, 60, or 130 Hz in a double-blinded fashion. Effects of stimulation on pain perception and pressure pain threshold were assessed using a mixed linear model.

Results: Stimulation at the physiological firing frequency of zona incerta reduces heat pain by a modest but significant amount, achieving a 30% reduction in one fifth of implants. Modulation is selective for heat pain and was not observed in non-nociceptive heat or mechanical pressure pain threshold.

Conclusions: These findings provide a mechanistic explanation of sensory changes seen in subthalamic DBS patients and identify zona incerta as a potential target for neuromodulation of pain.

Introduction

Deep brain stimulation (DBS) has been used for treatment of pain since the 1970s. Classical targets—sensory thalamus, periaqueductal gray, and periventricular gray matter—are often able to provide pain relief, although long-term success of these interventions varies widely across etiologies. While DBS treatment of phantom limb pain, failed back surgery syndrome, and trigeminal neuropathy is frequently successful, outcomes for treatment of pain from other etiologies, including stroke, peripheral neuropathy, and brachial plexus injury, tend to be less satisfactory (Kumar *et al.*, 1997; Boccard *et al.*, 2013; Frizon *et al.*, 2020). The many pain patients for whom conventional DBS remains ineffective highlight the need for new targets of neuromodulation.

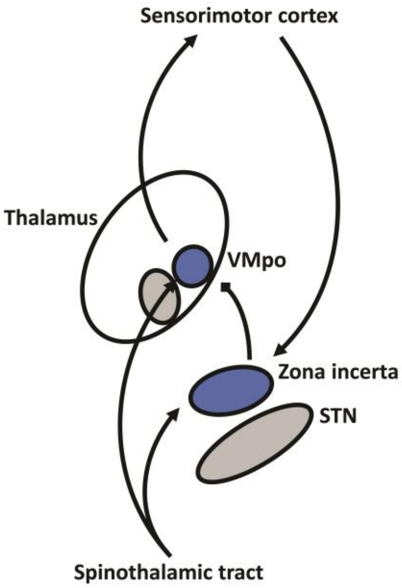

Figure 5-1 Feedforward inhibition of thalamic pain processing by zona incerta. VMpo: ventromedial posterior nucleus.

Strong evidence points to zona incerta, a heterogeneous region of cell bodies and fibers dorsal to subthalamic nucleus, as a promising new target for analgesic neuromodulation. The region receives direct spinothalamic input and projects GABAergic efferents to ventromedial thalamus, which integrates cortical and spinothalamic inputs (Figure 1) (Barthó *et al.*, 2002; Mitrofanis, 2005). In rodents, zona incerta has been shown to act as a feedforward inhibitor of pain perception, playing a key role in central pain syndromes (Masri *et al.*, 2009). The same group later demonstrated that 50-60 Hz stimulation of zona incerta reduces hyperalgesia in a rat model of neuropathic pain, providing a proof of concept for analgesic zona incerta DBS (Lucas *et al.*, 2011). More recent works have established compelling causative links between GABAergic output from zona incerta, neuropathic pain, and neuromodulatory relief of hyperalgesia and allodynia (Whitt *et al.*, 2013; Moon and Park, 2017; Hu *et al.*, 2019).

Experimental findings in rodent models have been corroborated by observations of sensory changes in human patients receiving subthalamic DBS. Although subthalamic DBS for Parkinson disease nominally targets the subthalamic nucleus, a large body of work has shown that most active contacts are located at or above the dorsal border of the subthalamic nucleus—a region directly adjacent to and overlapping zona incerta (Plaha *et al.*, 2006; Maks *et al.*, 2009). While the intervention is best recognized for its suppression of parkinsonian motor symptoms, it is also known to have substantial therapeutic effects on pain and sensation (Oshima *et al.*, 2012; Surucu *et al.*, 2013; Jung *et al.*, 2015; Belasen *et al.*, 2017; Custozzo *et al.*, 2020). Multiple studies show that this effect is not explained by motor improvements alone (Marques *et al.*, 2013; Cury *et al.*, 2016), indicating an independent mechanism by which subthalamic stimulation ameliorates pain symptoms. Taken together, these observations strongly suggest that stimulation of zona incerta modulates pain perception.

In this study, we utilized the serendipitous placement of subthalamic DBS leads in patients with Parkinson disease to directly evaluate the effects of zona incerta DBS on human perception of experimental heat and mechanical pain. A broad set of stimulation parameters were tested and then prospectively validated in independent cohorts, showing that stimulation at physiological frequency modulated perceived heat pain by a modest but significant amount. Modulation was specific to heat pain and did not significantly alter perception of non-painful heat or mechanical pain threshold. These findings provide a mechanistic explanation of sensory changes seen in subthalamic DBS patients and identify zona incerta as a potential target for neuromodulation of pain.

Methods

Subjects

Table 5-1 Subject characteristics. GDSS: Geriatric Depression Scale Short Form score. Duration of DBS measured from time of implant to time of study.

Age	Sex	GDSS	Duration of DBS, months	Experiment	Data inclusion
62	M	4	55	Exploratory	Bilateral
58	M	2	18	Exploratory	Bilateral
62	M	2	64	Exploratory	Excluded
67	M	2	13	Exploratory	Bilateral
58	F	1	65	Exploratory	Bilateral
71	M	2	59	Exploratory	Bilateral
73	M	2	7	Exploratory	Unilateral
45	M	1	22	Validation	Bilateral
62	F	11	6	Validation	Bilateral
60	M	3	40	Validation	Bilateral
73	F	2	42	Validation	Bilateral
66	M	2	38	Validation	Unilateral

Outpatient experiments were performed with 9 male and 3 female patients previously implanted with subthalamic DBS leads for treatment of Parkinson disease at the study institution. Patient selection criteria for subthalamic DBS at the institution have been described previously

(Patil *et al.*, 2012; Houshmand *et al.*, 2014). All patients were implanted with Medtronic (Dublin, Ireland) DBS leads, model 3389, with guidance by 3T magnetic resonance imaging (MRI), stereotactic navigation, and microelectrode recording. Subjects were implanted at least six months prior to the study and had stable, effective programming parameters. Prior to study, outpatient subjects were screened for depression using the Geriatric Depression Scale Short Form (Yesavage and Sheikh, 1986). The study was approved by the study institution's Institutional Review Board, and all participants provided individual informed consent.

DBS lead placement

DBS targets were initially assigned from indirect targeting (12 mm lateral, 3 mm posterior, and 4 mm inferior to the mid-commissural point) and adjusted with direct visualization of the ventral border of subthalamic nucleus on 3T MRI (Philips Achieva 3T; Philips, Amsterdam, Netherlands). Microelectrode signals were recorded with a Neuroprobe amplified by a Neuro Omega system (Alpha Omega, Alpharetta, GA). Recordings were performed from 15 mm above to 5 mm below the planned target. An experienced electrophysiologist identified the location subthalamic nucleus during surgery. DBS leads were inserted with the tip near the electrophysiologically defined ventral border of subthalamic nucleus. Pulse generators were implanted and connected to DBS leads within 14 days of lead implantation. High-resolution computed tomography scans (GE HD750; General Electric, Boston, MA) were acquired two to four weeks after surgery to verify lead locations.

Estimation of stimulation sites

Post-operative computed tomography scans were co-registered with magnetic resonance images using commercial software (Analyze; AnalyzeDirect, Overland Park, KS). Coordinates of DBS contacts were recorded, alongside coordinates of the subthalamic nucleus midpoint and its mediolateral, dorsoventral, and anteroposterior spans. Coordinates were linearly transformed into a common space with a shared orientation (left brain) and subthalamic nucleus midpoint. Coordinates for each contact were then scaled according to the size of its corresponding subthalamic nucleus to preserve relative anatomical locations. Scaled leads were then visualized within a representative magnetic resonance image to approximate the anatomical location of contacts used to deliver stimulation.

Deep brain stimulation

Neuromodulation of zona incerta was achieved using the implanted DBS leads and pulse generators by delivering stimulation to the DBS contact closest to 1.5 mm above the dorsal border of electrophysiological subthalamic nucleus. Three different stimulation frequencies were used: 20 Hz, 60 Hz, and 130 Hz; which reflect the frequency of observed human ZI activity (Merello *et al.*, 2006), the frequency of analgesic ZI stimulation in rats (Lucas *et al.*, 2011), and the frequency of conventional subthalamic DBS stimulation, respectively. Stimulation was delivered contralateral to the side of sensory testing with 60 µs charge-balanced pulses and voltage at 0.5 V below sensory threshold at 130 Hz, with a maximum of 2.0 V. Stimulation settings were set by an experienced clinician using a clinical programmer, with subject and experimenter blinded to stimulation settings. Estimated simulation sites for subjects in the Exploratory experiments (see *Experiment design*) are shown in Figure 2A.

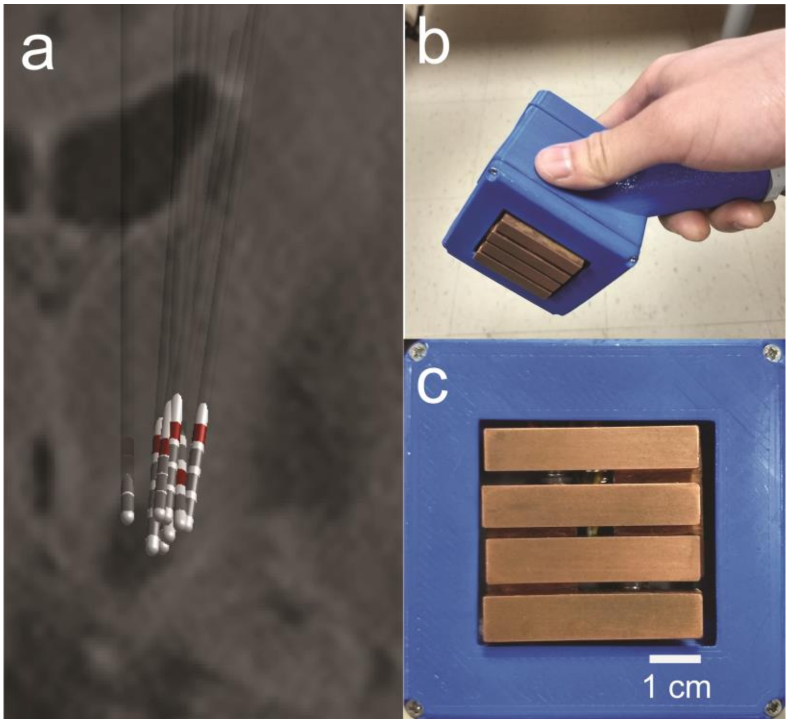

Figure 5-2 Deep brain stimulation sites and thermal stimulation device. a. Estimated lead locations in subjects participating in exploratory experiments juxtaposed against a representative magnetic resonance image. Active contacts used in the study are indicated in red. b. Device used to produce thermal stimuli. c. Detail of device contact surface.

<u>Thermal stimulation</u>

A custom device was used to provide thermal stimuli. The contact surface is composed of four parallel copper bars (9x10 mm surface), shown in Figure 2B, with temperature controlled by Peltier devices. Two distinct stimuli were produced with the device: nonpainful *Warm* stimuli were produced by setting bars to 39 °C; painful *Hot* stimuli were achieved by setting bars to 45 °C, or the highest temperature tolerable by the subject (always greater than 41 °C).

Thermal stimuli were applied to three sites along the volar forearm: proximal aspect, midpoint, and distal aspect, centered along midline. Each thermal stimulus was tested once at each site for each DBS setting. Application of thermal stimuli followed the sequence listed above with at least 30 seconds of rest between successive applications. After application of each thermal stimulus, patients were asked to separately rate the intensity (See Supplement) and pain of each thermal stimulus on a 10-point scale, with 0 signifying “no sensation/pain” and 10 signifying the “most intense/painful sensation imaginable.”

Mechanical stimulation

Algometry was performed using an Algometer type II device (SBMEDIC Electronics, Solna, Sweden) upon the belly of the extensor digitorum muscle. Three measurements of pressure pain threshold were performed for each test case at locations roughly 1 cm apart. Measurements across test cases were performed at overlapping but non-identical locations.

Experiment design

Exploratory experiments

A set of experiments evaluating the effects of 20, 60, and 130 Hz zona incerta stimulation on perceptions of warm, hot, and mechanical stimulation was performed bilaterally with seven outpatient subjects.

Each DBS setting was applied for 15 minutes. The first ten minutes involved no sensory testing to allow for wash-in of potential slow-acting effects. The last five minutes were used to perform sensory testing. Thermal stimuli (warm, hot) were tested in randomized order, counterbalanced across DBS settings. Algometry was performed after thermal testing. Patients were tested unilaterally on one side first, then the other. The first and last DBS settings were sham stimulation. The order of 20, 60, and 130 Hz stimulation was randomized. The experimenter was blinded to stimulation frequency. Test subjects were blinded to stimulation setting (sham and frequency) and thermal stimulation paradigm.

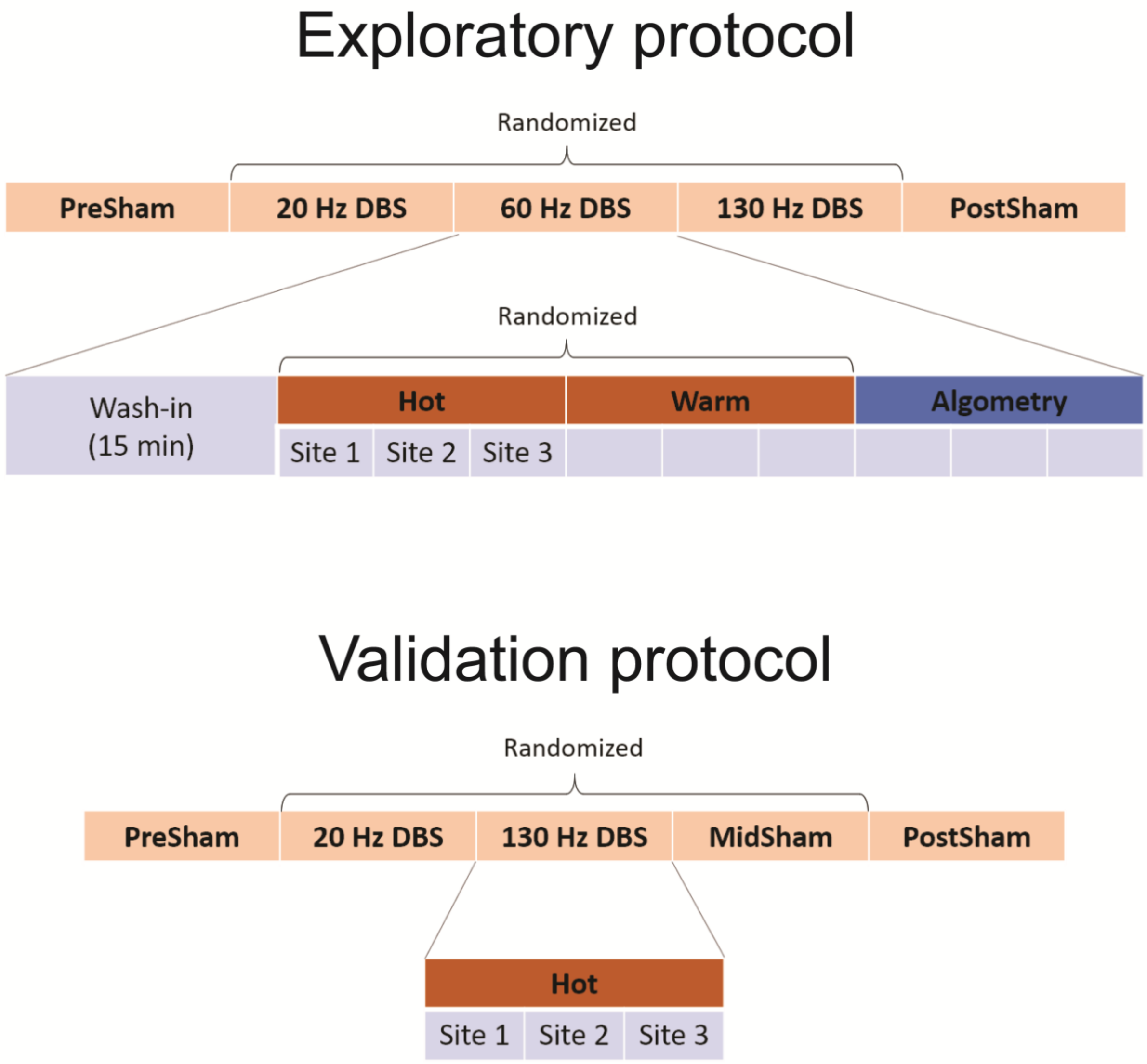

Figure 5-3 Experimental protocols. Order of randomized DBS settings were hidden from both subject and experimenter. Order of randomized thermal stimuli were hidden from subject.

Validation experiments

A second set of experiments was performed on an independent cohort of five subjects to evaluate the effects of 20 and 130 Hz zona incerta stimulation on perceived heat pain.

Validation experiments followed a similar protocol to that of exploratory experiments, described above. However, no wash-in time was provided. Instead, thermal stimulation followed immediately (within five minutes) after application of DBS settings. Only hot stimuli were used for sensory testing. In addition, 60 Hz stimulation was replaced with another period of sham stimulation for three of the five subjects. Subjects remained blinded to all deep brain stimulation and sensory stimuli settings. Experimenter was blinded to order of stimulation parameters (including the additional sham period).

Statistical analysis

A mixed linear model controlling for differences in patient baselines ($\beta_{subject}$) and habituation over time (β_{habit}) was used to determine the effect and significance of each intervention by zona incerta stimulation (β_{DBS}).

$$VAS = \beta_{subject} + \beta_{habit} trialNumber + \beta_{DBS} DBS$$

Each implant was treated as an individual subject during statistical analysis. As such, results obtained from contralateral sides of bilaterally tested subjects were assumed to be independent and have different baselines. Sham stimulation trials were shared across interventions.

Results

Subjects

Subjects scored an average of 3.1 points (standard deviation of 2.5 points) on the Geriatric Depression Scale Short Form, with one subject (at 11 points) exceeding the 10-point cutoff for depression risk (included in analysis) (Table 1). One subject was a non-responder to hot stimuli up to 45 °C and was excluded from all analyses. Results were collected unilaterally on one subject due to scarring on one arm from previous traumatic injury. Unilateral data from one subject was excluded due to misinterpretation of subject instructions. No subjects reported pre-existing pain in the areas examined in this study.

Zona incerta DBS modulates heat pain

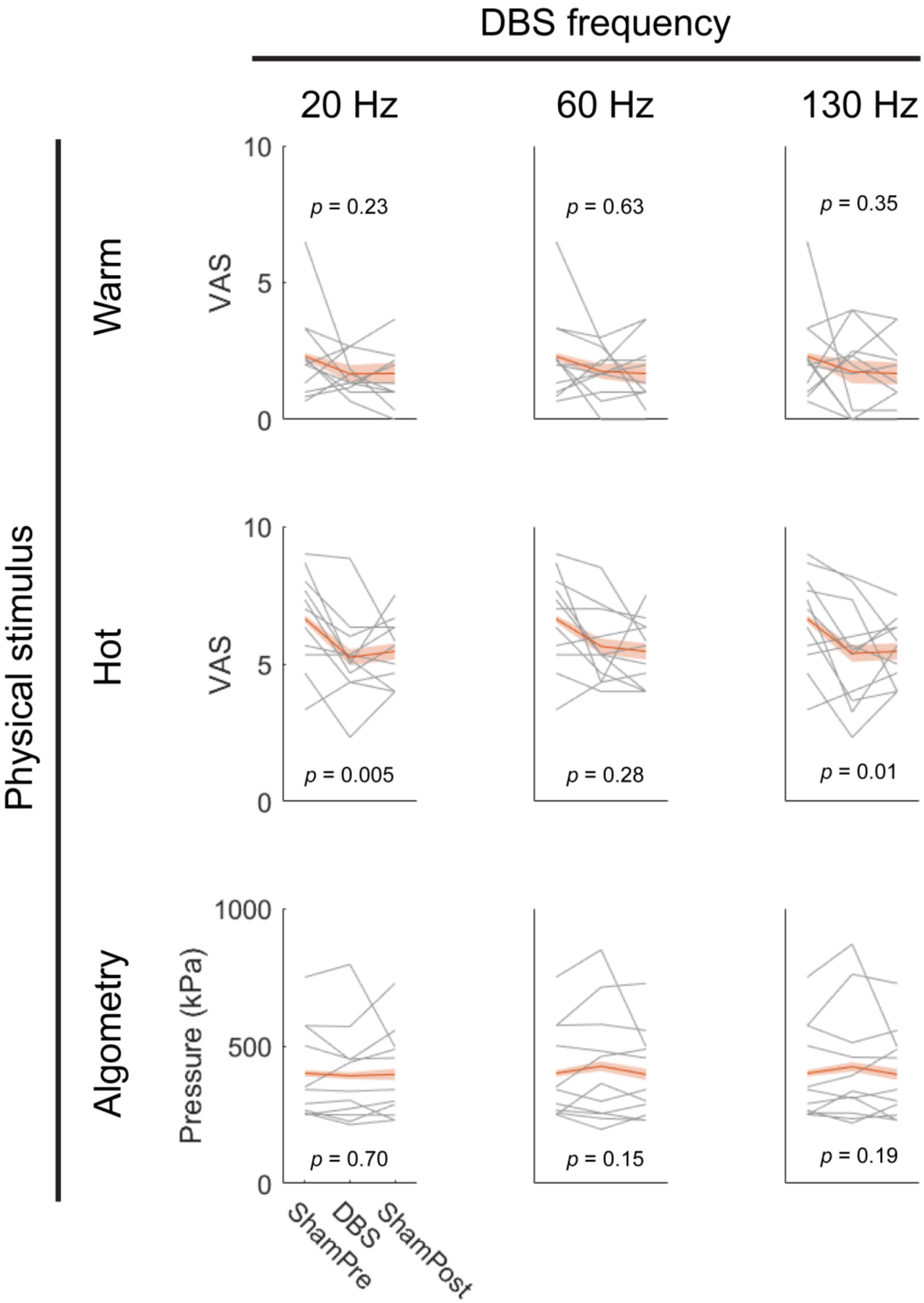

Figure 5-4 Effects of DBS on perceived pain from warm stimuli, hot stimuli, and mechanical pressure. Gray lines show mean pain scores across arm sites for each subject-implant. Red lines show average across implants with standard error of the mean shaded. n = 99 trials for all analyses shown, with sham trials shared across DBS frequencies.

Zona incerta DBS with conventional 130 Hz stimulation decreased perceived heat pain by 0.71 points (*p*=0.01) on the visual analog scale (Figure 4). Low frequency 20 Hz stimulation reflecting physiological firing of zona incerta also reduced pain elicited by hot stimuli, relative to sham trials (-0.78 points; *p*=0.005). DBS of any frequency did not appear to significantly affect perceived pain from warm stimuli (20 Hz, *p*=0.23; 60 Hz, *p*=0.63; 130 Hz, *p*=0.35) or mechanical pain thresholds (20 Hz, *p*=0.70; 60 Hz, *p*=0.15; 130 Hz, *p*=0.19).

Validation of 20 and 130 Hz stimulation

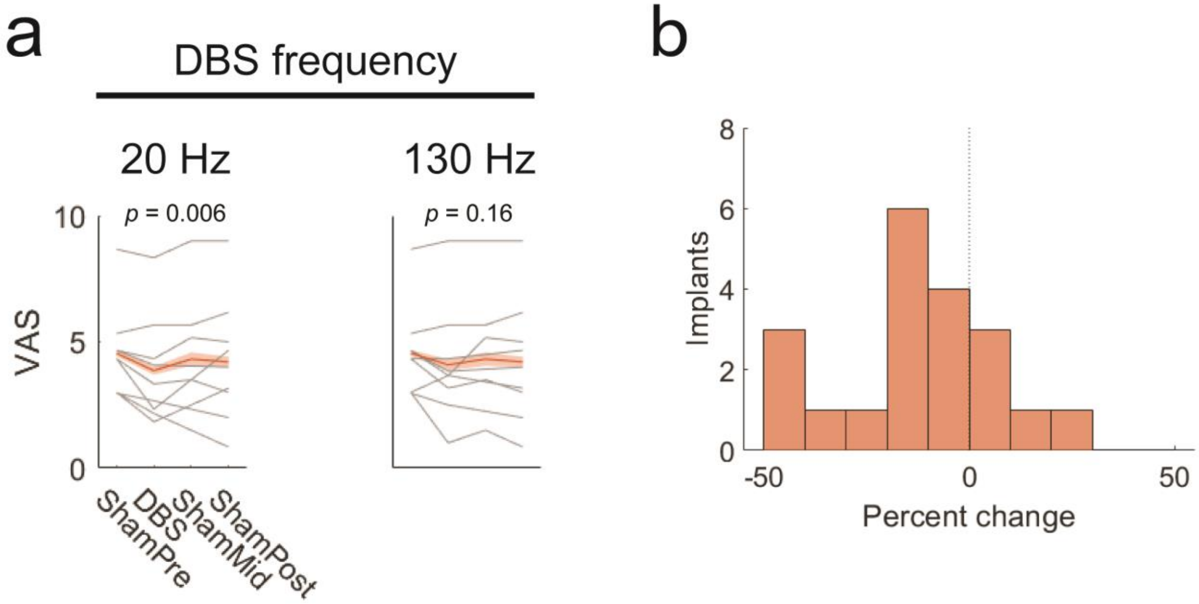

Figure 5-5 Effects of 20 and 130 Hz DBS on perception of heat pain. a. Effects of DBS on perceived pain from hot stimuli. Gray lines show mean pain scores across arm sites for each subject-implant. Red lines show average across implants with standard error of the mean shaded. *n* = 96 trials for both analyses, with sham trials shared across DBS frequencies. b. Distribution of percent change in heat pain with 20 Hz DBS. *n* = 20 implants.

Due to the small effect sizes observed and multiple comparisons made in the exploratory experiments, the effects of 20 and 130 Hz stimulation on heat pain were measured in an independent set of nine implants (five subjects) to confirm results. This group also received an additional sham trial. In this cohort, 20 Hz stimulation reduced heat pain by 0.51 points (*p*=0.006), confirming the original observation of this effect. Stimulation at 130 Hz also reduced heat pain by

0.27 points but did not reach significance (*p*=0.16). As the validation experiments did not incorporate wash-in time, results also indicate that neuromodulation of heat pain by zona incerta DBS takes rapid effect.

To quantify the effects of 20 Hz stimulation on heat pain, data from exploratory and validation experiments were combined. Analysis of each subject-implant's percent improvement from averaged sham score revealed that stimulation achieved pain reduction of 30% or more in 20% of implants. The mean and median effects of stimulation on heat pain were -11.8% and -11.3%, respectively, with a standard error of 4.5% (Figure 5B).

Discussion

This study evaluates a new form of DBS for pain and demonstrates that stimulation of zona incerta achieves a modest but significant analgesic effect in human subjects. We further demonstrate that analgesia is best achieved using stimulation at low frequency. This phenomenon was selective to perception of heat pain and did not affect perceived intensity of warm or mechanical stimuli. The results of this study are the first to confirm that stimulation of zona incerta modulates evoked pain perception in humans. This follows a compelling body of work in rodent models, which have demonstrated both behavioral manifestations and mechanistic explanations of pain modulation by excitation of zona incerta (Lucas *et al.*, 2011; Moon and Park, 2017). Human translation of zona incerta DBS is an important step to better qualify the perceptual effects of zona incerta neuromodulation and lays a foundation for further optimization of analgesic DBS.

Observation that analgesia is best achieved with stimulation at physiological frequency is a notable finding. While stimulation at conventional DBS frequencies has been hypothesized to act as an informational lesion (Grill *et al.*, 2004), stimulation at physiological firing rates may act to increase activity in zona incerta, which has been shown by rodent studies to impart analgesic effect (Moon and Park, 2017). A parsimonious interpretation of the findings is that analgesic stimulation acts by increasing GABAergic output from zona incerta to sensory thalamus. Importantly, we also show that the effects of stimulation appear specific to heat pain; perception of non-painful warm stimulation and mechanical pain thresholds were not altered by DBS. However, zona incerta is known to project widely across the brain (Mitrofanis, 2005), and potential relevant off-target effects were not investigated in this study, nor were other pain modalities.

There are differences in findings between this study and previous rodent studies. Most notably, this study did not identify any significant effects of zona incerta DBS on mechanical pain thresholds, while hind paw withdrawal thresholds were seen to increase in rodent models of neuropathic pain (Lucas *et al.*, 2011; Moon and Park, 2017; Hu *et al.*, 2019). Although unexpected, this may arise from a variety of differences between our study and those performed in rodent models. Primarily, pain in our patients did not arise from clinically relevant sources of neuropathic pain. Additionally, Parkinson disease is known to cause a broad but inconsistent and poorly understood constellation of sensory abnormalities (Ha and Jankovic, 2012), introducing an important confounder. Performing this study in humans, however, allowed for the first experiment to directly assess the effects of zona incerta stimulation on perceived pain intensities, rather than noxious withdrawal thresholds. Other human studies describing the sensory effects of nearby subthalamic stimulation differ on whether mechanical pain thresholds are modified by stimulation (Cury *et al.*, 2016; Belasen *et al.*, 2017). However, the mechanistic pathway of these effects may also be distinct from that of DBS at zona incerta (DiMarzio *et al.*, 2019).

Critically, interpretation of these results must acknowledge that targeting of zona incerta in this study is inherently imprecise. While DBS leads for Parkinson disease are placed to activate dorsolateral subthalamic nucleus, the portions of zona incerta connected to the spinothalamic tract and sensory thalamus are found in ventral zona incerta, which is located medial to the dorsolateral horn of subthalamic nucleus (Mitrofanis, 2005). As such, optimal activation of the target region could not be guaranteed. The imprecise nature of stimulation targeting may account for some of the large variations in effect size observed across subjects shown in Figures 4 and 5.

Despite this limitation in study design, stimulation of zona incerta elicited a statistically significant and reproducible effect on perceived heat pain, identifying zona incerta as a strong candidate for neuromodulation of pain. Although clinical translation of this intervention requires substantial additional work, these findings provide a compelling explanation of how subthalamic DBS modulates pain-related symptoms observed in Parkinson patients and present clear avenues for optimization. Foremost, explicit targeting of ventral zona incerta, medial to the subthalamic DBS targets employed here, has potential to markedly improve both consistency and magnitude of the analgesic effect. Our finding that stimulation at physiological frequencies is effective also motivates further investigation of other low frequency stimulation paradigms and physiologically inspired patterns. More immediately, these results can be used to inform programming for the large population of subthalamic DBS patients presenting with pain. As we advance our understanding of zona incerta, further research in this direction is warranted, particularly to examine effects on clinically relevant etiologies of pain and sustainability of effects over longer time periods.

Competing Interests

None.

Data Availability

Data from this study are available upon reasonable request to the corresponding author.

Acknowledgements

The authors would like to thank Adam Davis for his assistance in designing and constructing the thermal stimulation device. This study would not have been possible without the clinical experience and help of Kelly Lupo, Wilma Mackenzie, and Adam Matthews.

Funding

This work was supported by the A. Alfred Taubman Medical Institute, Ann Arbor, MI; the Coulter Foundation, Ann Arbor, MI; the STIM (Surgical Therapies Improving Movement) Program, Ann Arbor, MI; and the University of Michigan Medical School, Ann Arbor, MI.

Supplement

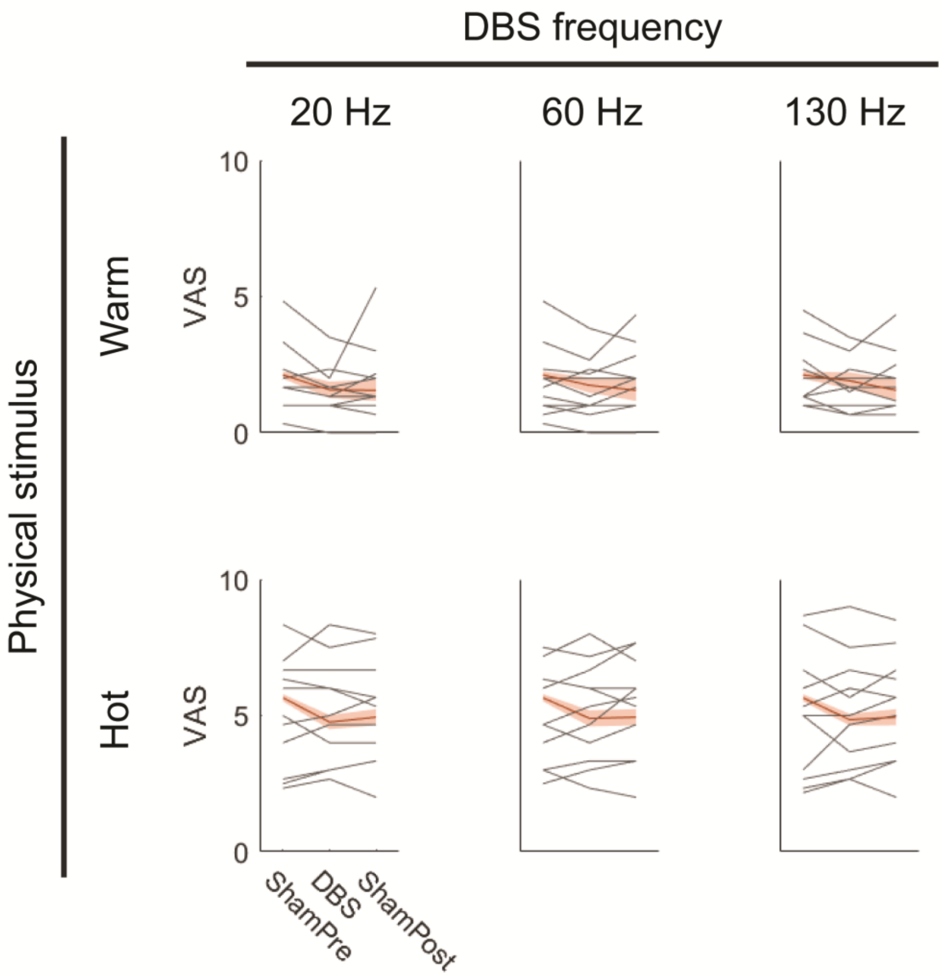

Figure 5-6 (Supplementary Figure 1) Effects of DBS on perceived intensity (rather than pain) from warm and hot stimuli. Gray lines show mean pain scores across arm sites for each subject-implant. Red lines show average across implants with standard error of the mean shaded. n = 99 trials for all plots, with sham trials shared across DBS frequencies.

Chapter 6

Emulation of Naturalistic Sensation by Unit-Specific Stimulation

Co-authored with: Matthew Willsey, Parag Patil

Abstract

Electrical stimulation of the sensory nervous system typically produces unnatural paresthesias. Attempts to emulate natural sensation have only been demonstrated with low sample sizes and often fail to replicate. In this preliminary study, we demonstrate empirically derived stimulation patterns designed from individual units' sensory-evoked firing. We show that, within a small cohort, this method of stimulation reliably replicates naturalistic sensations, while other amplitude, site, and power-matched stimulation patterns elicit paresthesia.

Introduction

Tonic pulsatile stimulation of the sensory nervous system is known to elicit unnatural sensations, often described as "electric tingling". Some approaches have been proposed to elicit more naturalistic sensation, e.g., frequency and site-specific tonic stimulation (Weiss *et al.*, 2009; Swan *et al.*, 2018), pulse-width modulation (Tan *et al.*, 2014), and biomimetic frequency modulation (George *et al.*, 2019). Previously proposed methods, however, have been demonstrated on small samples and lack evidence of wide reproducibility. In this preliminary study, we find evidence that unit-specific stimulation patterns may be able to reliably and reproducibly emulate naturalistic sensations.

Methods

Four essential tremor patients receiving deep brain stimulator lead placement surgery underwent microelectrode recording in sensory ventrocaudal nucleus of thalamus (Vc). The dorsal border of Vc was identified by elicitation of paresthesia by 130 Hz, 100 uA microstimulation. While advancing the microelectrode through Vc, an experimenter lightly and rapidly brushed sites on the patient's contralateral arm, including fingers, palmar surfaces, and distal arm. Electrophysiological activity was visually and auditorily monitored for receptive units.

Once a responsive unit is identified, approximately ten seconds of spiking activity was recorded while the receptive field received 1 Hz brushing. Electrophysiology was converted to rasters with a manually defined threshold. Tonic activity of the unit was then removed by removing a set number of spikes from the raster at a regular interval. The number of spikes and interval were manually determined through visual inspection of the original raster. The remaining spiking activity was designated as the *evoked pattern*. Clusters of bursting activity within the evoked pattern were also defined, using a manually set intra-burst inter-spike interval (ISI).

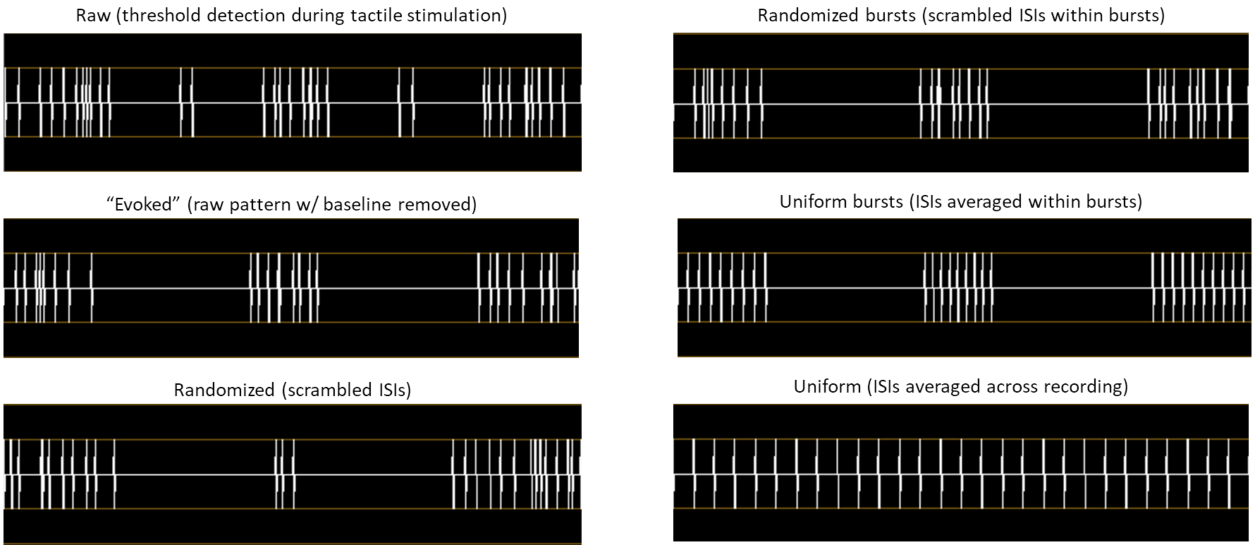

Figure 6-1 Illustrations of stimulation patterns based on a synthetic signal. Recorded threshold crossings (top left) are used to create the evoked pattern (center left) and control patterns (all others).

Using the evoked pattern, four control patterns were created: *random*, *uniform*, *uniform burst*, and *random burst*; all of which contain the same number of pulses and average pulse frequency as the evoked pattern. Random patterns are created by randomizing the ISIs of the evoked pattern. Uniform patterns are comprised of tonic pulses at the average frequency of the evoked pattern. Uniform burst patterns maintain burst groupings of the evoked pattern but average the pulse frequency within each burst. Random burst randomizes the ISIs within each burst. Patterns are demonstrated in Figure 1, with an artificial raster generated for purposes of illustration. All patterns were implemented with 60 us bipolar cathodic square waves. Stimulation amplitude for all patterns was set as the sensory threshold amplitude for tonic 100 Hz stimulation in an effort to activate the minimum volume of tissue surrounding the unit that produced the sensory evoked pattern.

Microstimulation patterns were applied in semi-random order at the site of the receptive unit, and the patient was asked to describe location and quality of sensation evoked by each pattern.

Results

Table 6-1 Stimulation patterns and evoked sensations reported by an exemplary subject.

Trial	Stimulation pattern	Reported sensation
1	Evoked	brushing at finger base
2	Random A	constant tingling at finger base
3	Random B	constant tingling at finger base
4	Uniform	constant tingling at finger base
5	Uniform burst	no sensation
6	Random burst A	no sensation
7	Random burst B	tingling at finger base and tips
8	Artificial bursts	pulsed tingling at finger base
9	Evoked	brushing at finger base

10	Tonic 27 Hz	no sensation
11	Tonic 80 Hz	no sensation

Five responsive units were identified in four subjects. Two subjects did not report paresthesia while receiving tonic 130 Hz stimulation at 100 uA and were subsequently excluded from further stimulation. Stimulation testing occurred in a total of three sites across two patients. The stimulation order and reported sensations at one exemplar site are shown in Table 1.

Aggregate data across all subjects and sites show that stimulation with the evoked pattern elicited only sensations that were described as naturalistic and similar to the tactile stimulus that evoked the recorded unit activity. Conversely, all other stimulation patterns evoked only paresthetic sensations.

Table 6-2 Stimulation patterns and evoked sensations across all subjects and sites.

Stimulation pattern	Trials (sites)	Reported sensations
Evoked	5 (3)	3/5 tactile sensation 2/5 no sensation
Random	4 (2)	4/4 tingling
Random burst	4 (2)	1/4 tingling 3/4 no sensation
Uniform burst	1 (1)	1/1 no sensation
Uniform	3 (2)	3/3 tingling
Tonic (27, 80, 130 Hz)	3 (2)	1/3 tingling 2/3 no sensation

Discussion

This preliminary study demonstrated that suprathreshold stimulation with sensory evoked patterns reliably elicits naturalistic sensation while other power-matched modes of stimulation elicit paresthesia only. These findings provide support for two hypotheses. First, the observation that stimulation with evoked patterns was necessary and sufficient to elicit naturalistic sensation indicates that temporally precise firing patterns are necessary to encode sensation in sensory thalamus. Second, the detailed sensations described by subjects indicate that activation of a highly localized volumes in sensory thalamus is sufficient to evoke specific naturalistic sensations.

Our results support previous observations that biomimetic stimulation patterns are better able to elicit naturalistic percepts (Tan *et al.*, 2014; Swan *et al.*, 2018; George *et al.*, 2019) than tonic stimulation. The high reliability of evoked pattern stimulation as shown in this study, however, suggests that naturalistic activation patterns may be specific to individual units or populations within sensory thalamus. In a notable departure from previously reported findings, we did not observe any naturalistic percepts resulting from tonic stimulation. This may be a result of small sample size.

Future experiments will attempt to validate this preliminary data over a larger dataset. With additional data, it may also be possible to identify generalizable patterns that can be used to generate naturalistic activation patterns without the need for unit-specific design of stimulation pattern.

Chapter 7

Temporal Dynamics of Tactile Sensation Representation in Sensory Cortex

Co-authored with: Samuel Nason, Philip Vu, Parag Patil, Cynthia Chestek

Abstract

Attempts to reliably emulate naturalistic sensations via electrical stimulation of the nervous system have remained elusive, possibly due to hypersynchrony of artificially activated pathways. In this preliminary study, we investigated the temporal dynamics of cortical units firing in response to tactile stimulation of the hand. We find that while units exhibit macro-scale synchrony at the level of seconds, temporal dynamics are more complex at the level of milliseconds, providing a potential explanation of why artificial stimulation tends to elicit non-natural sensations.

Introduction

Tactile sensation is a critical component of intuitive prosthetic control. A rough approximation of haptic feedback can be provided via tonic pulsatile stimulation of the nervous system, eliciting parasthetic sensations often described as “electric tingling”. Methods to reliably emulate naturalistic percepts via artificial stimulation, however, have yet to be reported despite numerous efforts (Weiss *et al.*, 2009; Tan *et al.*, 2014; Lee *et al.*, 2018; Swan *et al.*, 2018; George *et al.*, 2019; Kirin *et al.*, 2019). The authors hypothesize that this may be due to hypersynchrony of units activated by artificial stimulation. Electrical stimulation simultaneously and indiscriminately activates large populations of cells, while natural tactile stimulation is known to elicit complex and meaningful temporal dynamics across sensory units (Fortier-Poisson and Smith, 2016).

In this preliminary study, we investigated the temporal dynamics of cortical units firing in response to tactile stimulation of the hand with specific focus on inter-unit synchrony. We find that while units exhibit macro-scale synchrony at the level of seconds, units are largely unsynchronized at the level of milliseconds, providing a potential explanation of why artificial stimulation tends to elicit non-natural sensations.

Methods

A rhesus macaque monkey was implanted with two 96-channel Utah arrays: one in right motor cortex and the other in right sensory cortex. Several units were visually observed to respond to brushing of the medial edge of the left small finger.

A battery of tactile stimuli was applied to the receptive field described above: 1 Hz brushing by hand, 1 Hz poking with a wooden probe, 30 Hz vibration, 60 Hz vibration, 170 Hz vibration, and constant pressure. Electrical stimulation of the ulnar nerve was also applied through fine wires inserted into the medial aspect of the forearm near the wrist. Electrical stimuli included 30 Hz, 60 Hz, and 170 Hz pulses. Patterns also included pulse-width modulation (Tan *et al.*, 2014) and biomimetic pulse trains (George *et al.*, 2019) previously describe in literature. All stimulation patterns were applied at 50, 100, 200, 300, and 400 uA in order of increasing amplitude.

Stimulation patterns were also tested in a human regenerative peripheral nerve interface to determine the sensation produced by each pattern. Stimulation was delivered at sensory threshold to a nerve interface that elicits sensation at the medial edge of the little finger, mirroring the receptive field of the monkey’s recorded units. The subject was asked to describe the sensation elicited by each pattern.

Analysis of channel spiking activity used threshold crossings only, without spike sorting, as threshold crossings were observed to be highly modulated by tactile stimuli. Prior to threshold detection, channels were common average referenced and high pass filtered at 300 Hz. During trials for which ulnar nerve stimulation was performed, stimulation artifact was removed using a trial and channel-specific template of the artifact, created by averaging the recorded signal over each stimulus pulse (recorded on an independent channel).

Results

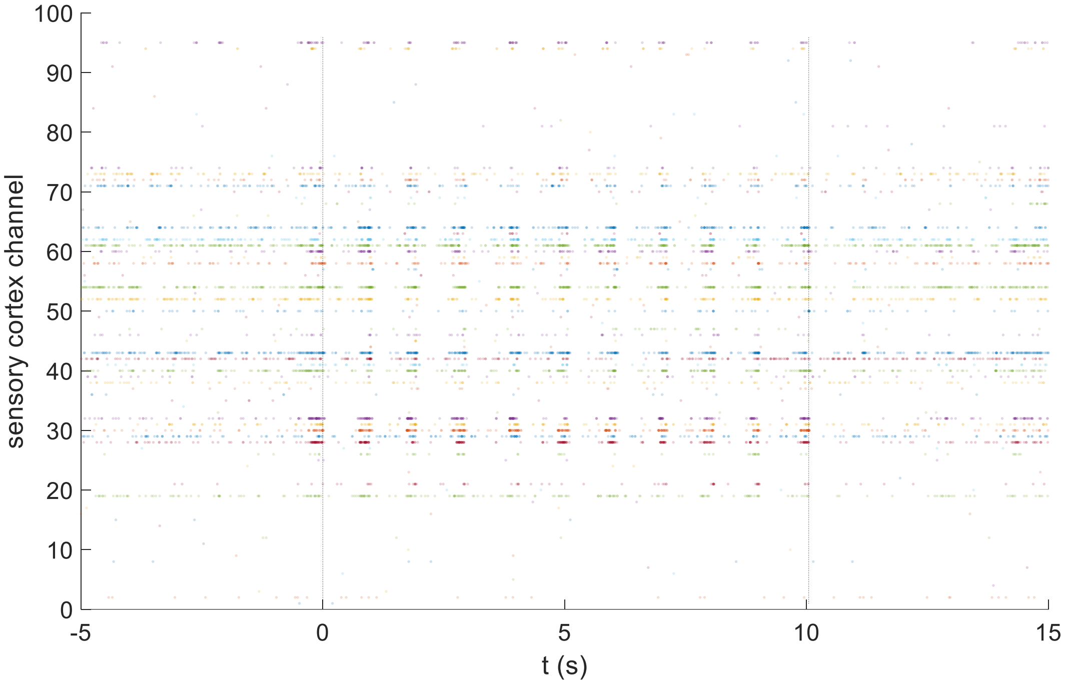

Figure 7-1: Sensory cortex threshold crossings across all channels during 1 Hz brushing. Brushing occurred roughly between the times points of 0 and 10 seconds.

Tactile stimulation of the medial aspect of the little finger resulted in highly distinguishable stimulus-locked threshold crossings in a subset of recorded channels. Figure 1 shows rasters of threshold crossings across all 96 channels on sensory cortex in response to a tactile stimulus. Four channels (28, 30, 32, and 54) were identified to reliably and robustly responsive to all six tactile stimuli and were used for subsequent analysis of cross-channel synchrony. A smaller subset of channels in motor cortex were also found to respond to tactile stimuli.

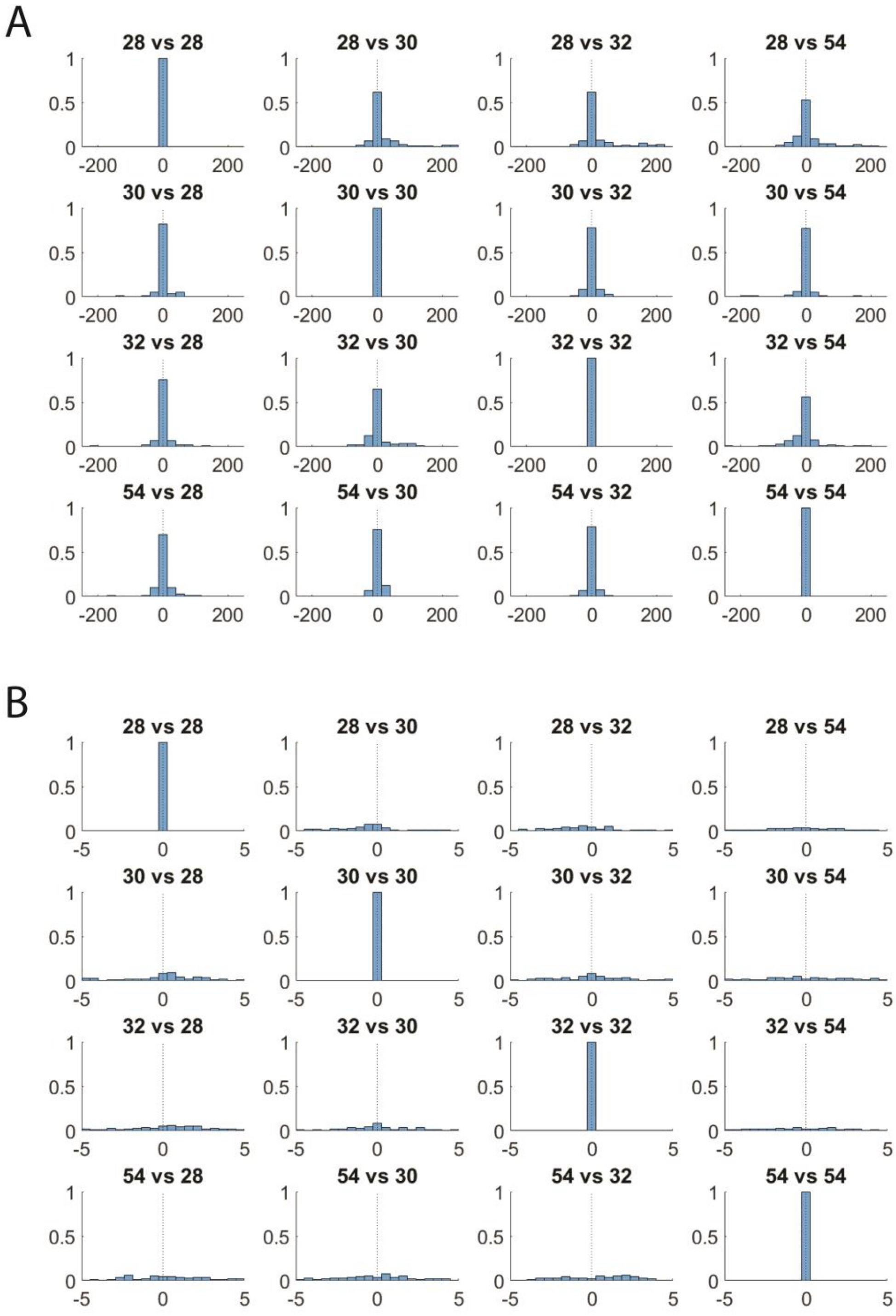

Figure 7-2: Cross-channel synchrony of tactile-induced spiking. Percentage of spikes on one channel occurring within a given time period of another channel's spike, from same trial shown in Figure 1. A) Synchrony over a 250 ms window. B) Synchrony over a 5 ms window.

At large time scales (hundreds of milliseconds), responsive channels were found to be highly synchronous (Figure 2A) during 1 Hz brushing. This was expected, as all channels were responding to the same tactile inputs. However, at single millisecond timescales, we find that threshold crossings across channels are highly asynchronous (Figure 2B). This relationship was found across all tactile stimuli.

Stimulation of the ulnar peripheral nerve interface in the human subject elicited paresthetic "electric tingling" sensations with all patterns. Electrical stimulation of ulnar nerve in the primate subject produced artifact templates that did not contain obvious units (Figure 3). However, electrical stimulation was not found to modulate recorded threshold crossings in sensory or motor cortex. Threshold crossings elicited during ulnar nerve stimulation were not used for further analysis.

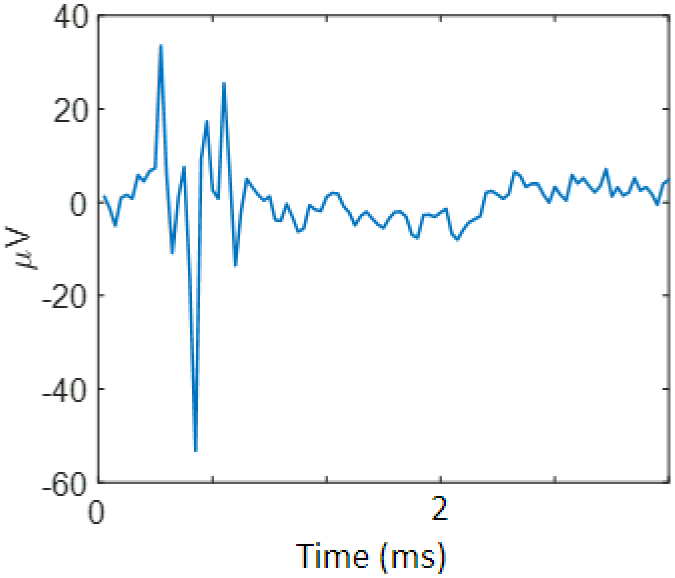

Figure 7-3: Representative stimulation artifact template. Extracted from channel 28 with 400 uA stimulation. No action potential-like waveforms are observed within the artifact template.

Discussion

This set of experiments presents insight into the temporal dynamics of evoked sensory activity across units during natural tactile stimulation. The authors hypothesize that natural tactile sensations elicit neural activity with complex timing characteristics, while paresthetic sensations evoked by electrical stimulation arise from artificially time-locked activity of simultaneously activated fibers. The findings here indicate that natural activation of sensory pathways does indeed result in non-time-locked activity across cortical channels. However, the study was unable to confirm that electrical stimulation results in different neural activity.

The lack of measurable evoked activity in sensory and motor cortex from ulnar nerve stimulation significantly limited the scope of the current study. Although the authors observed clear behavioral responses to electrical stimulation, indicating successful delivery of suprathreshold stimulation, there are multiple potential causes for this result. First, it is probable that insertion of the fine wire electrodes missed ulnar nerve and were inserted instead in an adjacent space. Second, it is possible that stimulation, even within ulnar nerve, elicited sensory activity at cortical sites not covered by the implanted electrode arrays. Third, it is possible that template subtraction of the stimulation artifact also removed evoked activity, although this was unlikely as templates exhibited smaller magnitudes than the observed spikes.

Follow-up experiments will apply stimulation directly to the receptive field of the finger edge to preclude concerns of stimulation targeting. Stimulation will also be applied at reverse polarity, so that evoked potentials can be identified, even with template subtraction of stimulation artifacts. With a more robust stimulation protocol, new data may definitively demonstrate differences in spiking dynamics resulting from artificial and natural sensation. Such results would provide a mechanistic explanation of perceptual differences elicited by tactile and electrical stimulation and inform future design of more efficacious sensory stimulation paradigms.

Chapter 8

Placing the Work in Context

The work described here spans the breadth of developmental stages along the translational arc of biomedical research. Earlier chapters presented tools that are close to clinical validation and implementation, while later chapters explored basic science questions. Together, these chapters form a collection of contributions to the field of neural engineering with foreseeable impacts, both imminent and long-term. However, each study leaves significant room for further refinement, presenting opportunities for follow-up studies.

Innovations in deep brain stimulation

In the near term, the lead localization and stimulation optimization technologies presented in Chapters 2 and 4 may have the greatest practical impact. Chapter 2 combined sophisticated computational models of tissue activation with deep brain electrophysiology and machine learning tools to identify and validate neural signal markers of therapeutic stimulation regions. Chapter 4 utilized modern imaging technologies and computational power to interpret physical properties of the brain, prototyping an accessible tool for localization of deep brain leads. While both studies produced ancillary findings to further fuel basic science research, their most significant contributions arise from the unification and translation of previously disparate works into clinically useful tools.

The potential clinical impact of more sophisticated targeting technologies is large. The recent introduction of directional leads to the DBS market (Contarino *et al.*, 2014; Pollo *et al.*, 2014; Dembek *et al.*, 2017) have increased the possible precision of delivered stimulation. The capabilities afforded by these technologies, however, present a new challenge. Additional stimulation parameters dramatically increase the possible space of stimulation programs, thereby increasing the burden of stimulation programming which is already time-consuming and expensive (Hunka *et al.*, 2005; Volkmann *et al.*, 2006). Improved targeting technologies can help to both preemptively identify promising regions of stimulation, enabling use of automated stimulation programming algorithms (McIntyre *et al.*, 2006; Teplitzky *et al.*, 2016; Xiao *et al.*, 2016; Pena *et al.*, 2017; Anderson *et al.*, 2018), and also further inform our understanding of where and how therapeutic stimulation acts upon pathological activity. Critically, prediction of entire tissue activation regions, rather than discrete points, makes it possible to predict both optimal stimulation site and voltage. Although the technologies described here are not intrinsically sophisticated, maximization of patient impact requires distribution to a broad market of neurosurgeons. To this end, collaboration from industry partners for commercialization is necessary.

Additional work to further refine the targeting technologies presented here is ongoing. While Chapter 2 treated satisfactory therapeutic effect as a given from clinical testing, outcomes from DBS are complex and multidimensional (Chou *et al.*, 2013), warranting attention toward specific motor outcomes, as well as side effects, reductions in medication, and other effects, such as changes in sensation (Cury *et al.*, 2016). The manifestations of these effects vary by patient and present an opportunity for improvement of therapeutic tissue activation prediction. Previous studies have shown that relationships between specific motor outcomes, recorded electrophysiology, and stimulation site do exist (Moran *et al.*, 2008; Oswal *et al.*, 2013a; Bour *et al.*, 2015; Kuhn and Volkmann, 2017; Telkes *et al.*, 2018), establishing promising leads with which to pursue further optimization. This approach may also be augmented with use of more sophisticated interpretations of multi-band interaction, such as phase-amplitude coupling (van Wijk *et al.*, 2016; Shreve *et al.*, 2017) and beta burst length (Tinkhauser *et al.*, 2017). Our research group is now performing a prospective evaluation of the tool, demonstrating its utility on a separate platform, and investigating the potential of motor outcome-specific predictions.

Likewise, clear paths of optimization exist for impedance-guided lead localization. Although Chapter 4 established a novel method of efficiently creating whole-brain impedance atlases, it also identified spatial precision as the major limiting factor for using impedance to provide spatial information. The simplest approach to addressing this issue is to employ a smaller test electrode (Newman, 1966). Smaller electrodes with lower surface areas present additional challenges, however. First, they exhibit intrinsically higher impedance, elevating the baseline signal. Second, smaller surface areas can tolerate smaller charge delivery, before exhibiting irreversible non-faradaic reactions. The microelectrode recording tip is an obvious candidate for this modification, although safety tests must first be done to assess safety. The use of multiple contacts to act as both current source and return may also prove to provide more precise spatial information. Creation of a whole-brain impedance atlas for such a method, however, will be much more complex, as expected values may differ significantly with respect to electrode orientation.

Stimulation of zona incerta for pain neuromodulation, presented in Chapter 5, is situated further upstream along the path to clinical application. The chapter demonstrated, in humans, an analgesic intervention previously shown only in rodent models (Lucas *et al.*, 2011). While the demonstrated effect size fails to meet the clinical criteria to justify a new treatment modality for pain management (Coffey, 2001), the study provides a mechanistic explanation for pain relief resulting from subthalamic DBS (Oshima *et al.*, 2012; Surucu *et al.*, 2013; Jung *et al.*, 2015; Belasen *et al.*, 2017; Custozzo *et al.*, 2020). This discovery will inform more clinically focused investigations in the future, specifically by enabling clinicians to explicitly treat pain, a well-established but often neglected symptom of Parkinson disease (Ha and Jankovic, 2012; Rana *et al.*, 2013), in recipients of subthalamic DBS. Moving forward, these marginal advancements may eventually elucidate a new intervention to directly target other etiologies of chronic pain.

Notably, the analgesic effects observed in the chapter were achieved with coincidentally placed leads. Acknowledging the importance of spatially precise stimulation, it is serendipitous that any effect was observed at all. Indeed, large variance in effect size was observed across individuals. Although the optimal site of zona incerta stimulation in humans is yet to be established, more intentional targeting of the structure and its subdomains is a promising avenue by which to improve analgesic effect (Mitrofanis, 2005). The study described here also leaves room for evaluation of other forms of pain, such as cold and mechanical pain, and their modulation by zona incerta stimulation.

Advances in sensory modulation

The latter chapters on tactile sensory modulation, in contrast, are situated soundly within the space of exploratory research, with the goal of better understanding mechanisms by which naturalistic tactile sensation is achieved. Chapter 6 showed compelling evidence that unit-specific stimulation patterns modeled after the unit's own evoked activity in sensory thalamus can replicate tactile sensations. Chapter 7 demonstrated that natural tactile stimulation manifests as unsynchronized activity across units in sensory cortex.

It is critical to acknowledge here that there have been previous reports of achieving naturalistic tactile sensations with electrical stimulation (Tan *et al.*, 2014; Lee *et al.*, 2018; Swan *et al.*, 2018; George *et al.*, 2019). However, published methods have been tested only in small samples and often fail to replicate in follow-up studies. These qualifications highlight the importance of acquiring additional data to verify the stated claims in both studies described here.

Nonetheless, given the available data, the studies reveal important insights on timing dynamics of both individual firing and population activity during naturalistic sensation. Interestingly, the two chapters appear to support intuitively contradictory conclusions. While Chapter 6 claims that precise modulation of a small volume around a single unit can produce specific tactile sensations, Chapter 7 suggests that meaningful tactile information is represented across multiple units in a temporally complex manner. These observations may be reconciled by the fact that they are observed at different locations along the sensory pathway or by another mechanism of sensory integration, although these possibilities cannot be verified with our data.

Conversely, both studies reinforce the notion that naturalistic sensation is best achieved with highly precise activation of specific. This is concordant with previous observations that microstimulation of sensory thalamus more reliably elicits “natural” sensations than stimulation delivered via the macro contact (Swan *et al.*, 2018). Other attempts at achieving naturalistic sensation have employed less discriminatory stimulation paradigms (Tan *et al.*, 2014; Lee *et al.*, 2018; George *et al.*, 2019; Kirin *et al.*, 2019), potentially explaining the prevalence of parasthetic sensations.

In line with published studies on naturalistic stimulation, the sensory experiments in this dissertation approach sensory modulation from an engineering perspective. Although informed by basic neuroscience, these studies largely seek to validate plausible patterns with which to induce naturalistic sensation. Additional basic neuroscience research examining low-level interactions along the full sensory pathway will help to better inform and generalize the approaches discussed here and elsewhere. Recent rodent studies, in particular, have provided particularly relevant information, elucidating fundamental processes, such as interactions between sensory thalamic and cortical activity (Borden *et al.*, 2019), the effects of adaptation (Wright *et al.*, 2019), and the influence of cognitive states (Sederberg *et al.*, 2019).

Human studies, however, produce crucial qualitative findings concerning the specific nature of induced sensations. To this end, the studies described here will contribute important knowledge to further inform design of naturalistic stimulation. Chapter 6 and follow-up experiments will determine the importance and specificity of specific timing properties in activation patterns. Future experiments may also ask whether patterns are unique across units (Can evoked patterns recorded from one unit be used to evoke naturalistic sensations at another site?) and explore the extent of pathways activated during stimulation-evoked naturalistic sensation (How many cells are or can be activated to produce natural sensations?). Likewise, the findings from Chapter 7 and ensuing experiments may help to constrain future design of naturalistic stimulation paradigms, by establishing an upper limit to the span of pathways that can be activated before producing paresthesia.

Altogether, the works described here help to realize the clinical potential of previously existing technologies and reveal promising new avenues along which to further advance neuroprosthetic technology. With additional work, it is foreseeable that sensorimotor neuromodulation will achieve the precision and accuracy necessary to find utility in a wide range of clinical applications, from sensory prostheses to treatment of pain disorders.

References

Akram H, Sotiropoulos SN, Jbabdi S, Georgiev D, Mahlknecht P, Hyam J, *et al.* Subthalamic deep brain stimulation sweet spots and hyperdirect cortical connectivity in Parkinson's disease. Neuroimage 2017; 158: 332-45.

Anderson DN, Osting B, Vorwerk J, Dorval AD, Butson CR. Optimized programming algorithm for cylindrical and directional deep brain stimulation electrodes. J Neural Eng 2018; 15(2): 026005.

Andrews RJ, Li J, Kuhn SA, Walter J, Reichart R. Impedance Recording in Central Nervous System Surgery. Textbook of Stereotactic and Functional Neurosurgery; 2009. p. 631-44.

Astrom M, Diczfalusy E, Martens H, Wardell K. Relationship between neural activation and electric field distribution during deep brain stimulation. IEEE Trans Biomed Eng 2015; 62(2): 664-72.

Balachandran R, Mitchell JE, Dawant BM, Fitzpatrick JM. Accuracy evaluation of microTargeting Platforms for deep-brain stimulation using virtual targets. IEEE Trans Biomed Eng 2009; 56(1): 37-44.

Barthó P, Freund TF, Acsády L. Selective GABAergic innervation of thalamic nuclei from zona incerta. European Journal of Neuroscience 2002; 16(6): 999-1014.

Belasen A, Rizvi K, Gee LE, Yeung P, Prusik J, Ramirez-Zamora A, *et al.* Effect of low-frequency deep brain stimulation on sensory thresholds in Parkinson's disease. J Neurosurg 2017; 126(2): 397-403.

Bjartmarz H, Rehncrona S. Comparison of accuracy and precision between frame-based and frameless stereotactic navigation for deep brain stimulation electrode implantation. Stereotact Funct Neurosurg 2007; 85(5): 235-42.

Boccard SG, Pereira EA, Moir L, Aziz TZ, Green AL. Long-term outcomes of deep brain stimulation for neuropathic pain. Neurosurgery 2013; 72(2): 221-30; discussion 31.

Borden P, Wright N, Sederberg A, Waiblinger C, Haider B, Stanley GB. Thalamic modulation and the shaping of cortical sensory representations in the awake and anesthetized mouse. 2019; Chicago, IL: Society for Neuroscience; 2019.

Bour LJ, Lourens MA, Verhagen R, de Bie RM, van den Munckhof P, Schuurman PR, *et al.* Directional Recording of Subthalamic Spectral Power Densities in Parkinson's Disease and the Effect of Steering Deep Brain Stimulation. Brain Stimul 2015; 8(4): 730-41.

Bressan M, Vitria JJItopa, intelligence m. On the selection and classification of independent features. 2003; 25(10): 1312-7.

Brocker DT, Swan BD, So RQ, Turner DA, Gross RE, Grill WM. Optimized temporal pattern of brain stimulation designed by computational evolution. Sci Transl Med 2017; 9(371).

Bullard DE, Makachinas TT. Measurement of tissue impedence in conjunction with computed tomography-guided stereotaxic biopsies. J Neurol Neurosurg Psychiatry 1987; 50(1): 43-51.

Burchiel KJ, McCartney S, Lee A, Raslan AM. Accuracy of deep brain stimulation electrode placement using intraoperative computed tomography without microelectrode recording. J Neurosurg 2013; 119(2): 301-6.

Butson CR, Cooper SE, Henderson JM, McIntyre CC. Patient-specific analysis of the volume of tissue activated during deep brain stimulation. NeuroImage 2007; 34(2): 661-70.

Butson CR, Cooper SE, Henderson JM, Wolgamuth B, McIntyre CC. Probabilistic analysis of activation volumes generated during deep brain stimulation. Neuroimage 2011; 54(3): 2096-104.

Cagnan H, Denison T, McIntyre C, Brown P. Emerging technologies for improved deep brain stimulation. Nat Biotechnol 2019; 37(9): 1024-33.

Caire F, Ranoux D, Guehl D, Burbaud P, Cuny E. A systematic review of studies on anatomical position of electrode contacts used for chronic subthalamic stimulation in Parkinson's disease. Acta Neurochir (Wien) 2013; 155(9): 1647-54; discussion 54.

Chen L, Li N, Ge S, Lozano AM, Lee DJ, Yang C, *et al.* Long-term results after deep brain stimulation of nucleus accumbens and the anterior limb of the internal capsule for preventing heroin relapse: An open-label pilot study. Brain Stimul 2019; 12(1): 175-83.

Chestek CA, Gilja V, Blabe CH, Foster BL, Shenoy KV, Parvizi J, *et al.* Hand posture classification using electrocorticography signals in the gamma band over human sensorimotor brain areas. Journal of neural engineering 2013; 10(2): 026002.

Cho D, Min B, Kim J, Lee B. EEG-based Prediction of Epileptic Seizures Using Phase Synchronization Elicited from Noise-Assisted Multivariate Empirical Mode Decomposition. IEEE Transactions on Neural Systems and Rehabilitation Engineering 2017; 25(8): 1309-18.

Chou KL, Taylor JL, related disorders P-PG. The MDS− UPDRS tracks motor and non-motor improvement due to subthalamic nucleus deep brain stimulation in Parkinson disease. Parkinsonism & related disorders 2013.

Coffey RJ. Deep brain stimulation for chronic pain: results of two multicenter trials and a structured review. Pain Med 2001; 2(3): 183-92.

Cohen MX. Analyzing neural time series data: theory and practice: MIT press; 2014.

Cole SR, van der Meij R, Peterson EJ, de Hemptinne C, Starr PA, Voytek B. Nonsinusoidal beta oscillations reflect cortical pathophysiology in Parkinson's disease. Journal of Neuroscience 2017; 37(18): 4830-40.

Cole SR, Voytek B. Brain Oscillations and the Importance of Waveform Shape. Trends in Cognitive Sciences 2017; 21(2): 137-49.

Cole SR, Voytek B. Cycle-by-cycle analysis of neural oscillations. bioRxiv 2018: 302000.

Combrisson E, Jerbi K. Exceeding chance level by chance: The caveat of theoretical chance levels in brain signal classification and statistical assessment of decoding accuracy. Journal of neuroscience methods 2015; 250: 126-36.

Contarino MF, Bour LJ, Verhagen R, Lourens MA, de Bie RM, van den Munckhof P, *et al.* Directional steering: A novel approach to deep brain stimulation. Neurology 2014; 83(13): 1163-9.

Cortes C, Vapnik V. Support-vector networks. Machine Learning 1995; 20(3): 273-97.

Cury RG, Galhardoni R, Teixeira MJ, Dos Santos Ghilardi MG, Silva V, Myczkowski ML, *et al.* Subthalamic deep brain stimulation modulates conscious perception of sensory function in Parkinson's disease. Pain 2016; 157(12): 2758-65.

Custozzo A, DiMarzio M, Pilitsis JG. Addressing Parkinson Disease-Related Pain with Deep Brain Stimulation. World Neurosurg 2020; 135: 381-2.

D'Haese PF, Pallavaram S, Konrad PE, Neimat J, Fitzpatrick JM, Dawant BM. Clinical accuracy of a customized stereotactic platform for deep brain stimulation after accounting for brain shift. Stereotact Funct Neurosurg 2010; 88(2): 81-7.

De Hemptinne C, Ryapolova-Webb ES, Air EL, Garcia PA, Miller KJ, Ojemann JG, *et al.* Exaggerated phase–amplitude coupling in the primary motor cortex in Parkinson disease. Proceedings of the National Academy of Sciences 2013; 110(12): 4780-5.

Dembek TA, Reker P, Visser-Vandewalle V, Wirths J, Treuer H, Klehr M, *et al.* Directional DBS increases side-effect thresholds-A prospective, double-blind trial. Mov Disord 2017; 32(10): 1380-8.

DiMarzio M, Rashid T, Hancu I, Fiveland E, Prusik J, Gillogly M, *et al.* Functional MRI Signature of Chronic Pain Relief From Deep Brain Stimulation in Parkinson Disease Patients. Neurosurgery 2019; 85(6): E1043-E9.

Duda RO, Hart PE, Stork DG. Pattern classification: John Wiley & Sons; 2012.

Flandrin P, Rilling G, Goncalves P. Empirical mode decomposition as a filter bank. IEEE signal processing letters 2004; 11(2): 112-4.

Foffani G, Priori A, Egidi M, Rampini P, Tamma F, Caputo E, *et al.* 300-Hz subthalamic oscillations in Parkinson's disease. Brain 2003; 126(Pt 10): 2153-63.

Fortier-Poisson P, Smith AM. Neuronal activity in somatosensory cortex related to tactile exploration. J Neurophysiol 2016; 115(1): 112-26.

Frequin HL, Bot M, Dilai J, Scholten MN, Postma M, Bour LJ, *et al.* Relative Contribution of Magnetic Resonance Imaging, Microelectrode Recordings, and Awake Test Stimulation in Final Lead Placement during Deep Brain Stimulation Surgery of the Subthalamic Nucleus in Parkinson's Disease. Stereotact Funct Neurosurg 2020; 98(2): 118-28.

Frizon LA, Yamamoto EA, Nagel SJ, Simonson MT, Hogue O, Machado AG. Deep Brain Stimulation for Pain in the Modern Era: A Systematic Review. Neurosurgery 2020; 86(2): 191-202.

Fry WJ, Fry FJ, Leichner GH, Heimburger RF. Tissue interface detector for ventriculography and other applications. J Neurosurg 1962; 19: 793-8.

Garcia-Garcia D, Guridi J, Toledo JB, Alegre M, Obeso JA, Rodriguez-Oroz MC. Stimulation sites in the subthalamic nucleus and clinical improvement in Parkinson's disease: a new approach for active contact localization. J Neurosurg 2016; 125(5): 1068-79.

George JA, Kluger DT, Davis TS, Wendelken SM, Okorokova EV, He Q, *et al.* Biomimetic sensory feedback through peripheral nerve stimulation improves dexterous use of a bionic hand. Science Robotics 2019; 4(32).

Gradinaru V, Mogri M, Thompson KR, Henderson JM, Deisseroth K. Optical deconstruction of parkinsonian neural circuitry. Science 2009; 324(5925): 354-9.

Grill WM, Snyder AN, Miocinovic S. Deep brain stimulation creates an informational lesion of the stimulated nucleus. Neuroreport 2004; 15(7): 1137-40.

Gunalan K, Chaturvedi A, Howell B, Duchin Y, Lempka SF, Patriat R, *et al.* Creating and parameterizing patient-specific deep brain stimulation pathway-activation models using the hyperdirect pathway as an example. PLoS One 2017; 12(4): e0176132.

Gunalan K, Howell B, McIntyre CC. Quantifying axonal responses in patient-specific models of subthalamic deep brain stimulation. Neuroimage 2018; 172: 263-77.

Guo S, Zhuang P, Hallett M, Zheng Z, Zhang Y, Li J, *et al.* Subthalamic deep brain stimulation for Parkinson's disease: correlation between locations of oscillatory activity and optimal site of stimulation. Parkinsonism Relat Disord 2013; 19(1): 109-14.

Ha AD, Jankovic J. Pain in Parkinson's disease. Movement Disorders 2012; 27(4): 485-91.

Hamel W, Koppen JA, Alesch F, Antonini A, Barcia JA, Bergman H, *et al.* Targeting of the Subthalamic Nucleus for Deep Brain Stimulation: A Survey Among Parkinson Disease Specialists. World Neurosurg 2017; 99: 41-6.

Haynes WI, Haber SN. The organization of prefrontal-subthalamic inputs in primates provides an anatomical substrate for both functional specificity and integration: implications for Basal Ganglia models and deep brain stimulation. J Neurosci 2013; 33(11): 4804-14.

Hazrati MH, Ulrich. Decoding finger movements from ECoG signals using Empirical Mode Decomposition. Biomed Tech 2012; 57.

Herrington TM, Cheng JJ, Eskandar EN. Mechanisms of deep brain stimulation. J Neurophysiol 2016; 115(1): 19-38.

Herrman H, Egge A, Konglund AE, Ramm-Pettersen J, Dietrichs E, Tauboll E. Anterior thalamic deep brain stimulation in refractory epilepsy: A randomized, double-blinded study. Acta Neurol Scand 2019; 139(3): 294-304.

Hirschmann J, Abbasi O, Storzer L, Butz M, Hartmann CJ, Wojtecki L, *et al.* Longitudinal Recordings Reveal Transient Increase of Alpha/Low-Beta Power in the Subthalamic Nucleus Associated With the Onset of Parkinsonian Rest Tremor. Front Neurol 2019; 10: 145.

Holloway KL, Gaede SE, Starr PA, Rosenow JM, Ramakrishnan V, Henderson JM. Frameless stereotaxy using bone fiducial markers for deep brain stimulation. J Neurosurg 2005; 103(3): 404-13.

Horn A, Neumann WJ, Degen K, Schneider GH, Kuhn AA. Toward an electrophysiological "sweet spot" for deep brain stimulation in the subthalamic nucleus. Hum Brain Mapp 2017; 38(7): 3377-90.

Houshmand L, Cummings KS, Chou KL, Patil PG. Evaluating indirect subthalamic nucleus targeting with validated 3-tesla magnetic resonance imaging. Stereotact Funct Neurosurg 2014; 92(6): 337-45.

Houshmand L, Malaga KA, Chaturvedi A, Chou KL, MyIntyre CC, Patil PG. Individualized, atlas-independent diffusion tensor imaging-based thalamic segmentation and tissue activation modeling in deep brain stimulation for essential tremor Neuroimage Clinical In review.

Howell B, McIntyre CC. Analyzing the tradeoff between electrical complexity and accuracy in patient-specific computational models of deep brain stimulation. J Neural Eng 2016; 13(3): 036023.

Howell B, McIntyre CC. Role of Soft-Tissue Heterogeneity in Computational Models of Deep Brain Stimulation. Brain Stimul 2017; 10(1): 46-50.

Hu TT, Wang RR, Du Y, Guo F, Wu YX, Wang Y, *et al.* Activation of the Intrinsic Pain Inhibitory Circuit from the Midcingulate Cg2 to Zona Incerta Alleviates Neuropathic Pain. J Neurosci 2019; 39(46): 9130-44.

Huang J-R, Fan S-Z, Abbod M, Jen K-K, Wu J-F, Shieh J-S. Application of Multivariate Empirical Mode Decomposition and Sample Entropy in EEG Signals via Artificial Neural Networks for Interpreting Depth of Anesthesia. Entropy 2013; 15(9).

Huang NE, Shen Z, Long SR, Wu MC, Shih HH, Zheng Q, *et al.* The empirical mode decomposition and the Hilbert spectrum for nonlinear and non-stationary time series analysis. Proceedings of the Royal Society of London A: mathematical, physical and engineering sciences; 1998: The Royal Society; 1998. p. 903-95.

Hunka K, Suchowersky O, Wood S, Derwent L, Kiss ZH. Nursing time to program and assess deep brain stimulators in movement disorder patients. J Neurosci Nurs 2005; 37(4): 204-10.

Hunsche S, Sauner D, Maarouf M, Poggenborg J, Lackner K, Sturm V, *et al.* Intraoperative X-ray detection and MRI-based quantification of brain shift effects subsequent to implantation of the first electrode in bilateral implantation of deep brain stimulation electrodes. Stereotact Funct Neurosurg 2009; 87(5): 322-9.

Huys D, Kohl S, Baldermann JC, Timmermann L, Sturm V, Visser-Vandewalle V, *et al.* Open-label trial of anterior limb of internal capsule-nucleus accumbens deep brain stimulation for obsessive-compulsive disorder: insights gained. J Neurol Neurosurg Psychiatry 2019; 90(7): 805-12.

Ince NF, Gupte A, Wichmann T, Ashe J, Henry T, Bebler M, *et al.* Selection of optimal programming contacts based on local field potential recordings from subthalamic nucleus in patients with Parkinson's disease. Neurosurgery 2010; 67(2): 390-7.

Irwin ZT, Thompson DE, Schroeder KE, Tat DM, Hassani A, Bullard AJ, *et al.* Enabling low-power, multi-modal neural interfaces through a common, low-bandwidth feature space. IEEE Transactions on Neural Systems and Rehabilitation Engineering 2016; 24(5): 521-31.

Johansson JD, Blomstedt P, Haj-Hosseini N, Bergenheim AT, Eriksson O, Wardell K. Combined diffuse light reflectance and electrical impedance measurements as a navigation aid in deep brain surgery. Stereotact Funct Neurosurg 2009; 87(2): 105-13.

Jolliffe IT, Cadima J. Principal component analysis: a review and recent developments. Philosophical Transactions of the Royal Society A: Mathematical, Physical and Engineering Sciences 2016; 374(2065).

Jung YJ, Kim HJ, Jeon BS, Park H, Lee WW, Paek SH. An 8-Year Follow-up on the Effect of Subthalamic Nucleus Deep Brain Stimulation on Pain in Parkinson Disease. JAMA Neurol 2015; 72(5): 504-10.

Kellis S, Miller K, Thomson K, Brown R, House P, Greger B. Decoding spoken words using local field potentials recorded from the cortical surface. Journal of neural engineering 2010; 7(5): 056007.

Kent AR, Grill WM. Analysis of deep brain stimulation electrode characteristics for neural recording. J Neural Eng 2014; 11(4): 046010.

Khan MF, Mewes K, Gross RE, Skrinjar O. Assessment of brain shift related to deep brain stimulation surgery. Stereotact Funct Neurosurg 2008; 86(1): 44-53.

Kirin SC, Yanagisawa T, Oshino S, Edakawa K, Tanaka M, Kishima H, *et al.* Somatosensation Evoked by Cortical Surface Stimulation of the Human Primary Somatosensory Cortex. Front Neurosci 2019; 13: 1019.

Kirketeig T, Schultheis C, Zuidema X, Hunter CW, Deer T. Burst Spinal Cord Stimulation: A Clinical Review. Pain Med 2019; 20(Suppl 1): S31-S40.

Kirkland L, Kanfer F, Millard S. LASSO Tuning Parameter Selection; 2015.

Koeglsperger T, Palleis C, Hell F, Mehrkens JH, Botzel K. Deep Brain Stimulation Programming for Movement Disorders: Current Concepts and Evidence-Based Strategies. Front Neurol 2019; 10: 410.

Kramer MA, Tort AB, Kopell NJ. Sharp edge artifacts and spurious coupling in EEG frequency comodulation measures. Journal of neuroscience methods 2008; 170(2): 352-7.

Kubben PL, ter Meulen KJ, Schijns OEMG, ter Laak-Poort MP, van Overbeeke JJ, Santbrink Hv. Intraoperative MRI-guided resection of glioblastoma multiforme: a systematic review. The Lancet Oncology 2011; 12(11): 1062-70.

Kuhn AA, Volkmann J. Innovations in deep brain stimulation methodology. Mov Disord 2017; 32(1): 11-9.

Kumar K, Toth C, Nath RK. Deep brain stimulation for intractable pain: a 15-year experience. Neurosurgery 1997; 40(4): 736-46; discussion 46-7.

Kumaravelu K, Oza CS, Behrend CE, Grill WM. Model-based deconstruction of cortical evoked potentials generated by subthalamic nucleus deep brain stimulation. J Neurophysiol 2018; 120(2): 662-80.

Kuncel AM, Cooper SE, Grill WM. A method to estimate the spatial extent of activation in thalamic deep brain stimulation. Clin Neurophysiol 2008; 119(9): 2148-58.

Laitinen L, Johansson GG, Sipponen P. Impedance and phase angle as a locating method in human stereotaxic surgery. J Neurosurg 1966; 25(6): 628-33.

Lee B, Kramer D, Armenta Salas M, Kellis S, Brown D, Dobreva T, *et al.* Engineering Artificial Somatosensation Through Cortical Stimulation in Humans. Front Syst Neurosci 2018; 12: 24.

Lefranc M, Capel C, Pruvot AS, Fichten A, Desenclos C, Toussaint P, *et al.* The impact of the reference imaging modality, registration method and intraoperative flat-panel computed tomography on the accuracy of the ROSA(R) stereotactic robot. Stereotact Funct Neurosurg 2014; 92(4): 242-50.

Lempka SF, McIntyre CC. Theoretical analysis of the local field potential in deep brain stimulation applications. PLoS One 2013; 8(3): e59839.

Logothetis NK, Kayser C, Oeltermann A. In vivo measurement of cortical impedance spectrum in monkeys: implications for signal propagation. Neuron 2007; 55(5): 809-23.

Lopes-dos-Santos V, Panzeri S, Kayser C, Diamond ME, Quian Quiroga R. Extracting information in spike time patterns with wavelets and information theory. Journal of neurophysiology 2014; 113(3): 1015-33.

Lopes-dos-Santos V, Rey HG, Navajas J, Quiroga RQ. Extracting information from the shape and spatial distribution of evoked potentials. Journal of neuroscience methods 2017.

Lopez-Azcarate J, Tainta M, Rodriguez-Oroz MC, Valencia M, Gonzalez R, Guridi J, *et al.* Coupling between beta and high-frequency activity in the human subthalamic nucleus may be a pathophysiological mechanism in Parkinson's disease. J Neurosci 2010; 30(19): 6667-77.

Lucas JM, Ji Y, Masri R. Motor cortex stimulation reduces hyperalgesia in an animal model of central pain. Pain 2011; 152(6): 1398-407.

Lyketsos C, Holroyd K, Fosdick L, Smith G, Leoutsakos J-M, Munro C, *et al.* Deep brain stimulation targeting the fornix for mild Alzheimer dementia: design of the ADvance randomized controlled trial. Open Access Journal of Clinical Trials 2015.

Maks CB, Butson CR, Walter BL, Vitek JL, McIntyre CC. Deep brain stimulation activation volumes and their association with neurophysiological mapping and therapeutic outcomes. J Neurol Neurosurg Psychiatry 2009; 80(6): 659-66.

Maling N, Lempka SF, Blumenfeld Z, Bronte-Stewart H, McIntyre CC. Biophysical basis of subthalamic local field potentials recorded from deep brain stimulation electrodes. J Neurophysiol 2018; 120(4): 1932-44.

Mallat SG. A theory for multiresolution signal decomposition: the wavelet representation. IEEE transactions on pattern analysis and machine intelligence 1989; 11(7): 674-93.

Manning JR, Jacobs J, Fried I, Kahana MJ. Broadband shifts in local field potential power spectra are correlated with single-neuron spiking in humans. Journal of Neuroscience 2009; 29(43): 13613-20.

Marques A, Chassin O, Morand D, Pereira B, Debilly B, Derost P, *et al.* Central pain modulation after subthalamic nucleus stimulation: A crossover randomized trial. Neurology 2013; 81(7): 633-40.

Masri R, Quiton RL, Lucas JM, Murray PD, Thompson SM, Keller A. Zona incerta: a role in central pain. J Neurophysiol 2009; 102(1): 181-91.

Mayberg HS, Lozano AM, Voon V, McNeely HE, Seminowicz D, Hamani C, *et al.* Deep brain stimulation for treatment-resistant depression. Neuron 2005; 45(5): 651-60.

McClelland S, Ford B, Senatus PB, Winfield LM, Du YE, Pullman SL, *et al.* Subthalamic stimulation for Parkinson disease: determination of electrode location necessary for clinical efficacy. Neurosurgical Focus 2005; 19(5): 1-9.

McIntyre CC, Butson CR, Maks CB, Noecker AM. Optimizing deep brain stimulation parameter selection with detailed models of the electrode-tissue interface. Conf Proc IEEE Eng Med Biol Soc 2006; 1: 893-5.

McIntyre CC, Mori S, Sherman DL, Thakor NV, Vitek JL. Electric field and stimulating influence generated by deep brain stimulation of the subthalamic nucleus. Clin Neurophysiol 2004; 115(3): 589-95.

McNeal DR. Analysis of a model for excitation of myelinated nerve. IEEE Trans Biomed Eng 1976; 23(4): 329-37.

Merello M, Tenca E, Cerquetti D. Neuronal activity of the zona incerta in Parkinson's disease patients. Mov Disord 2006; 21(7): 937-43.

Miller K, Zanos S, Fetz E, Den Nijs M, Ojemann J. Decoupling the cortical power spectrum reveals real-time representation of individual finger movements in humans. Journal of Neuroscience 2009a; 29(10): 3132-7.

Miller KJ, Abel TJ, Hebb AO, Ojemann JG. Rapid online language mapping with electrocorticography. Journal of Neurosurgery Pediatrics 2011; 7(5): 482-90.

Miller KJ, Hermes D, Honey CJ, Sharma M, Rao RP, Den Nijs M, *et al.* Dynamic modulation of local population activity by rhythm phase in human occipital cortex during a visual search task. Frontiers in human neuroscience 2010; 4: 197.

Miller KJ, Hermes D, Schalk G, Ramsey NF, Jagadeesh B, Den Nijs M, *et al.* Detection of spontaneous class-specific visual stimuli with high temporal accuracy in human electrocorticography. Engineering in Medicine and Biology Society, 2009 EMBC 2009 Annual International Conference of the IEEE; 2009b: IEEE; 2009b. p. 6465-8.

Miller KJ, Sorensen LB, Ojemann JG, Den Nijs M. Power-law scaling in the brain surface electric potential. PLoS computational biology 2009c; 5(12): e1000609.

Mitrofanis J. Some certainty for the "zone of uncertainty"? Exploring the function of the zona incerta. Neuroscience 2005; 130(1): 1-15.

Moon HC, Park YS. Reduced GABAergic neuronal activity in zona incerta causes neuropathic pain in a rat sciatic nerve chronic constriction injury model. J Pain Res 2017; 10: 1125-34.

Moran A, Bergman H, Israel Z, Bar-Gad I. Subthalamic nucleus functional organization revealed by parkinsonian neuronal oscillations and synchrony. Brain 2008; 131(Pt 12): 3395-409.

Moshel S, Shamir RR, Raz A, de Noriega FR, Eitan R, Bergman H, *et al.* Subthalamic nucleus long-range synchronization-an independent hallmark of human Parkinson's disease. Front Syst Neurosci 2013; 7: 79.

National Institute on Deafness and Other Communication Disorders. Cochlear Implants. 2017 March 6, 2017 [cited 2020 June 23]; Available from:

Newman J. Resistance for Flow of Current to a Disk. Journal of The Electrochemical Society 1966; 113(5).

Nicholson P. Specific impedance of cerebral white matter. Experimental Neurology 1965; 13(4): 386-401.

Novak P, Przybyszewski AW, Barborica A, Ravin P, Margolin L, Pilitsis JG. Localization of the subthalamic nucleus in Parkinson disease using multiunit activity. J Neurol Sci 2011; 310(1-2): 44-9.

Okun MS, Tagliati M, Pourfar M, Fernandez HH, Rodriguez RL, Alterman RL, *et al.* Management of referred deep brain stimulation failures: a retrospective analysis from 2 movement disorders centers. Arch Neurol 2005; 62(8): 1250-5.

Oshima H, Katayama Y, Morishita T, Sumi K, Otaka T, Kobayashi K, *et al.* Subthalamic nucleus stimulation for attenuation of pain related to Parkinson disease. J Neurosurg 2012; 116(1): 99-106.

Oswal A, Brown P, Litvak V. Movement related dynamics of subthalmo-cortical alpha connectivity in Parkinson's disease. Neuroimage 2013a; 70: 132-42.

Oswal A, Brown P, Litvak V. Synchronized neural oscillations and the pathophysiology of Parkinson's disease. Curr Opin Neurol 2013b; 26(6): 662-70.

Ozkurt TE, Butz M, Homburger M, Elben S, Vesper J, Wojtecki L, *et al.* High frequency oscillations in the subthalamic nucleus: a neurophysiological marker of the motor state in Parkinson's disease. Exp Neurol 2011; 229(2): 324-31.

Patil PG, Conrad EC, Aldridge JW, Chenevert TL, Chou KL. The anatomical and electrophysiological subthalamic nucleus visualized by 3-T magnetic resonance imaging. Neurosurgery 2012; 71(6): 1089-95; discussion 95.

Pena E, Zhang S, Deyo S, Xiao Y, Johnson MD. Particle swarm optimization for programming deep brain stimulation arrays. J Neural Eng 2017; 14(1): 016014.

Percival DB, Walden AT. Spectral analysis for physical applications: Cambridge University Press; 1993.

Peterson EJ, Izad O, Tyler DJ. Predicting myelinated axon activation using spatial characteristics of the extracellular field. J Neural Eng 2011; 8(4): 046030.

Pittman-Polletta B, Hsieh W-H, Kaur S, Lo M-T, Hu K. Detecting phase-amplitude coupling with high frequency resolution using adaptive decompositions. Journal of neuroscience methods 2014; 226: 15-32.

Plaha P, Ben-Shlomo Y, Patel NK, Gill SS. Stimulation of the caudal zona incerta is superior to stimulation of the subthalamic nucleus in improving contralateral parkinsonism. Brain 2006; 129(Pt 7): 1732-47.

Pollo C, Kaelin-Lang A, Oertel MF, Stieglitz L, Taub E, Fuhr P, *et al.* Directional deep brain stimulation: an intraoperative double-blind pilot study. Brain 2014; 137(Pt 7): 2015-26.

Rajshekhar V. Continuous impedance monitoring during CT-guided stereotactic surgery: relative value in cystic and solid lesions. Br J Neurosurg 1992; 6(5): 439-44.

Rana AQ, Kabir A, Jesudasan M, Siddiqui I, Khondker S. Pain in Parkinson's disease: analysis and literature review. Clin Neurol Neurosurg 2013; 115(11): 2313-7.

Rattay F. Analysis of models for external stimulation of axons. IEEE Trans Biomed Eng 1986; 33(10): 974-7.

Research Center for Adaptive Data Analysis. Hilbert Huang Transform MATLAB program. 2015 [cited November 10, 2017]; Available from: http://rcada.ncu.edu.tw/research1.htm

Robinson BW. Localization of intracerebral electrodes. Experimental Neurology 1962; 6(3): 201-23.

Robinson BW, Bryan JS, Rosvold HE. Locating brain structures. Extensions to the impedance method. Arch Neurol 1965; 13(5): 477-86.

Robinson BW, Tompkins HE. Impedance Method for Localizing Brain Structures. An Extension of the Method. Arch Neurol 1964; 10: 563-74.

Russo M, Van Buyten JP. 10-kHz High-Frequency SCS Therapy: A Clinical Summary. Pain Med 2015; 16(5): 934-42.

Sadleir RJ, Argibay A. Modeling skull electrical properties. Ann Biomed Eng 2007; 35(10): 1699-712.

Schlag J, Balvin R. Background activity in the cerebral cortex and reticular formation in relation with the electroencephalogram. Experimental Neurology 1963; 8(3): 203-19.

Schrader B, Hamel W, Weinert D, Mehdorn HM. Documentation of electrode localization. Mov Disord 2002; 17 Suppl 3: S167-74.

Schroeder KE, Irwin ZT, Bullard AJ, Thompson DE, Bentley JN, Stacey WC, *et al.* Robust tactile sensory responses in finger area of primate motor cortex relevant to prosthetic control. J Neural Eng 2017; 14(4): 046016.

Sederberg AJ, Pala A, Zheng HJV, He BJ, Stanley GB. State-aware detection of sensory stimuli in the cortex of the awake mouse. PLoS Comput Biol 2019; 15(5): e1006716.

Shannon RV, Cruz RJ, Galvin JJ, 3rd. Effect of stimulation rate on cochlear implant users' phoneme, word and sentence recognition in quiet and in noise. Audiol Neurootol 2011; 16(2): 113-23.

Shreve LA, Velisar A, Malekmohammadi M, Koop MM, Trager M, Quinn EJ, *et al.* Subthalamic oscillations and phase amplitude coupling are greater in the more affected hemisphere in Parkinson's disease. Clin Neurophysiol 2017; 128(1): 128-37.

Stark E, Abeles M. Predicting movement from multiunit activity. J Neurosci 2007; 27(31): 8387-94.

Stein E, Bar-Gad I. beta oscillations in the cortico-basal ganglia loop during parkinsonism. Exp Neurol 2013; 245: 52-9.

Surucu O, Baumann-Vogel H, Uhl M, Imbach LL, Baumann CR. Subthalamic deep brain stimulation versus best medical therapy for L-dopa responsive pain in Parkinson's disease. Pain 2013; 154(8): 1477-9.

Swan BD, Gasperson LB, Krucoff MO, Grill WM, Turner DA. Sensory percepts induced by microwire array and DBS microstimulation in human sensory thalamus. Brain Stimul 2018; 11(2): 416-22.

Tan DW, Schiefer MA, Keith MW, Anderson JR, Tyler J, Tyler DJ. A neural interface provides long-term stable natural touch perception. Sci Transl Med 2014; 6(257): 257ra138.

Tass P, Smirnov D, Karavaev A, Barnikol U, Barnikol T, Adamchic I, *et al.* The causal relationship between subcortical local field potential oscillations and Parkinsonian resting tremor. J Neural Eng 2010; 7(1): 16009.

Telkes I, Jimenez-Shahed J, Viswanathan A, Abosch A, Ince NF. Prediction of STN-DBS Electrode Implantation Track in Parkinson's Disease by Using Local Field Potentials. Front Neurosci 2016; 10: 198.

Telkes I, Viswanathan A, Jimenez-Shahed J, Abosch A, Ozturk M, Gupte A, *et al.* Local field potentials of subthalamic nucleus contain electrophysiological footprints of motor subtypes of Parkinson's disease. Proc Natl Acad Sci U S A 2018; 115(36): E8567-E76.

Teplitzky BA, Zitella LM, Xiao Y, Johnson MD. Model-Based Comparison of Deep Brain Stimulation Array Functionality with Varying Number of Radial Electrodes and Machine Learning Feature Sets. Front Comput Neurosci 2016; 10: 58.

Thompson JA, Lanctin D, Ince NF, Abosch A. Clinical implications of local field potentials for understanding and treating movement disorders. Stereotact Funct Neurosurg 2014; 92(4): 251-63.

Tibshirani R. Regression Shrinkage and Selection via the Lasso. Journal of the Royal Statistical Society Series B (Methodological) 1996; 58(1): 267-88.
Tinkhauser G, Pogosyan A, Debove I, Nowacki A, Shah SA, Seidel K, *et al.* Directional local field potentials: A tool to optimize deep brain stimulation. Mov Disord 2018; 33(1): 159-64.
Tinkhauser G, Pogosyan A, Little S, Beudel M, Herz DM, Tan H, *et al.* The modulatory effect of adaptive deep brain stimulation on beta bursts in Parkinson's disease. Brain 2017; 140(4): 1053-67.
Tuch DS, Wedeen VJ, Dale AM, George JS, Belliveau JW. Conductivity tensor mapping of the human brain using diffusion tensor MRI. Proc Natl Acad Sci U S A 2001; 98(20): 11697-701.
van Wijk BC, Beudel M, Jha A, Oswal A, Foltynie T, Hariz MI, *et al.* Subthalamic nucleus phase-amplitude coupling correlates with motor impairment in Parkinson's disease. Clin Neurophysiol 2016; 127(4): 2010-9.
van Wijk BCM, Pogosyan A, Hariz MI, Akram H, Foltynie T, Limousin P, *et al.* Localization of beta and high-frequency oscillations within the subthalamic nucleus region. Neuroimage Clin 2017; 16: 175-83.
Verhagen R, Zwartjes DG, Heida T, Wiegers EC, Contarino MF, de Bie RM, *et al.* Advanced target identification in STN-DBS with beta power of combined local field potentials and spiking activity. J Neurosci Methods 2015; 253: 116-25.
Volkmann J, Moro E, Pahwa R. Basic algorithms for the programming of deep brain stimulation in Parkinson's disease. Mov Disord 2006; 21 Suppl 14: S284-9.
von Langsdorff D, Paquis P, Fontaine D. In vivo measurement of the frame-based application accuracy of the Neuromate neurosurgical robot. J Neurosurg 2015; 122(1): 191-4.
Weiss N, Ohara S, Johnson KO, Lenz FA. The human thalamic somatic sensory nucleus [ventral caudal (Vc)] shows neuronal mechanoreceptor-like responses to optimal stimuli for peripheral mechanoreceptors. J Neurophysiol 2009; 101(2): 1033-42.
Wendel K, Vaisanen J, Seemann G, Hyttinen J, Malmivuo J. The influence of age and skull conductivity on surface and subdermal bipolar EEG leads. Comput Intell Neurosci 2010; 2010: 397272.
Whitt JL, Masri R, Pulimood NS, Keller A. Pathological activity in mediodorsal thalamus of rats with spinal cord injury pain. J Neurosci 2013; 33(9): 3915-26.
Winkler D, Tittgemeyer M, Schwarz J, Preul C, Strecker K, Meixensberger J. The first evaluation of brain shift during functional neurosurgery by deformation field analysis. J Neurol Neurosurg Psychiatry 2005; 76(8): 1161-3.
Wodarg F, Herzog J, Reese R, Falk D, Pinsker MO, Steigerwald F, *et al.* Stimulation site within the MRI-defined STN predicts postoperative motor outcome. Mov Disord 2012; 27(7): 874-9.
Wright N, Borden P, Liew Y, Bolus M, Stoy W, Forest C, *et al.* Rapid sensory adaptation in the thalamocortical network of the mouse and the relative contribution of synaptic depression. 2019; Chicago, IL: Society for Neuroscience; 2019.
Xiao Y, Pena E, Johnson MD. Theoretical Optimization of Stimulation Strategies for a Directionally Segmented Deep Brain Stimulation Electrode Array. IEEE Trans Biomed Eng 2016; 63(2): 359-71.
Yeh J-R, Shieh J-S, Huang NE. Complementary ensemble empirical mode decomposition: A novel noise enhanced data analysis method. Advances in adaptive data analysis 2010; 2(02): 135-56.
Yesavage JA, Sheikh JI. 9/Geriatric Depression Scale (GDS). Clinical Gerontologist 1986; 5(1-2): 165-73.

Yoshida F, Martinez-Torres I, Pogosyan A, Holl E, Petersen E, Chen CC, *et al.* Value of subthalamic nucleus local field potentials recordings in predicting stimulation parameters for deep brain stimulation in Parkinson's disease. J Neurol Neurosurg Psychiatry 2010; 81(8): 885-9.

Yousif N, Bayford R, Liu X. The influence of reactivity of the electrode-brain interface on the crossing electric current in therapeutic deep brain stimulation. Neuroscience 2008; 156(3): 597-606.

Yu C, Cassar IR, Sambangi J, Grill WM. Frequency-Specific Optogenetic Deep Brain Stimulation of Subthalamic Nucleus Improves Parkinsonian Motor Behaviors. J Neurosci 2020; 40(22): 4323-34.

Zaidel A, Spivak A, Grieb B, Bergman H, Israel Z. Subthalamic span of beta oscillations predicts deep brain stimulation efficacy for patients with Parkinson's disease. Brain 2010; 133(Pt 7): 2007-21.

Zonenshayn M, Sterio D, Kelly PJ, Rezai AR, Beric A. Location of the active contact within the subthalamic nucleus (STN) in the treatment of idiopathic Parkinson's disease. Surg Neurol 2004; 62(3): 216-25; discussion 25-6.